INSTITUTO SUPERIOR DE ENGENHARIA DO PORTO
MESTRADO EM ENGENHARIA MECÂNICA




Structural Optimization Combined with Meshless Methods - 2D Applications

DIOGO COSTA GONÇALVES
julho de 2020

POLITÉCNICO
DO PORTO

STRUCTURAL OPTIMIZATION COMBINED WITH MESHLESS METHODS – 2D APPLICATIONS

Diogo Costa Gonçalves

2020

ISEP – School of Engineering

Department of Mechanical Engineering

POLITÉCNICO
DO PORTO

Instituto Superior de Engenharia do Porto

STRUCTURAL OPTIMIZATION COMBINED WITH MESHLESS METHODS – 2D APPLICATIONS

Diogo Costa Gonçalves

1150709

Dissertation presented to the School of Engineering of the Polytechnic of Porto (ISEP) to fulfill the requirements necessary to obtain a Master's degree in Mechanical Engineering, supervised by Professor Doutor Jorge Américo Oliveira Pinto Belinha.

2020

ISEP – School of Engineering

Department of Mechanical Engineering

POLITÉCNICO DO PORTO

JURY

President

Raul Duarte Salgueiral Gomes Campilho, Ph.D.

Professor Adjunto, Departamento de Engenharia Mecânica

Instituto Superior de Engenharia do Porto (ISEP), Instituto Politécnico do Porto (IPP)

Supervisor

Jorge Américo de Oliveira Pinto Belinha, Ph.D.

Professor Adjunto, Departamento de Engenharia Mecânica

Instituto Superior de Engenharia do Porto (ISEP), Instituto Politécnico do Porto (IPP)

Examiner

Renato Manuel Natal Jorge, Ph.D.

Professor Catedrático, Departamento de Engenharia Mecânica

Faculdade de Engenharia da Universidade do Porto (FEUP)

AGRADECIMENTOS

Terminada esta dissertação e respetivo percurso académico, expresso os meus profundos e sinceros agradecimentos a todos que, direta ou indiretamente, contribuíram não só para a realização deste trabalho, mas também para a finalização com sucesso desta etapa académica.

Ao Professor Jorge Américo Oliveira Pinto Belinha, obrigado ter aceitado ser orientador e me ter dado oportunidade de realizar este trabalho no ramo da mecânica computacional, tema pelo qual desenvolvi especial interesse. Agradeço a contínua orientação e disponibilidade ao longo deste percurso.

Obrigado à instituição e comunidade ISEP pelas condições oferecidas. Ao Departamento de Engenharia Mecânica e docentes, obrigado pela disponibilidade e pelos conhecimentos e competências transmitidas. Agradeço também a todos os colegas de curso pela entreajuda e companheirismo.

À minha família e amigos, obrigado pelo contínuo esforço, acompanhamento e incentivo que tornaram possível a concretização deste trabalho. Obrigado!

INSTITUTIONAL ACKNOWLEDGEMENTS

The author truly acknowledges the work conditions provided by the department of mechanical engineering (DEM) of School of Engineering of the Polytechnic of Porto (ISEP-IPP), and by the MIT-Portugal project “MITEXPL/ISF/0084/2017”, funded by Massachusetts Institute of Technology (USA) and “Ministério da Ciência, Tecnologia e Ensino Superior - Fundação para a Ciência e a Tecnologia” (Portugal) and project UIDB/50022/2020 and “205_596864527 - Assisting the prevention and control of COVID-19 with 3D printing solutions” through “Ministério da Ciência, Tecnologia e Ensino Superior - Fundação para a Ciência e a Tecnologia” (Portugal)

Additionally, the author gratefully acknowledge the funding of Project NORTE-01-0145-FEDER-000022 - SciTech - Science and Technology for Competitive and Sustainable Industries, cofinanced by Programa Operacional Regional do Norte (NORTE2020), through Fundo Europeu de Desenvolvimento Regional (FEDER).

Finally, the author acknowledges the synergetic collaboration with the collaborators of “Computational Mechanics Research Laboratory CMech-Lab” (ISEP/FEUP/INEGI), and its director, Prof.Dr. Jorge Belinha, and its senior advisors, Prof.Dr. Renato Natal Jorge and Prof.Dr. Lúcia Dinis.

KEYWORDS

Finite Element Method; Meshless Methods; Structural Optimization; Evolutionary Algorithm; “Hard-Kill” Method.

ABSTRACT

Continuously, the industry seeks to reduce costs associated with the design and construction of structural materials. Today, structural optimization (or topologic optimization) is a large research area inside computational mechanics capable to reduce the amount of material used in the structure and, at the same time, assure its structural resistance and high performance. Thus, the development of new structural optimization algorithms and techniques will allow to produce structural elements using less material, leading to an overall cost reduction (design, production and use costs). Thus, the main objective of this dissertation is to implement and demonstrate the effectiveness of structural optimization in designing cost and energy efficient components. Although the Finite Element Method (FEM) is the most used discretization technique within structural optimization, meshless methods have been extended to optimization algorithms in recent years. Meshless methods are advanced discretization techniques that allow to discretize the problem domain by only using an unstructured nodal distribution. In this work, the FEM and two Radial Point Interpolation (RPI) meshless methods are combined with an Evolutionary Structural Optimization (ESO) algorithm. The Radial Point Interpolation Method (RPIM) and the Natural Neighbour Radial Point Interpolation Method (NNRPIM) formulation are described with detail, as well as the fundamentals of mechanics of solids required to combine meshless methods with structural optimization algorithms. Also, a literature review on structural optimization algorithms and its coupling with meshless methods is given. Regarding the numerical simulation, the optimization algorithm is applied to benchmark problems, allowing to calibrate algorithm parameters, as well as evaluate mesh influence and computational time. Afterwards, the methodology is extended to several industrial applications. The implementation of the structural optimization algorithm allowed to design innovative structures with reduced volume. By implementing structural optimization and designing innovative structures based on algorithm solutions, this work demonstrates the diversity of applications and benefits of using structural optimization in the product design phase.

PALAVRAS CHAVE

Método de Elementos Finitos; Métodos sem Malha; Otimização Estrutural; Algoritmo Evolucionário; Método “Hard-Kill”.

RESUMO

Continuamente, o setor industrial procura reduzir custos associados ao projeto e construção de materiais estruturais. Hoje, a otimização estrutural (ou otimização topológica) é uma grande área de investigação dentro da mecânica computacional, mostrando-se capaz de reduzir a quantidade de material usado na estrutura e, ao mesmo tempo, garantir sua resistência estrutural e alto desempenho. Assim, o desenvolvimento de novos algoritmos e técnicas de otimização estrutural permitirá produzir elementos estruturais utilizando menos material, levando a uma redução geral de custos (custos de projeto, produção e uso). Assim, o principal objetivo desta dissertação é implementar e demonstrar a eficácia da otimização estrutural em desenvolver componentes eficientes em termos de custo e energia. Embora o Método dos Elementos Finitos (MEF) seja o método de discretização mais utilizado em otimização estrutural, métodos sem malha têm sido aplicados em algoritmos de otimizaçao recentemente. Métodos sem malha são técnicas avançadas de discretização que permitem discretizar o domínio do problema usando apenas uma distribuição nodal não estruturada. Neste trabalho, o MEF e dois métodos sem malha de interpolação pontal radial são combinados com um algoritmo de otimização estrutural evolucionário. A formulação do *Radial Point Interpolation Method* (RPIM) e do *Natural Neighbour Radial Point Interpolation Method* (NNRPIM) é descrita com detalhe, bem como os fundamentos da mecânica dos sólidos necessários para combinar métodos sem mallha com algoritmos de otimização estrutural. Adicionalmente, é efetuada uma revisão da literatura de otimização estrutural e a sua combinação com métodos sem malha. No trabalho prático, o algoritmo de otimização é aplicado a problemas de referência, o que permite calibrar os parâmetros do algoritmo, assim como investigar a influência da malha e o tempo computacional. Depois, a metodologia é estendida a várias aplicações industriais. A implementação do algoritmo de otimização estrutural permitiu desenhar estruturas inovadoras com volume reduzido. Implementando otimização industrial e desenhando estruturas inovadoras baseadas em soluções do algoritmo, este trabalho demonstra a diversidade de aplicações e os benefícios de utilizar otimização estrutural na fase de projeto do produto.

LIST OF SYMBOLS AND ABBREVIATIONS

List of abbreviations

BEM	Boundary Element Method
BESO	Bi-directional Evolutionary Structural Optimization
CS-RPIM	Cell-based Smoothed Radial Point Interpolation Method
DEM	Diffuse Element Method
DR	Decrease ratio
DSA	Design Sensitivity Analysis
EFGM	Element Free Galerkin Method
ESO	Evolutionary Structural Optimization
FEM	Finite Element Method
FEMAS	Finite Element and Meshless Analysis Software
FEMAP	Finite Element Modelling And Postprocessing
FVMLPG	Finite Volume Meshless Local Petrov-Galerkin
GA	Genetic Algorithms
IGA	Isogeometric Analysis
LC	Load case
LC-RPIM	Linear Conforming Radial Point Interpolation Method
MFS	Method of Finite Spheres
MLPG	Meshless Local Petrov-Galerkin
MLS	Moving Least Square
MPRT	Monorail Personal Rapid Transit
MQ-RBF	Multi-Quadrics Radial Basis Functions

NEM	Natural Element Method
NI-RPIM	Nodal Integration Radial Point Interpolation Method
NNPG	Natural Neighbour Petrov-Galerkin
NNRPIM	Natural Neighbour Radial Point Interpolation Method
NREM	Natural Radial Element Method
PBF	Polynomial Basis Function
PIM	Point Interpolation Method
RBF	Radial Basis Functions
RKPM	Reproducing Kernel Particle Method
RPI	Radial Point Interpolators
RPIM	Radial Point Interpolation Method
SED	Strain Energy Density
SIMP	Solid Isotropic Microstructures with Penalization
SPH	Smoothed Particle Hydrodynamics
VM	Von Mises

List of units

kg	Kilogram
m	Meter
N	Newton
Pa	Pascal

List of symbols

$\boldsymbol{a}(\boldsymbol{x}_I)$	RBF coefficients
$\boldsymbol{B}$	Deformability matrix
$\boldsymbol{b}$	Body force per unit volume vector
$\boldsymbol{b}(\boldsymbol{x}_I)$	PBF coefficients
$\boldsymbol{c}$	Material constitutive matrix
D	Size of the support-domain (length, area or volume)

d	Domain dimension (one, two or three)
d_{0i}	Distance between node 0 and natural neighbour node i
d_{0i}^{*}	Half of d_{0i}
d_a	Average nodal spacing of the nodes inside the support-domain of $\boldsymbol{x}_I$
d_{iI}	Distance between the field nodes and the interest point $\boldsymbol{x}_I$
d_r	Circular influence-domain radius
d_{ref}	Reference influence-domain dimension
d_x, d_y	Rectangular influence-domain dimensions
E	Young's elastic modulus
$\boldsymbol{f_b}$	Body force vector
$\boldsymbol{f_t}$	External force vector
g	Gravity acceleration
$\boldsymbol{H}$	Interpolation matrix
h	Beam height
h_{av}	Average nodal spacing in the surroundings of $\boldsymbol{x}_I$
I	Moment of inertia
K	Stiffness
$\boldsymbol{K}$	Global Stiffness matrix
k	Dimensionless influence-domain parameter
L	Beam length
$\boldsymbol{L}$	Differential operator matrix
M_I	Middle point
$\boldsymbol{M_T}$	Assembled moment matrix
m	Number of monomials in the polynomial basis
N	Normal reaction force
$\boldsymbol{N}$	Nodal set vector
n	Number of nodes inside the influence-domain
$\boldsymbol{n}$	Unit outward vector normal to the boundary of domain
n_I	Interest node

$\boldsymbol{P}$	Polynomial moment matrix
P_I	Vertex of the Voronoï cell
$\boldsymbol{p}(\boldsymbol{x}_I)$	PBF vector
$\boldsymbol{R}$	RBF moment matrix
$\mathbb{R}^2$	Two-dimensional real numbers set
$\mathbb{R}^d$	d-dimensional real numbers set
$\boldsymbol{r}(\boldsymbol{x}_I)$	RBF vector
$\bar{\boldsymbol{t}}$	Traction on the natural boundary
$u(\boldsymbol{x}_1)$	Nodal values
$u^h(\boldsymbol{x}_I)$	Interpolation function
$\boldsymbol{u}_s$	Nodal values vector
$\boldsymbol{V}$	Voronoï cells vector
V_f	Volume fraction
V_i	Voronoï cell
V_i^*	Trial cell
W	Weight
$\widehat{w_I}$	Weight of the integration point
$\widehat{w_I^*}$	Weight of the integration point at the curve/surface
$\boldsymbol{X}$	Nodal coordinates vector
$\boldsymbol{x}$	Cartesian coordinates of a point
$\boldsymbol{x}_I$	Interest point
γ, p	MQ-RBF parameters
$\boldsymbol{\varepsilon}$	Deformation vector
μ	Static coefficient of friction
μ_1, μ_2	Material constitutive matrix coefficients
$\boldsymbol{\sigma}$	Cauchy stress tensor
υ	Poisson's ratio
$\boldsymbol{\varphi}(\boldsymbol{x}_I)$	Interpolation vector
ψ	Virtual work

$\boldsymbol{\psi}(\boldsymbol{x}_I)$	Byproduct vector
Γ	Boundary domain
Γ_t	Natural boundary
Γ_u	Essential boundary
Ω	Solid domain
%	Percentage
$\|\cdot\|$	Euclidean norm
:	Such that
$\forall$	For all
∇	Gradient operator
$\in$	Belonging to
$\wedge$	And
$:=$	Equal by definition
$\subset$	Subset

GLOSSARY OF TERMS

Hard-kill	Term defining the optimization method in which inefficient elements are instantly deleted
Checkerboard pattern	Pattern arising in the optimized structure due to the alternating presence of solid and void elements

FIGURES INDEX

TABLES INDEX

INDEX

INTRODUCTION

1 INTRODUCTION

Advancements in computer technology allowed numerical methods to become a fundamental tool in the design and simulation of complex engineering problems. Although the Finite Element Method (FEM) is the most widely used discrete numerical technique to simulate a wide range of engineering problems, it has some limitations inherent to the method procedure. Meshless methods were developed focusing on overcoming the limitations of mesh-based methods. In the present work, meshless methods are implemented in the structural optimization of structures. The FEM, the Radial Point Interpolation Method (RPIM) and the Natural Neighbour RPIM (NNRPIM) are combined with an evolutionay optimization algorithm.

1.1 FINITE ELEMENT METHOD BACKGROUND

Conceptually, the finite element divides a complex problem into smaller and simpler known problems. In the FEM, the problem domain is discretized in a set of nodes, which are naturally connected by the so-called elements. Although the FEM was popularized around the mid-1950s, its history can be traced back more than a hundred years to the works of Rayleigh and Ritz [1], [2]. The Galerkin method [3] is also considered a primordial work in the FEM development. In 1941, Hrennikov [4] used a framework method to solve one-dimensional elasticity problems. The work by Hrennikov represents an important contribution to the future developments of the FEM. After Hrennikov's paper, several works on the FEM topics were published. In 1943, Courant published a classic paper on the FEM formulation [5]. In this work, Courant presented the formulation for a triangular finite element. Argyris and Kelsey [6] contributed with matrix methods for structural analysis using energy principles. At this point in time, the theory concepts for solving problems resorting to the FEM formulation were roughly developed. However, the computer technology did not allow for the testing and application of the proposed techniques. FEM programs started to be implemented only a few years later.

The work developed by Turner *et al.* at Boeing [7] was a significant contribution to the FEM development. In this paper, the authors formulated the FEM based on the principle of virtual work. Even though FEM procedures were already being developed, the specific term "finite element" was only introduced in 1960 in a paper by Clough [8]. From 1960 onwards, the FEM was rapidly spread to a wide range of applications. Beyond the structural mechanics, the FEM was extended to the analysis of large deformations [9], dynamic applications [10], heat conduction [11] and fluid flows [12]. In 1967, Zienkiewicz and Taylor published the first book where the FEM concept and procedure is detailed presented [13]. FEM packages started to develop in the 1970s. Nowadays, several software is available to perform numerical analysis using the FEM, such as Ansys, Abaqus, Cosmos, Solidworks and Femap. Several reference books regarding the FEM formulation and implementation can also be found in the literature [14]–[17].

1.2 MESHLESS METHOD

In the last thirty years, meshless methods emerged as a viable alternative to the existing finite element numerical methods as the FEM and the Boundary Element Method (BEM) [18]–[20]. Even though the FEM was successfully applied in several engineering fields, the nature of the method procedure limits its accuracy in some applications. In problems where large deformations are present the FEM accuracy is limited by the mesh distortion. Remeshing could be a solution to the high mesh distortions, nonetheless the computational time and cost would be significantly high. The FEM is also not well suited for fracture mechanics and impact problems since remeshing is necessary due to the moving boundaries. Meshless methods are not affected by the mesh distortion, neither they need remeshing during the analysis. Hence, meshless methods started being developed to overcome the drawbacks of the existing methods in the mentioned applications. Meshless methods have been used in several engineering applications and are considered the next generation in computational techniques. Figure 1 demonstrates the continuous evolution in the number of publications on meshless methods since its initial developments [21]. Since the beginning of the millennium, meshless methods are being studied and implemented in the structural optimization field, in which the drawbacks of the FEM are even more compelling.

The meshless method concept born from the idea of not using elements to impose the nodal connectivity. In meshless methods the domain is also discretized in a set of nodes. Yet, the nodal connectivity is established by the overlapping of the influence domains of each node. Generally, meshless methods are more flexible and equally accurate. However, the computational cost and analysis time are usually higher. Although the post processing phase in meshless methods is the same as the FEM, the pre-processing analysis is more demanding due to the complex shape functions and high order integration schemes. The interpolation functions in meshless methods are more accurate and smoother than those in the FEM. Also, meshless methods present higher rates of convergence than the FEM.

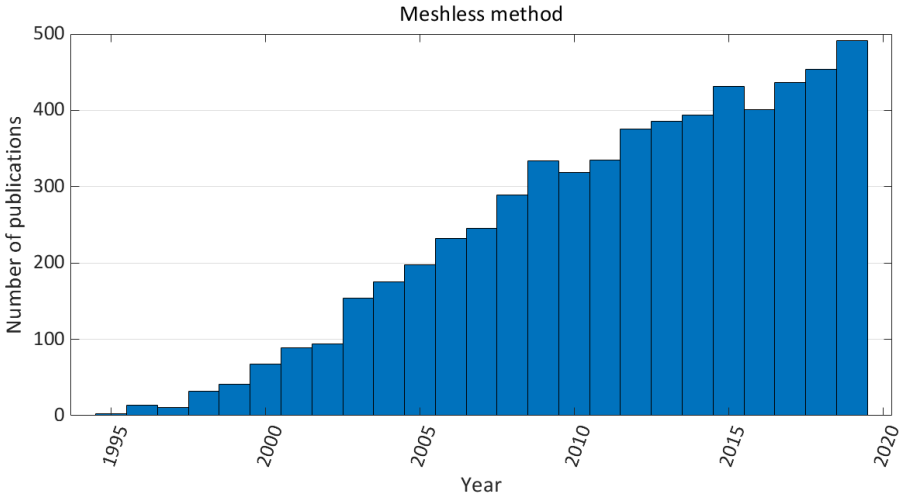

Figure 1 - Number of publications per year on meshless methods since 1995 [21]

1.3 STRUCTURAL OPTIMIZATION

One of the main objectives specifically pursued by the automotive and aerospace industries is the weight reduction of components while maintaining or even improving structure stiffness. Within the automotive and aerospace industries, a minimal weight reduction can not only represent a significant fuel save in the long-term, but also reduced carbon emissions and its impact on the environment. Thus, design optimization is of vital importance to produce cost and energy efficient designs with increased performance. Computational structural optimization techniques were developed and introduced into the engineering community with the objective of rapidly obtaining an optimal material configuration of a specific component. Optimization algorithms is a mathematical approach to computationally redistribute the material and determine the optimal design of a structure within certain objectives and constraints. The development of optimization techniques is constrained by the advancements in computer technology, yet an efficient design can nowadays be achieved by the means of structural optimization algorithms, which have been successfully applied in industrial applications.

Considering the structural optimization of isotropic components, three kinds of optimization problems can be defined: size, shape, and topology optimization. Size optimization deals with the size of a component within a known shape. An example of size optimization is the optimization of the cross-sectional dimensions of beams with known length and position. In shape optimization, the boundary of the structure is modified to achieve an optimal design. Topology is the most beneficial and general type of optimization. In topology optimization, algorithms determine the number, location, and shape of cavities within a continuum domain, thus resulting in an optimal material distribution. Although topology is the most beneficial kind of optimization, it generally leads to highly complex geometries which may turn to be impracticable to produce.

In the early developments of structural optimization, the solutions obtained by optimization algorithms were unfeasible. The benefits in producing efficiently designed components did not justify the cost in manufacturing such complex shapes by conventional manufacturing procedures. Recently, the additive manufacturing technology have been under huge development and it is nowadays a viable manufacturing process. The additive manufacturing process allows to promptly obtain highly complex structures. Thus, the additive manufacturing technology may be a complement to structural optimization methods and justify the practical implementation of the optimal solutions given by optimization algorithms.

1.4 DISSERTATION MOTIVATION AND OBJECTIVES

Both industry and academic communities permanently investigate innovative methodologies to design cost and energy efficient structural components. As previously referred, structural optimization is a growing topic in engineering and science. Regarding the structural analysis phase, the FEM is the most experienced numerical method in optimization algorithms. Differently, the implementation of meshless methods in structural optimization represents a research necessity and opportunity. The present

dissertation aims to combine an evolutionary algorithm with the FEM, RPIM and NNRPIM in the structural analysis, hence consolidating the FEM as a viable numerical tool and pushing the meshless method boundary in the structural optimization field. The objectives of the present work can be summarized as follows:

i. Calibrate parameters of the evolutionary algorithm by solving structural optimization benchmark examples;
ii. Study mesh influence on the optimized solutions;
iii. Evaluate computational time of the structural optimization analysis;
iv. Extend developed methodology to industrial applications;
v. Demonstrate effectiveness of structural optimization in designing cost and energy efficient structures with reduced weight.

1.5 DOCUMENT STRUCTURE

The present dissertation is divided in three main chapters: introduction (1), literature review (2), dissertation development (3) and conclusions (4). An introduction to the subject of the work is presented in first chapter. A brief history of the FEM as well as the motivation to the development of meshless methods is given. Then, the structural optimization subject is introduced, and the dissertation motivation and objectives are presented.

In the second chapter the research work developed is presented. In section 2.1, the radial point interpolators (RPI) meshless methods formulation is reviewed. Initially, the history and state of the art of meshless methods is presented, focusing on the RPIM and NNRPIM meshless methods. The concepts of natural neighbours, Voronoï diagram and Delaunay triangulation are presented. Then, the nodal connectivity, numerical integration, and shape functions construction procedures in the RPIM and NNRPIM are presented. Concluding, the approach to obtain the final discrete system of equations is given. Section 2.2 is dedicated to the structural optimization research. Firstly, the background of structural optimization and developed algorithms are presented. Then, a review on the implementation of numerical methods in the structural optimization field is presented, focusing on the implementation of meshless techniques in the design optimization. To conclude, relevant industrial applications of topology optimization are given to demonstrate the benefits of topology optimization and its practical applications.

The practical work developed is presented in the third chapter. Initially, a preliminary convergence study is carried out to validate the used numerical methods. Afterwards, the structural optimization algorithm is applied to benchmark optimization examples using the FEM, RPIM and NNRPIM. The structural optimization algorithm parameters are calibrated, and the mesh influence and computational time are investigated. Finally, the proposed methodology is applied to industrial components. A wheel rim, brake pedal and aircraft wing rib are analysed. Lastly, main conclusions work developed, as well as extensions to this dissertation and future works regarding structural optimization combined with meshless techniques are presented in the fourth chapter.

BIBLIOGRAPHIC WORK

2.1 RADIAL POINT INTERPOLATION MESHLESS METHODS

2.1.1 STATE OF THE ART

2.1.2 STANDART MESHLESS METHOD PROCEDURE

2.1.3 NATURAL NEIGHBOURS, VORONOÏ DIAGRAM AND DELAUNAY TRIANGULATION

2.1.4 NUMERICAL INTEGRATION

2.1.5 NODAL CONNECTIVITY

2.1.6 RADIAL POINT INTERPOLATION SHAPE FUNCTIONS

2.1.7 SOLID MECHANICS

2.2 STRUCTURAL OPTIMIZATION

2.2.1 STATE OF THE ART

2.2.2 THE “HARD-KILL” METHOD

2.2.3 NUMERICAL METHODS IN STRUCTURAL OPTIMIZATION

2.2.4 INNOVATIVE APPLICATIONS IN INDUSTRY

2 BIBLIOGRAPHIC WORK

2.1 RADIAL POINT INTERPOLATION MESHLESS METHODS

In the following section, a review on meshless methods is presented. Initially, the historical evolution of the meshless method is described with focus on the RPIM and NNRPIM. Subsequently, the concepts supporting the RPIM and NNRPIM formulation are given. The numerical integration, nodal connectivity and shape functions construction procedures are described. Finally, the approach to obtain the final discrete set of equations is presented.

2.1.1 STATE OF THE ART

Meshless methods [22]–[24] started to be fully develop in early 1990s, however the earliest development of meshless methods can be traced back to the 1930s when meshless collocation methods were introduced [25]–[27]. One of the first meshless methods to emerge was the Smoothed Particle Hydrodynamics (SPH) method [28]. Initially, the SPH was used for modelling astrophysical phenomena without boundaries, such as exploding stars. Although the history of SPH methods can be traced back to early 1970's [22], they were applied to solid mechanics only in the 1990s [29]. SPH is based on kernel approximation and later it was the basis of the Reproducing Kernel Particle Method (RKPM) [30]. While the SPH method pursues the strong form formulation, in the 1990s methods based on weak form started to be develop since these are more stable and accurate. While strong form methods address the partial differential equations directly to obtain the exact solution, weak form methods use variational principles to obtain an approximate solution to the differential equations.

The first meshless methods employed approximating functions. Relevant approximation schemes are the Taylor approximation, the Moving Least Square (MLS) approximation, the Reproducing Kernel approximation and the hp-cloud approximation. The Diffuse Element Method (DEM) [31] was the first meshless method to use the Moving Least Squares (MLS) approximation [32] and to build the shape functions over scattered nodes. In 1994, Belytschko proposed the Element Free Galerkin Method (EFGM) [33], which is considered today as an improvement of the DEM. One year later, Liu *et al.* published the RKPM based on the reproducing kernel approximation. In 1998, the Meshless Local Petrov-Galerkin (MLPG) based on the local weak form formulation method was proposed [34]. Two years later, the Method of Finite Spheres (MFS) [35] was developed as a special case of the general formulation of the MLPG procedure.

Approximant methods were successfully developed and applied to many engineering fields. Yet, they present a major disadvantage which led to further development and creation of new procedures. Approximation functions do not satisfy the delta Kronecker property $\varphi_i(\boldsymbol{x}_j) \neq \delta_{ij}$, therefore essential boundary conditions cannot be enforced as easily as in FEM. Although approximant methods produce smoother solutions, meshless methods using interpolations functions started to develop since these satisfy the delta property. The Natural Element Method (NEM) [36], [37] was one of the first interpolation methods to develop. The NEM uses the Sibson interpolation functions and

the Voronoï diagram to impose the nodal connectivity. In 2001, The Point Interpolation Method (PIM) [38] was presented. Adding radial basis functions to the PIM interpolating functions led to the development of the RPIM [39]. The combination of the NEM with the RPIM originated the NNRPIM, a truly meshless method developed by Belinha and co-workers [40]. Contrarily to the RPIM, which uses a nodal independent background integration mesh, the NNRPIM is considered a truly meshless method since the integration mesh used is uniquely dependent on the nodal discretization. More recently, the Natural Radial Element Method (NREM) [41]–[43] was developed and demonstrated to be an accurate truly meshless method.

2.1.1.1 RADIAL POINT INTERPOLATION METHOD

The RPIM was originally proposed in 2002 [39] as an enhancement of the PIM [38], [44]. In the original PIM, the shape functions are constructed using polynomial interpolation through a set of nodes in a local support domain. The shape functions in the PIM possess the Kronecker delta function property, which allows a simpler enforcement of essential boundary conditions. Yet, the PIM presents some drawbacks. For instances, the perfect alignment of the nodes produces singular solutions in the interpolation function construction process [45]. The improvement of the PIM originated the RPIM. The RPIM results from the application of Radial Basis Functions (RBF) to the interpolation functions in the PIM. Using RBF as the PIM shape functions stabilizes the procedure and produces smoother solutions. The Gaussian and the multiquadric are the most common RBF, yet several RBF can be used. The RPIM uses the concept of influence domain to establish the nodal connectivity and a nodal independent background integration mesh is constructed for the numerical integration. The use of a nodal independent integration mesh shatters the literal concept of meshless method, thus the RPIM is not considered a truly meshless method. Succeeding the original method, several variants of the RPIM were developed. Such variants include the Linear Conforming RPIM (LC-RPIM) [46], the Nodal Integration RPIM (NI-RPIM) [47], the Cell-based Smoothed RPIM (CS-RPIM) [48], [49] and the NNRPIM [40].

2.1.1.2 NATURAL NEIGHBOUR RADIAL POINT INTERPOLATION METHOD

The NNRPIM [40] results from the combination of the RPIM with the Natural Neighbours concept, also present in the NEM. In the NNRPIM, the nodal connectivity is established by the overlap of “influence cells” rather than the “influence domain” approach in the RPIM. To determine the influence cells, the NNRPIM constructs the Voronoï diagram [50] and the Delaunay Tessellation [51]. The Delaunay tessellation creates a nodal dependent background mesh used in the numerical integration of the NNRPIM interpolation functions. Even though the NNRPIM is a relative recent meshless method [40], it has been extended to numerous computational mechanics fields and engineering applications. The NNRPIM presented successful results in the fields of static analysis of isotropic and orthotropic plates [52], functionally graded material plate analysis [53] and 3D shell-like approach [54] for laminated plates and shells [55]. Studies were also developed in dynamic analysis [56]–[59], fracture mechanics [60]–[63] and in more demanding applications as the large deformation analysis [64].

2.1.2 STANDART MESHLESS METHOD PROCEDURE

As other nodal dependent discretization methods, meshless methods respect a generic procedure. Initially, the geometry of the problem domain is established, and the essential and natural boundary conditions are identified. Afterwards, the problem domain is discretized in a regular or irregular nodal set. As in mesh-based methods, the nodal density affects the method performance. A fine nodal distribution results in more accurate solutions, however the computational time and cost grow with the number of nodes. To obtain more accurate results, locations with predictable stress concentrations should present higher nodal density when compared with locations in which the stress distribution is predictable.

Subsequently, a nodal dependent (NNRPIM) or independent (RPIM) background integration mesh is constructed to numerically integrate the integro-differential equations governing the studied phenomenon. Gaussian integration schemes resorting to nodal independent background integration lattices are common. Nonetheless, a nodal dependent integration scheme is also viable. In the NNRPIM, a nodal integration uniquely dependent on the nodal discretization is used. Since it is a fundamental concept to approach the NNRPIM formulation on numerical integration (section 2.1.4.2) and nodal connectivity (section 2.1.5.2), the construction of the Voronoï diagram resorting to the natural neighbours geometric concept and the Delaunay triangulation are described in the next section.

After constructing a background integration mesh, the next step in the general meshless method procedure is to establish the nodal connectivity. In the FEM, the nodal connectivity is naturally assured by the finite element mesh. However, in meshless methods there are no elements and the nodal connectivity must be imposed. Meshless methods use the concept of influence domains (RPIM) or influence cells (NNRPIM). The nodal connectivity is then established by the overlap of the influence domains or cells. Subsequently, the field variables are obtained using interpolation or approximation functions. The final phase is to establish the equation system based on the strong or weak form formulation. The resulting equations are then assembled in a global equation system matrix. Finally, the set of equations is solved using a suitable technique [45].

2.1.3 NATURAL NEIGHBOURS, VORONOÏ DIAGRAM AND DELAUNAY TRIANGULATION

The present section is dedicated to the geometrical concepts behind the NNRPIM formulation: the Voronoï diagram and the Delaunay Tessellation. The Voronoï diagram is constructed using the natural neighbours geometrical concept, originally introduced by Sibson for data fitting and field smoothing [65]. Properties and applications of the Voronoï diagram can be found in the literature [66], [67] along with efficient algorithms to construct Voronoï tessellations [45], [68].

2.1.3.1 VORONOÏ DIAGRAM CONSTRUCTION

Consider the nodal set $\boldsymbol{N} = \{n_1, n_2, \dots, n_N\} \in \mathbb{R}^2$ discretizing the space $\Omega \subset \mathbb{R}^d$ with $\boldsymbol{X} = \{\boldsymbol{x}_1, \boldsymbol{x}_2, \dots, \boldsymbol{x}_N\} \in \Omega$. The Voronoï diagram is composed by the N closed and convex sub-regions V_i defining the set of Voronoï cells $\boldsymbol{V} = \{V_1, V_2, \dots, V_N\}$. Each cell V_i is associated with the node n_i so that any point inside V_i is closer to n_i than any other node $n_j \in \boldsymbol{N} \wedge j \neq i$. Thus, the Voronoï V_i is defined [45] by:

$$V_i \coloneqq \left\{\boldsymbol{x} \in \Omega \subset \mathbb{R}^d : \|\boldsymbol{x}_I - \boldsymbol{x}_i\| < \left\|\boldsymbol{x}_I - \boldsymbol{x}_j\right\|, \forall i \neq j\right\} \tag{1}$$

Being $\boldsymbol{x}_I$ an interest point of the domain and $\|\cdot\|$ the Euclidian metric norm or the distance between two points.

The procedure of the construction of the Voronoï diagram is presented next. For simplicity, it is considered a two-dimensional space, however the presented procedure can be easily extrapolated to the three-dimensional scenario. Consider a two-dimensional space $\Omega \subset \mathbb{R}^2$ and the nodal set present in Figure 2a. The objective is to determine the Voronoï cell of the node n_0. Initially a group of nodes is preselected as potential natural neighbours of the node n_0. Then a single node is picked, for example node n_7 and the vector $\boldsymbol{u}_{70}$ is defined:

$$\boldsymbol{u}_{70} = \frac{(\boldsymbol{x}_0 - \boldsymbol{x}_7)}{\|\boldsymbol{x}_0 - \boldsymbol{x}_7\|} \tag{2}$$

Considering vector $\boldsymbol{u}_{70}$ as the normal vector, the plane π_{70} is defined as:

$$u_{70}x + v_{70}y + w_{70}z = u_{70}x_7 + v_{70}y_7 + w_{70}z_7 \tag{3}$$

After the definition of plane π_{70}, all nodes to be considered as natural neighbours of node π_{70} must satisfy the following condition:

$$u_{70}x + v_{70}y + w_{70}z \geq u_{70}x_7 + v_{70}y_7 + w_{70}z_7 \tag{4}$$

The nodes that do not satisfy this condition are eliminated from the set of natural neighbour nodes of node n_0. This process is demonstrated in Figure 2b where one can notice that nodes n_6 and n_8 do not satisfy the previous condition and must not be considered as natural neighbours of node n_0. Subsequently, the process is repeated for all preselected nodes. In the end a group of nodes is defined as being the natural neighbours of node n_0. All nodes defined as the natural neighbours of node n_0 (Figure 2c) respect simultaneously the following set of conditions:

$$\begin{cases} u_{10}x + v_{10}y + w_{10}z \geq u_{10}x_1 + v_{10}y_1 + w_{10}z_1 \\ u_{30}x + v_{30}y + w_{30}z \geq u_{30}x_3 + v_{30}y_3 + w_{30}z_3 \\ u_{40}x + v_{40}y + w_{40}z \geq u_{40}x_4 + v_{40}y_4 + w_{40}z_4 \\ u_{50}x + v_{50}y + w_{50}z \geq u_{50}x_5 + v_{50}y_5 + w_{50}z_5 \\ u_{70}x + v_{70}y + w_{70}z \geq u_{70}x_7 + v_{70}y_7 + w_{70}z_7 \\ u_{90}x + v_{90}y + w_{90}z \geq u_{90}x_9 + v_{90}y_9 + w_{90}z_9 \end{cases} \tag{5}$$

The geometrical space in which all points satisfy the previous set of conditions forms an auxiliary trial cell $V_0{}^*$. The final step is the actual definition of the Voronoï cell V_0, which is the homothetic form of $V_0{}^*$. Figure 2d demonstrates this final procedure, where $d_{0i}{}^*$ is defined as:

$$d_{0i}{}^* = \frac{d_{0i}}{2} = \frac{\|\boldsymbol{x}_0 - \boldsymbol{x}_i\|}{2} \tag{6}$$

In order to obtain the Voronoï diagram, the described procedure is applied to all nodes discretizing the domain.

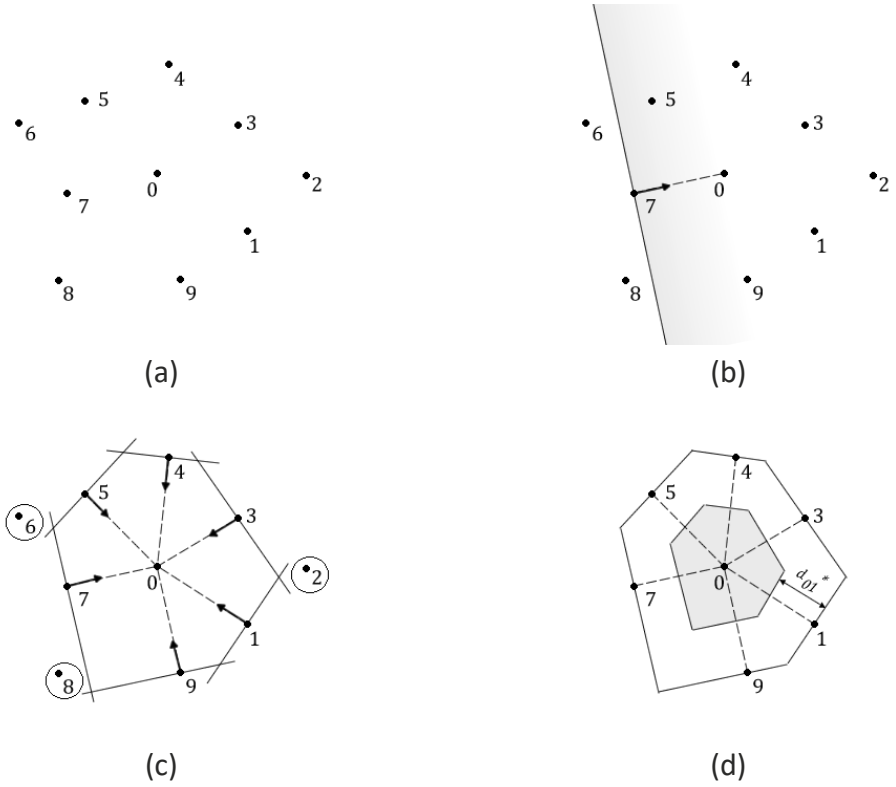

Figure 2 - Construction phases of a Voronoï cell (adapted from [45]): (a) Nodal set and potential natural neighbours of node n_0; (b) First trial plane; (c) Trial cell of node n_0; (d) Voronoï cell of node n_0

2.1.3.2 DELAUNAY TRIANGULATION

The numerical integration in the NNRPIM resorts to the Delaunay triangulation, which is considered as the geometrical dual of the Voronoï diagram (Figure 3a). The Delaunay triangles are constructed by connecting the nodes which have a Voronoï edge in common as Figure 3b demonstrates. The Delaunay triangulation forms a mesh totally dependent on the nodal spatial discretization that is used to integrate the NNRPIM shape functions. The Delaunay triangulation possess unique properties, such as the ‘‘empty circumcircle criterion” [69]. This criterion implies that a circumcircle formed by a Delaunay triangle contains no other nodes than the ones forming the respective triangle. The circumcircles formed by Delaunay triangles are known as “natural neighbour circumcircles” [70], whose centres are the vertex of the respective Voronoï cell. The concept of natural neighbour circumcircles is illustrated in Figure 3b.

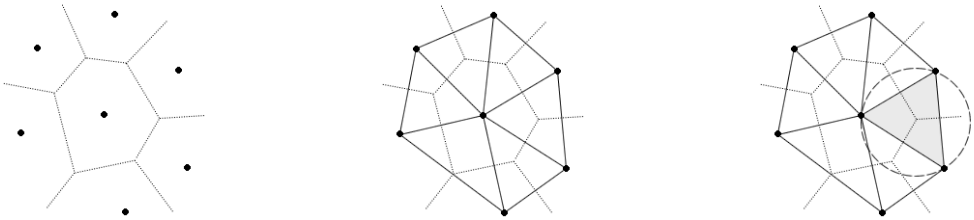

(a) (b) (c)

Figure 3 - (a) Voronoï diagram; (b) Delaunay *triangulation*; (c) Natural neighbour *circumcircles*

2.1.4 NUMERICAL INTEGRATION

Numerical integration is a fundamental module in the meshless method procedure. Since the early development of meshless methods, the scientific community recognized that the numerical integration in meshless methods represents a higher challenge than the FEM numerical integration [71]. The numerical integration in meshless methods is addressed by several authors in the literature [45], [72]–[76]. The integration represents a significant part in the total computational cost of the analysis [45], thus this step must be carefully parametrized. The density of the discretization and the density of the background mesh must be related to obtain more accurate results. Several authors have proposed empiric expressions to determine the optimal relation between the total number of field nodes and the total number of integration nodes used to discretize the problem domain [33], [45], [75], [77], [78].

2.1.4.1 GAUSSIAN QUADRATURE INTEGRATION (RPIM)

The Gauss-Legendre quadrature integration scheme is used in the RPIM. To implement the Gauss-Legendre integration scheme, a nodal independent background integration mesh is constructed. As in FEM, it is common to use Gaussian integration meshes fitted to the domain (Figure 4a), yet using background meshes larger than the problem domain is also viable (Figure 4b). Studies on numerical integration demonstrate that the integration mesh can have the size of the problem domain or a larger one without affecting significantly the final results [33]. However, using meshes fitted to the domain are more computational demanding. Thus, blind integration meshes are the most used due to its simplicity and ease of implementation.

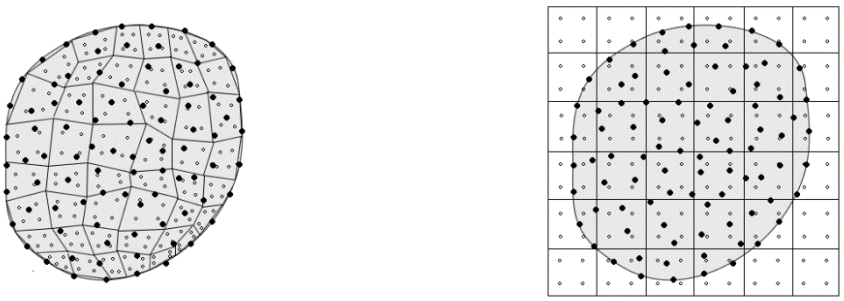

(a) (b)

Figure 4 - (a) Fitted Gaussian integration mesh; (b) Background Gaussian integration mesh

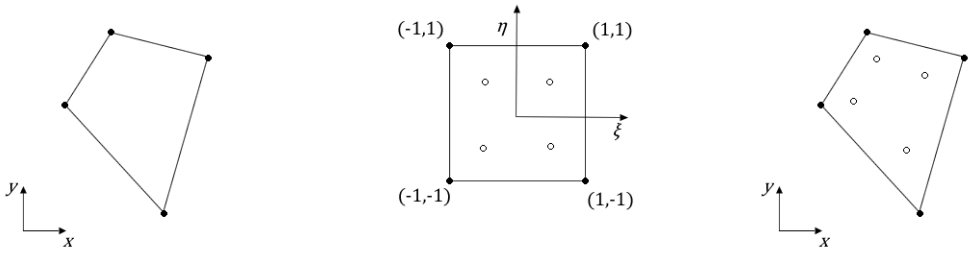

Figure 5 - Gaussian quadrature integration scheme: (a) Initial quadrilateral; (b) Transformation into an isoparametric square and 2 x 2 quadrature point rule; (c) Return to the initial quadrilateral

If a fitted mesh is constructed, the original grid-cells (Figure 5a) must be converted into an isoparametric square (Figure 5b). Then, Gauss points are distributed over the isoparametric square. Several Gauss points can be used, however the most common scheme is the two-point Gauss quadrature integration. The integration points location and weights can be found in the literature. Afterwards, the isoparametric square is converted back to the original shape in the Cartesian coordinate system (Figure 5c). When using blind integration meshes, there is no need to transform the original quadrilaterals. Yet, some integration points may be positioned outside the problem domain and must be removed from the integration procedure. Subsequently, in order to obtain the numerical integration of a function $\boldsymbol{F}(\boldsymbol{x})$, the continuums integral can be substituted by a sum:

$$\int_{\Omega} \boldsymbol{F}(\boldsymbol{x}) d\Omega = \sum_{i=1}^{n_g} \widehat{w_i} \boldsymbol{F}(\boldsymbol{x}_i) \tag{7}$$

Being $\widehat{w_i}$ the weight and $\boldsymbol{x}_i$ the location of each Gauss integration point (both in the Cartesian coordinate system).

2.1.4.2 NODAL BASED INTEGRATION (NNRPIM)

The NNRPIM uses an innovative nodal based integration scheme [40]. Within this technique, the construction of the integration mesh relies uniquely on the nodal spatial distribution. The Voronoï diagram [50] and the Delaunay triangulation [51] presented in section 2.1.3 are used to construct a nodal dependent background integration mesh. The presented nodal based integration scheme was successfully applied to one-, two- and three-dimensional domains using the NNRPIM formulation [40], [52]. Recently, this technique was used with the NREM [41]–[43].

Consider a two-dimensional domain and a node n_I. By using the Delaunay triangulation described in 2.1.3, the respective Voronoï cell is divided in n sub cells as Figure 6a illustrates, being n the number of natural neighbours of node n_I. The created sub cells are quadrilaterals defined by the node n_I, the vertex of the Voronoï cell P_I and the middle points M_I (Figure 6b). If a regular nodal discretization is employed the Voronoï diagram is composed by perfect squared cells. Thus, following the same procedure in regular nodal discretizations leads to triangular sub cells as Figure 7 demonstrates.

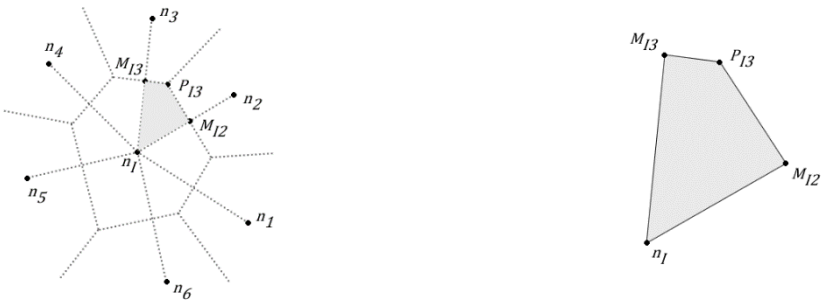

(a) (b)

Figure 6 - (a) Irregular nodal discretization and generated quadrilaterals; (b) Generated quadrilateral

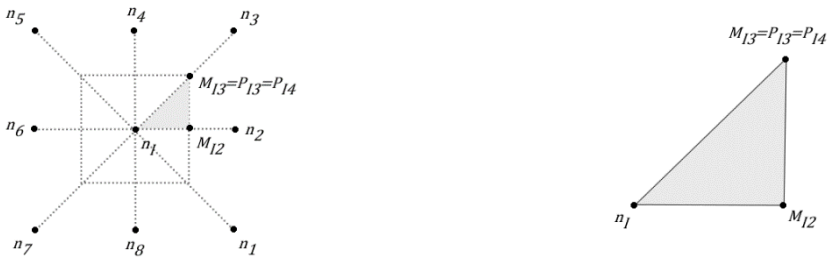

(a) (b)

Figure 7 - (a) Regular nodal discretization and generated triangles; b) Generated triangle

After dividing each Voronoï cell in n sub cells, Gauss integration points can be distributed inside the generated quadrilaterals or triangles following the procedure described in the previous section. Using a single Gauss point per sub cell is the simpler approach (integration of order 0). The location of the single integration point is the barycentre of the sub cell and its weight is the area of the respective sub cell.

It is possible to achieve a more general approach by dividing again each sub cell (triangular or quadrilateral) in smaller quadrilaterals. The new quadrilaterals are constructed by connecting the barycentre of the triangle (Figure 8a) or quadrilateral (Figure 8b) shapes to the middle points of the original edges. Then, the Gauss-Legendre Integration scheme can be applied using a single (integration of order 1) or several integration $k \times k$ points (integration of order k). This technique is generally used to integrate high order differential equations such as the ones arising in fluid dynamics analysis.

(a) (b)

Figure 8 - (a) Subdivision of a triangular sub cell in quadrilaterals; (b) Subdivision of a quadrilateral sub cell in smaller quadrilaterals

The pure nodal integration scheme considers a single integration point coincident with the barycentre of each Voronoï cell. The weight of the integration point is the area of the respective Voronoï cell, which is obtained by summing the areas of all sub cells. The drawback of this integration scheme is that the nodal integration is not enough to integrate accurately the meshless methods interpolation functions. Thus, stabilization techniques [45], [72], [74], [76], [79]–[81] are needed to obtain accurate results, which significantly increases the computational time of the analysis. All the described procedures can be extrapolated to the three-dimensional analysis. Yet, the computational time and cost of the more complex integration schemes is high. Studies on the NNRPIM [40] showed that a single Gauss point per sub cell is enough to obtain accurate results.

2.1.5 NODAL CONNECTIVITY

Contrarily to the FEM, in meshless methods the nodal connectivity must be established after discretizing the domain with a set of nodes. Meshless methods use the concept of influence domains to enforce the nodal connectivity, which is established by the overlap of the influence domains. In the following section, the influence domain approach used by the RPIM is described. Subsequently, a recently developed "influence-cell" approach to establish the nodal connectivity is presented [45].

2.1.5.1 INFLUENCE-DOMAINS (RPIM)

Many meshless methods use the influence domains concept [30], [33], [34], [39]. In the RPIM the nodal connectivity is established by the overlap of the influence domains of each node. The influence domains are defined by searching nodes inside a fixed area or volume, for two- and three-dimensional problems respectively. The size and shape of the influence domains affect the method's performance. All influence domains should contain the same number of nodes to obtain more accurate solutions. Previous works suggest that the ideal number of nodes inside the influence domains is between nine and sixteen nodes [33], [34], [38], [39], [45]. In these works, a reference dimension d_{ref} for the influence domains is established:

$$d_{ref} = k \cdot h_{av} \tag{8}$$

Where h_{av} is the average nodal spacing in the surroundings of $\boldsymbol{x}_I$ and k a dimensionless parameter ranging between $k = [1{,}5;\ 2{,}5]$.

Initially the dimensions of the influence domains are established. Considering a two-dimensional space and fixed size influence-domains, two shapes are suggested: rectangular and circular shapes. In the case of the rectangular shape d_x and d_y are determined, and for the circular shape d_R is determined. Then, for each interest point $\boldsymbol{x}_I$, the n nodes inside the influence domain centred in $\boldsymbol{x}_I$ are identified. Within fixed size influence domains, interest points near the domain boundary may have less nodes inside the respective fixed size influence domain in comparison with an inner interest point as Figure 9a demonstrates. This inconsistency can lead to the loss of accuracy in

the analysis. Yet, because of its simplicity and ease of implementation, fixed size influence-domains is the most used technique to enforce the nodal connectivity.

Although fixed size influence domains are simpler and easy to implement, variable size influence domains allow a constant connectivity along the domain. They also allow the construction of shape functions with the same degree of complexity in the whole domain. In variable size influence domains, the number of nodes inside the influence domains n is established. Then, a radial search centred in an interest point $\boldsymbol{x}_I$ is executed. The n closest nodes are identified, thus defining the influence domain. Figure 9b illustrates the concept of variable influence domains. Although interest point $\boldsymbol{x}_i$ is near the boundary and interest point $\boldsymbol{x}_j$ is deep inside the domain, both have the same number of nodes inside. The flexible influence-domains approach generally leads to more accurate results, however the computational time is higher.

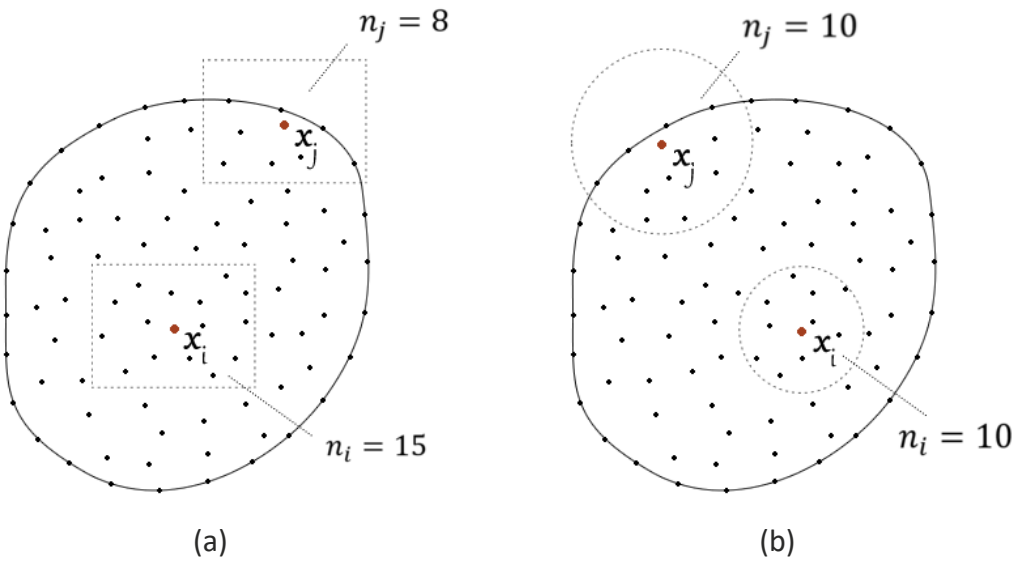

Figure 9 - (a) Fixed rectangular influence-domain; (b) Flexible circular influence-domain

2.1.5.2 INFLUENCE-CELLS (NNRPIM)

The NNRPIM uses a recently developed technique to enforce the nodal connectivity [40]. Instead of using blind influence domains, this technique determines the nodal connectivity directly from the nodal discretization. The Voronoï diagrams and the Delaunay triangulation mathematical concepts described in section 2.1.3 are used to impose the nodal connectivity. Since the influence domains are determined resorting to the Voronoï diagram, within this technique the influence domains are defined as influence cells. The influence-cell approach is analogous to the influence domain methodology considering that the nodal connectivity is imposed by the overlap of the influence cells. However, the set of nodes belonging to the influence cell and contributing to the interpolation of an interest point are determined using the Voronoï diagram instead of a radial search.

Two classes of influence-cells may be considered: first degree influence-cell (Figure 10a) and second degree influence cell (Figure 10b). The first-degree influence cell is composed by the cells of each natural neighbour of the interest point. In order to obtain

the second-degree influence-cell of an interest point, the first-degree influence-cell must be determined. Then, the same procedure is repeated for each node composing the first-degree influence-cell. Thus, the second degree is composed by the nodes belonging to the first-degree influence-cell plus the natural neighbours of each node of the first-degree influence-cell. Using second-degree influence cells generally leads to more accurate results, since these are naturally larger and allow a deeper connectivity. Yet, the computational time and cost is generally higher.

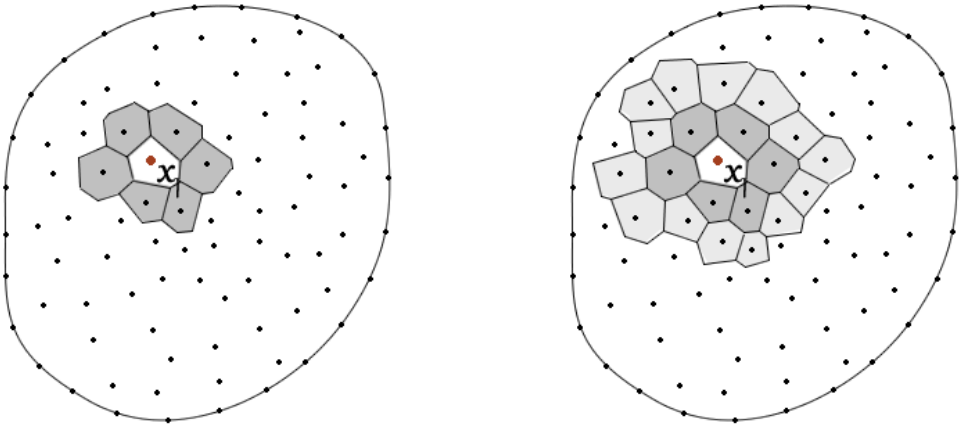

(a) (b)

Figure 10 - Influence cells: (a) First degree influence-cell; (b) Second degree influence-cell

2.1.6 RADIAL POINT INTERPOLATION SHAPE FUNCTIONS

Both RPIM and NNRPIM use the RPI to construct the shape functions. In the current section, the procedure to construct the RPI shape functions is described. A $\mathbb{R}^d$ dimensional space is discretized in a set of N nodes with coordinates $\boldsymbol{X} = \{\boldsymbol{x}_1, \boldsymbol{x}_2, \dots, \boldsymbol{x}_n\} \in \boldsymbol{\Omega} \wedge \boldsymbol{x}_i \in \mathbb{R}^d$. Considering a continuous scalar function $u(\boldsymbol{x})$, the interpolation function $u^h(\boldsymbol{x}_I)$ combines a RBF and a polynomial basis function (PBF). Thus, for an interest point $\boldsymbol{x}_I \in \mathbb{R}^d$, the interpolation function can be defined as:

$$\begin{aligned} u^h(\boldsymbol{x}_I) &= \sum_{i=i}^{n} r_i(\boldsymbol{x}_i - \boldsymbol{x}_I) a_i(\boldsymbol{x}_I) + \sum_{j=i}^{m} p_j(\boldsymbol{x}_I) b_j(\boldsymbol{x}_I) \\ &= \{\boldsymbol{r}(\boldsymbol{x}_I)^T \quad \boldsymbol{p}(\boldsymbol{x}_I)^T\} \begin{Bmatrix} \boldsymbol{a}(\boldsymbol{x}_I) \\ \boldsymbol{b}(\boldsymbol{x}_I) \end{Bmatrix} \end{aligned} \tag{9}$$

Being n the number of nodes inside the support domain of the interest point $\boldsymbol{x}_I$ and m the number of monomials of the complete polynomial basis. $\boldsymbol{a}(\boldsymbol{x}_I)$ and $\boldsymbol{b}(\boldsymbol{x}_I)$ are the non-constant coefficients of $\boldsymbol{r}(\boldsymbol{x}_I)$ and $\boldsymbol{p}(\boldsymbol{x}_I)$:

$$\boldsymbol{a}(\boldsymbol{x}_I) = \{a_1(\boldsymbol{x}_I) \quad a_2(\boldsymbol{x}_I) \quad \cdots \quad a_n(\boldsymbol{x}_I)\}^T \tag{10}$$

$$\boldsymbol{b}(\boldsymbol{x}_I) = \{b_1(\boldsymbol{x}_I) \quad b_2(\boldsymbol{x}_I) \quad \cdots \quad b_m(\boldsymbol{x}_I)\}^T \tag{11}$$

The RBF and the PBF are defined as:

$$\begin{aligned}\boldsymbol{r}(\boldsymbol{x}_I) &= \{r_1(\boldsymbol{x}_I) \quad r_2(\boldsymbol{x}_I) \quad \cdots \quad r_n(\boldsymbol{x}_I)\}^T \\ &= \{r(\boldsymbol{x}_1 - \boldsymbol{x}_I) \quad r(\boldsymbol{x}_2 - \boldsymbol{x}_I) \quad \cdots \quad r(\boldsymbol{x}_n - \boldsymbol{x}_I)\}^T\end{aligned} \tag{12}$$

$$\boldsymbol{p}(\boldsymbol{x}_I) = \{p_1(\boldsymbol{x}_I) \quad p_2(\boldsymbol{x}_I) \quad \cdots \quad p_m(\boldsymbol{x}_I)\}^T \tag{13}$$

The monomials in the PBF are determined by the three-dimensional Pascal's triangle represented in Figure 11. For instance, the PBF considering a quadratic basis for the three-dimensional case ($m = 10$) is defined as:

$$\boldsymbol{p}(\boldsymbol{x}_I) = \{1 \quad x \quad y \quad z \quad x^2 \quad xy \quad y^2 \quad yz \quad z^2 \quad zx\}^T \tag{14}$$

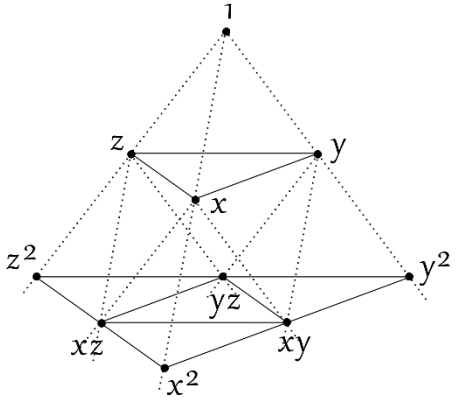

Figure 11 - Three-dimensional Pascal´s triangle of monomials

There are several RBF in the literatures. Within RPI meshless methods, the most common is the multi-quadrics RBF (MQ-RBF) [82]. The MQ-RBF is defined as:

$$r_i(\boldsymbol{x}_I) = \left({d_{iI}}^2 + (\gamma d_a)^2\right)^p \tag{15}$$

Being d_{iI} the distance between the field nodes and the interest point, γ and p the MQ-RBF shape parameters and d_a a coefficient that represents the size of the influence domain (RPIM) or influence cell (NNRPIM) of the interest point $\boldsymbol{x}_I$. The distance d_{iI} between the field nodes ($\boldsymbol{x}_i$) and the interest point ($\boldsymbol{x}_I$) is the only variable in RBF. For a three-dimensional space, this distance is calculated using the following expression:

$$d_{iI} = \sqrt{(x_i - x_I)^2 + (y_i - y_I)^2 + (z_i - z_I)^2} \tag{16}$$

The parameters γ and p need to be optimized to obtain accurate results. Works on the NNRPIM showed that γ should be close to zero and p should be close to one [45], [59]. However, γ and p cannot have the values zero and one since the use of these values leads to singular moment matrices. In this work the values $\gamma = 0{,}0001$ and $p = 1{,}0001$ are used [45]. Within meshless methods that use the influence domain concept (RPIM), d_a is defined as the average nodal spacing of the nodes n inside the support-domain of $\boldsymbol{x}_I$ and can be determined using the following equation [27], [45]:

$$d_a = \frac{D^{\frac{1}{d}}}{n^{\frac{1}{d}} - 1} \tag{17}$$

Being d the domain dimension and D the size of the support-domain. For the one-dimensional case D defines the length of the support-domain, for the two-dimensional case represents the support-domain area and for the three-dimensional case symbolizes the volume of the support-domain. In the NNRPIM, d_a is considered as the size of the Voronoï cell of the interest point $\boldsymbol{x}_I$. For the MQ-RBF, if $\boldsymbol{x}_I$ is an integration point, the coefficient d_a can be defined as the integration weight of $\boldsymbol{x}_I$ ($d_a = \widehat{w}_I$) [45]. The coefficients $\boldsymbol{a}(\boldsymbol{x}_I)$ and $\boldsymbol{b}(\boldsymbol{x}_I)$ are determined by imposing the function $u^h(\boldsymbol{x}_I)$ defined in Equation (9) to pass through all the n nodal values inside the support domain of $\boldsymbol{x}_I$. Thus, resorting to Equation (9) and imposing the n nodal values, a system of equations with $n + m$ unknowns is obtained:

$$\begin{cases} u^h(\boldsymbol{x}_1) = \sum_{i=i}^{n} r_i(\boldsymbol{x}_i - \boldsymbol{x}_1)a_i(\boldsymbol{x}_I) + \sum_{j=i}^{m} p_j(\boldsymbol{x}_1)b_j(\boldsymbol{x}_I) = u(\boldsymbol{x}_1) \\ u^h(\boldsymbol{x}_2) = \sum_{i=i}^{n} r_i(\boldsymbol{x}_i - \boldsymbol{x}_2)a_i(\boldsymbol{x}_I) + \sum_{j=i}^{m} p_j(\boldsymbol{x}_2)b_j(\boldsymbol{x}_I) = u(\boldsymbol{x}_2) \\ \vdots \\ u^h(\boldsymbol{x}_n) = \sum_{i=i}^{n} r_i(\boldsymbol{x}_i - \boldsymbol{x}_n)a_i(\boldsymbol{x}_I) + \sum_{j=i}^{m} p_j(\boldsymbol{x}_n)b_j(\boldsymbol{x}_I) = u(\boldsymbol{x}_n) \end{cases} \tag{18}$$

Which can be presented in the matrix form as:

$$\boldsymbol{R}\boldsymbol{a}(\boldsymbol{x}_I) + \boldsymbol{P}\boldsymbol{b}(\boldsymbol{x}_I) = \boldsymbol{u}_s \tag{19}$$

The RBF moment matrix $\boldsymbol{R}$ is defined as:

$$\boldsymbol{R} = \begin{bmatrix} r_1(\boldsymbol{x}_1) & r_2(\boldsymbol{x}_1) & \cdots & r_n(\boldsymbol{x}_1) \\ r_1(\boldsymbol{x}_2) & r_2(\boldsymbol{x}_2) & \cdots & r_n(\boldsymbol{x}_2) \\ \vdots & \vdots & \ddots & \vdots \\ r_1(\boldsymbol{x}_n) & r_2(\boldsymbol{x}_n) & \cdots & r_n(\boldsymbol{x}_n) \end{bmatrix} \tag{20}$$

Which for the MQ-RBF is defined as:

$$\boldsymbol{R} = \begin{bmatrix} \left({d_{11}}^2 + (\gamma d_c)^2\right)^p & \left({d_{12}}^2 + (\gamma d_c)^2\right)^p & \cdots & \left({d_{1n}}^2 + (\gamma d_c)^2\right)^p \\ \left({d_{21}}^2 + (\gamma d_c)^2\right)^p & \left({d_{22}}^2 + (\gamma d_c)^2\right)^p & \cdots & \left({d_{2n}}^2 + (\gamma d_c)^2\right)^p \\ \vdots & \vdots & \ddots & \vdots \\ \left({d_{n1}}^2 + (\gamma d_c)^2\right)^p & \left({d_{n2}}^2 + (\gamma d_c)^2\right)^p & \cdots & \left({d_{nn}}^2 + (\gamma d_c)^2\right)^p \end{bmatrix} \tag{21}$$

The polynomial moment matrix $\boldsymbol{P}$ is given by:

$$\boldsymbol{P} = \begin{bmatrix} p_1(\boldsymbol{x}_1) & p_2(\boldsymbol{x}_1) & \cdots & p_m(\boldsymbol{x}_1) \\ p_1(\boldsymbol{x}_2) & p_2(\boldsymbol{x}_2) & \cdots & p_m(\boldsymbol{x}_2) \\ \vdots & \vdots & \ddots & \vdots \\ p_1(\boldsymbol{x}_n) & p_2(\boldsymbol{x}_n) & \cdots & p_m(\boldsymbol{x}_n) \end{bmatrix} \tag{22}$$

The system of equations (18) has n equations and $m + n$ unknowns. Thus, an extra set of equations needs to be established as a consequence of a theorem of Duchon [45], [83] detailed in [84]. The following m equations can be added to the initial system:

$$\begin{cases} \sum_{i=1}^{n} p_1(\boldsymbol{x}_i) a_i(\boldsymbol{x}_I) = p_1(\boldsymbol{x}_1) a_1(\boldsymbol{x}_I) + \cdots + p_1(\boldsymbol{x}_n) a_n(\boldsymbol{x}_I) = 0 \\ \sum_{i=1}^{n} p_2(\boldsymbol{x}_i) a_i(\boldsymbol{x}_I) = p_2(\boldsymbol{x}_1) a_1(\boldsymbol{x}_I) + \cdots + p_2(\boldsymbol{x}_n) a_n(\boldsymbol{x}_I) = 0 \\ \vdots \\ \sum_{i=1}^{n} p_m(\boldsymbol{x}_i) a_i(\boldsymbol{x}_I) = p_m(\boldsymbol{x}_1) a_1(\boldsymbol{x}_I) + \cdots + p_m(\boldsymbol{x}_n) a_n(\boldsymbol{x}_I) = 0 \end{cases} \tag{23}$$

Which can be expressed in matrix form as:

$$\boldsymbol{P}^T \boldsymbol{a}(\boldsymbol{x}_I) = 0 \tag{24}$$

Equations (19) and (24) can be assembled to obtain the following set of $n + m$ equations with $n + m$ unknowns:

$$\begin{bmatrix} \boldsymbol{R} & \boldsymbol{P} \\ \boldsymbol{P^T} & \boldsymbol{0} \end{bmatrix} \begin{Bmatrix} \boldsymbol{a}(\boldsymbol{x}_I) \\ \boldsymbol{b}(\boldsymbol{x}_I) \end{Bmatrix} = \boldsymbol{M_T} \begin{Bmatrix} \boldsymbol{a}(\boldsymbol{x}_I) \\ \boldsymbol{b}(\boldsymbol{x}_I) \end{Bmatrix} = \begin{Bmatrix} \boldsymbol{u}_s \\ \boldsymbol{0} \end{Bmatrix} \tag{25}$$

The coefficients $\boldsymbol{a}(\boldsymbol{x}_I)$ and $\boldsymbol{b}(\boldsymbol{x}_I)$ are obtained from Equation (25):

$$\begin{Bmatrix} \boldsymbol{a}(\boldsymbol{x}_I) \\ \boldsymbol{b}(\boldsymbol{x}_I) \end{Bmatrix} = \boldsymbol{M_T}^{-1} \begin{Bmatrix} \boldsymbol{u}_s \\ \boldsymbol{0} \end{Bmatrix} \tag{26}$$

Substituting the coefficients $\boldsymbol{a}(\boldsymbol{x}_I)$ and $\boldsymbol{b}(\boldsymbol{x}_I)$ obtained in Equation (26) into Equation (9), Equation (9) can be rewritten as:

$$u^h(\boldsymbol{x}_I) = \{\boldsymbol{r}(\boldsymbol{x}_I)^T \quad \boldsymbol{p}(\boldsymbol{x}_I)^T\} \begin{Bmatrix} \boldsymbol{a}(\boldsymbol{x}_I) \\ \boldsymbol{b}(\boldsymbol{x}_I) \end{Bmatrix} = \{\boldsymbol{r}(\boldsymbol{x}_I)^T \quad \boldsymbol{p}(\boldsymbol{x}_I)^T\} \boldsymbol{M_T}^{-1} \begin{Bmatrix} \boldsymbol{u}_s \\ \boldsymbol{0} \end{Bmatrix} \tag{27}$$

The interpretation of Equation (27) permit to identify the interpolation functions vectors:

$$u^h(\boldsymbol{x}_I) = \{\boldsymbol{r}(\boldsymbol{x}_I)^T \quad \boldsymbol{p}(\boldsymbol{x}_I)^T\} \boldsymbol{M_T}^{-1} \begin{Bmatrix} \boldsymbol{u}_s \\ \boldsymbol{0} \end{Bmatrix} = \{\varphi(\boldsymbol{x}_I)^T \quad \psi(\boldsymbol{x}_I)^T\} \begin{Bmatrix} \boldsymbol{u}_s \\ \boldsymbol{0} \end{Bmatrix} \tag{28}$$

The interpolation vector $\varphi(\boldsymbol{x}_I)^T$ and the byproduct vector $\psi(\boldsymbol{x}_I)^T$ are defined as:

$$\boldsymbol{\varphi}(\boldsymbol{x}_I)^T = \{\varphi_1(\boldsymbol{x}_I) \quad \varphi_2(\boldsymbol{x}_I) \quad \cdots \quad \varphi_n(\boldsymbol{x}_I)\} \tag{29}$$

$$\boldsymbol{\psi}(\boldsymbol{x}_I)^T = \{\psi_1(\boldsymbol{x}_I) \quad \psi_2(\boldsymbol{x}_I) \quad \cdots \quad \psi_m(\boldsymbol{x}_I)\} \tag{30}$$

The byproduct vector can be completely negligible since it is multiplied by the null vector in Equation (28). Therefore, the field variable $\boldsymbol{u}$ is interpolated for an interest point $\boldsymbol{x_I}$ by the following expression:

$$\boldsymbol{u}^h(\boldsymbol{x}_I) = \sum_{i=1}^{n} \varphi_i(\boldsymbol{x}_I)\boldsymbol{u}(\boldsymbol{x}_i) = \boldsymbol{\varphi}(\boldsymbol{x}_I)^T \boldsymbol{u}_S \tag{31}$$

2.1.7 SOLID MECHANICS

In this section, the procedure to obtain the final discrete set of equations is described. The methodology employed by the meshless method is equal to the one used by the FEM. The methods used in the present work resort to the Galerkin weak form formulation to determine the discrete system of equations. As in the FEM, the essential and natural boundary conditions can be directly imposed, since the RPI shape functions possess the Kronecker delta property.

2.1.7.1 THREE-DIMENSIONAL ELASTICITY THEORY

Consider a solid with domain Ω bounded by Γ. The equilibrium equations for the linear elasto-static problem are defined as:

$$\nabla\boldsymbol{\sigma} + \boldsymbol{b} = 0 \tag{32}$$

Being ∇ the gradient operator, $\boldsymbol{\sigma}$ the Cauchy stress tensor and $\boldsymbol{b}$ the body force per unit volume vector. The boundary conditions are given by:

$$\begin{aligned} \boldsymbol{\sigma n} &= \bar{\boldsymbol{t}} \text{ on the natural boundary } \Gamma_t \\ \boldsymbol{u} &= \bar{\boldsymbol{u}} \text{ on the essential boundary } \Gamma_u \end{aligned} \tag{33}$$

Being $\bar{\boldsymbol{u}}$ the prescribed displacement on Γ_u, $\bar{\boldsymbol{t}}$ the traction on Γ_t and $\boldsymbol{n}$ the unit outward vector normal to the boundary of domain Ω. The Cauchy stress tensor $\boldsymbol{\sigma}$ is defined in Voigt notation as:

$$\boldsymbol{\sigma} = \{\sigma_{xx} \quad \sigma_{yy} \quad \sigma_{zz} \quad \tau_{xy} \quad \tau_{yz} \quad \tau_{zx}\}^T \tag{34}$$

The material constitutive relation is defined as:

$$\boldsymbol{\sigma} = \boldsymbol{c\varepsilon} \tag{35}$$

Being $\boldsymbol{c}$ the material constitutive matrix. Considering the three-dimensional problem:

$$\boldsymbol{c} = \mu_1 \begin{bmatrix} 1 & \upsilon & \upsilon & 0 & 0 & 0 \\ \upsilon & 1 & \upsilon & 0 & 0 & 0 \\ \upsilon & \upsilon & 1 & 0 & 0 & 0 \\ 0 & 0 & 0 & \mu_2 & 0 & 0 \\ 0 & 0 & 0 & 0 & \mu_2 & 0 \\ 0 & 0 & 0 & 0 & 0 & \mu_2 \end{bmatrix} \tag{36}$$

Where $\mu_1 = \frac{E}{1-\upsilon^2}$ and $\mu_2 = \frac{1-\upsilon}{2}$. The deformations vector is defined as:

$$\boldsymbol{\varepsilon} = \{\varepsilon_{xx} \quad \varepsilon_{yy} \quad \varepsilon_{zz} \quad \gamma_{xy} \quad \gamma_{yz} \quad \gamma_{zx}\}^T \tag{37}$$

The displacements are naturally related to the deformations by the following constitutive relation:

$$\boldsymbol{\varepsilon} = \boldsymbol{L}\boldsymbol{u} \tag{38}$$

Being $\boldsymbol{u} = \{u \quad v \quad w\}$ and $\boldsymbol{L}$ the differential operator matrix:

$$\boldsymbol{L} = \begin{bmatrix} \frac{\partial}{\partial x} & 0 & 0 & \frac{\partial}{\partial y} & 0 & \frac{\partial}{\partial z} \\ 0 & \frac{\partial}{\partial y} & 0 & \frac{\partial}{\partial x} & \frac{\partial}{\partial z} & 0 \\ 0 & 0 & \frac{\partial}{\partial z} & 0 & \frac{\partial}{\partial y} & \frac{\partial}{\partial x} \end{bmatrix}^T \tag{39}$$

2.1.7.2 DISCRETE SYSTEM OF EQUATIONS

Within the FEM, RPIM and NNRPIM methods, the partial differential equations ruling the physical phenomenon are established in the Galerkin weak form formulation. Considering equation (32), the Galerkin weak form is presented as [45]:

$$\psi = \int_{\Omega} \delta\varepsilon^T \boldsymbol{\sigma} d\Omega - \int_{\Omega} \delta\boldsymbol{u}^T \sigma b\Omega - \int_{\Gamma_t} \delta\boldsymbol{u}^T \boldsymbol{t} d\Gamma = 0 \tag{40}$$

Equation (40) can be developed and presented as:

$$\psi = \delta\boldsymbol{u}^T(\boldsymbol{K}\boldsymbol{u} - \boldsymbol{f_b} - \boldsymbol{f_t}) = 0 \tag{41}$$

Which leads to a linear set of equations that can be represented in the form:

$$\boldsymbol{K}\boldsymbol{u} = \boldsymbol{f_b} + \boldsymbol{f_t} \tag{42}$$

Being $\boldsymbol{K}$ the global stiffness matrix, which after manipulation [45] the first term of equation (40) allows to achieve the following equation:

$$\boldsymbol{K} = \int_{\Omega} \boldsymbol{B}^T \boldsymbol{c} \boldsymbol{B} d\Omega = \sum_{I=1}^{n_Q} \boldsymbol{B}(\boldsymbol{x}_I)^T \boldsymbol{c} \boldsymbol{B}(\boldsymbol{x}_I) \widehat{w_I} \tag{43}$$

Where $\boldsymbol{B}$ is the deformability matrix defined as:

$$\boldsymbol{B} = \begin{bmatrix} \frac{\partial \varphi_1(\boldsymbol{x}_I)}{\partial x} & 0 & 0 & \cdots & \frac{\partial \varphi_n(\boldsymbol{x}_I)}{\partial x} & 0 & 0 \\ 0 & \frac{\partial \varphi_1(\boldsymbol{x}_I)}{\partial y} & 0 & \cdots & 0 & \frac{\partial \varphi_n(\boldsymbol{x}_I)}{\partial y} & 0 \\ 0 & 0 & \frac{\partial \varphi_1(\boldsymbol{x}_I)}{\partial z} & \cdots & 0 & 0 & \frac{\partial \varphi_n(\boldsymbol{x}_I)}{\partial z} \\ \frac{\partial \varphi_1(\boldsymbol{x}_I)}{\partial y} & \frac{\partial \varphi_1(\boldsymbol{x}_I)}{\partial x} & 0 & \cdots & \frac{\partial \varphi_n(\boldsymbol{x}_I)}{\partial y} & \frac{\partial \varphi_n(\boldsymbol{x}_I)}{\partial x} & 0 \\ 0 & \frac{\partial \varphi_1(\boldsymbol{x}_I)}{\partial z} & \frac{\partial \varphi_1(\boldsymbol{x}_I)}{\partial y} & \cdots & 0 & \frac{\partial \varphi_n(\boldsymbol{x}_I)}{\partial z} & \frac{\partial \varphi_n(\boldsymbol{x}_I)}{\partial y} \\ \frac{\partial \varphi_1(\boldsymbol{x}_I)}{\partial z} & 0 & \frac{\partial \varphi_1(\boldsymbol{x}_I)}{\partial x} & \cdots & \frac{\partial \varphi_n(\boldsymbol{x}_I)}{\partial z} & 0 & \frac{\partial \varphi_n(\boldsymbol{x}_I)}{\partial x} \end{bmatrix} \tag{44}$$

The second and third term of equation (40) permit to define [45] the body force $\boldsymbol{f_b}$ and external force $\boldsymbol{f_t}$ vectors as:

$$\boldsymbol{f_b} = \int_{\Omega} \boldsymbol{H}^T \boldsymbol{b} d\Omega = \sum_{I=1}^{n_Q} \boldsymbol{H}(\boldsymbol{x}_I)^T \boldsymbol{b} \widehat{w_I} \tag{45}$$

$$\boldsymbol{f_t} = \int_{\Gamma} \boldsymbol{H}^T \bar{\boldsymbol{t}} d\Gamma = \sum_{I=1}^{n_{Q^*}} \boldsymbol{H}(\boldsymbol{x}_I)^T \boldsymbol{f} \widehat{w_I^*} \tag{46}$$

Being $\widehat{w_I^*}$ the weight of the integration point at the curve/surface at which the traction force $\boldsymbol{f_t}$ is being applied, n_{Q^*} is the number of integration points defining that traction boundary and $\boldsymbol{H}$ the interpolation matrix defined as:

$$\boldsymbol{H} = \begin{bmatrix} \varphi_1 & 0 & 0 & \varphi_2 & 0 & 0 & \cdots & \varphi_n & 0 & 0 \\ 0 & \varphi_1 & 0 & 0 & \varphi_2 & 0 & \cdots & 0 & \varphi_n & 0 \\ 0 & 0 & \varphi_1 & 0 & 0 & \varphi_2 & \cdots & 0 & 0 & \varphi_n \end{bmatrix} \tag{47}$$

The essential boundary conditions can then be imposed directly in the global stiffness matrix, since the RPI shape functions possess the Kronecker delta property.

2.2 STRUCTURAL OPTIMIZATION

In the present section, a review on the state of the art of structural optimization is presented. The most used optimization algorithms are mentioned and the historical background of the optimization method to be used in the practical work is outlined. Afterwards, a review on the implementation of meshless methods in optimization is presented. Finally, some recent practical applications of structural optimization are given, showing that structural optimization is a viable design tool in industry.

2.2.1 STATE OF THE ART

Structural optimization has been a topic of high interest in the computational mechanics and engineering community. Figure 12 demonstrates the research interest that structural optimization has had since its initial developments [21]. Structural optimization started to significantly develop since the 1990s and the research on the topic have been increasing exponentially to the present days. Since 2010, the number of publications has been increasing significantly. The inclusion of structural optimization modules in most used commercial structural analysis packages has contributed to an increase of the number of publications on structural optimization techniques in both academic research and practical applications.

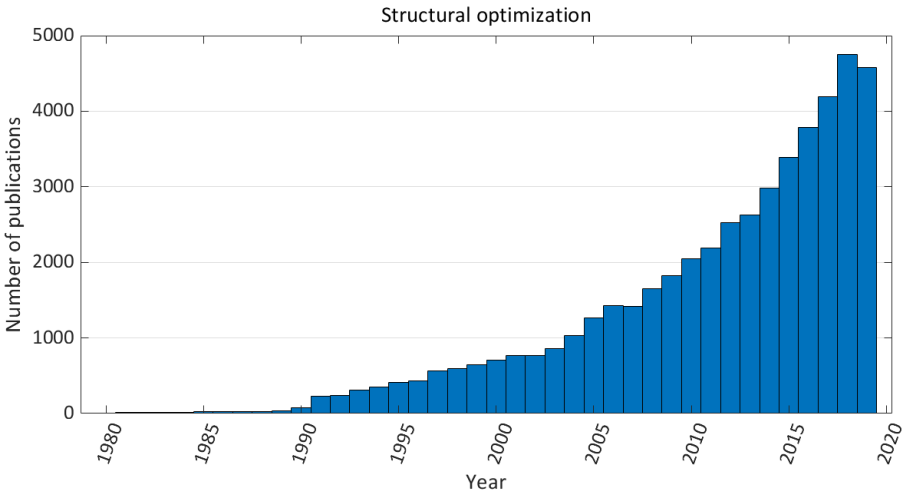

Figure 12 - Number of publications per year on structural optimization since 1990 [21]

The search for the optimal component design is a continuous engineering challenge. Thus, several mathematical optimization models [85], [86] have been developed in order to find optimal and cost-efficient designs. The first work on topology optimization was developed by Michell in 1904 [87]. Michell addressed the problem of least volume topology of trusses. However, the work was purely theoretical and had no practical applications given that no computational resources were available to implement it. In 1972, Rozvany [88] extended Michell's theory on trusses and beam systems. Rozvany also introduced the first general theoretical background of topology optimization called "optimal layout theory" [89]. A huge evolution in the field of topology optimization started after Rozvany's work [90]. The paper by Bendsøe and Kikuchi [91] on the homogenization method is considered a seminal work in topology optimization. Since then several methods have been developed in the structural optimization field. The Solid

Isotropic Microstructures with Penalization (SIMP) method [92]–[94] is a variant of the homogenization method and is one of the most common techniques in structural optimization. Due to its simplicity and ease of implementation the SIMP method is one of the most used optimization methods. Other developed optimization algorithms include Evolutionary procedures [95]–[99], topological derivative (bubble method) [100]–[102] and boundary variational methods such as the level-set method [103]–[107] and the phase field method [108], [109]. Genetic Algorithms (GA) [110], [111] were also developed. More recently, highly demanding discretization techniques were combined with optimization techniques, such as Isogeometric Analysis (IGA) [112], [113], allowing to develop new integrated approaches. Several reviews on the various structural optimization procedures can be found in the literature [114], [115].

The optimization algorithm used in this dissertation is an evolutionary algorithm. The Evolutionary Structural Optimization (ESO) method was originally proposed by Xie and Steven in 1993 [95]. The ESO technique is based on the concept of gradually removing inefficient material from the structure, thus evolving it to an optimal design. As an improvement of the original ESO, a bi-directional ESO (BESO) approach was proposed by Querin *et al* [96] and Yang *et al* [97]. The BESO allows both material removal and addiction simultaneously, thus permitting the recovery of deleted elements. Although the BESO method is a more generalized approach, it is very computational demanding when compared with the simpler ESO method. However, the ESO has significant limitations in some optimization problems due to its inherent unidirectional procedure. So, the original algorithm has been extensively modified in order to circumvent its original problems.

2.2.2 THE “HARD-KILL” METHOD

The ESO method is a discrete optimization approach in which inefficient elements are gradually removed at each iteration. Since inefficient elements are instantly deleted at each iteration, the ESO method is usually referred as the “hard-kill” method. The ESO method is a heuristic or intuitive optimization method, since there is no proof that an optimal design is achieved after several iterations. Being a heuristic optimization method, typically the original ESO method hardly results in convergent solutions. This means that the final solution cannot be further improved under the given update algorithms. The limitation of the ESO is that removed material cannot be recovered in subsequent iterations. Hence, if a portion of material is wrongly removed in early iterations, the algorithm may not result in an optimal design. In the literature is commonly stated that a problem within evolutionary procedures is the lack of algorithmic convergence and selection of appropriate stopping criteria [114]. Some critiques on the original ESO and BESO methods were reported by Rozvany in [116]. Although optimal solutions are not guaranteed within the original ESO, efficient designs can still be obtained. The early ESO algorithm has been intensively modified in order to surpass its inherent drawbacks related to its unidirectional approach. The ESO algorithm to be used in the present work has been extensively modified and intends to produce optimal solutions while being computational efficient.

The ESO showed to be a viable optimization method in a work by Li [117]. In 2016, Li used an ESO method in the design of the lower chassis of a Monorail Personal Rapid Transit (MPRT) car. Several load cases were considered in order to achieve a better overall performance of the structure. The implementation of the ESO method resulted in an optimized structure with 80% less volume than the original chassis (Figure 13). The final design was analysed using the FEM. An acceptable stress distribution as well as an efficient material distribution were obtained showing that the ESO method was implemented successfully. Presently, the ESO method is a viable optimization algorithm despite some of its reported drawbacks.

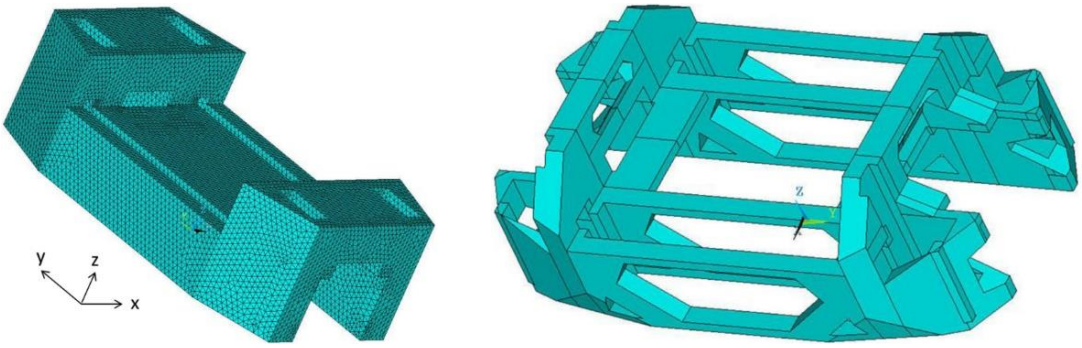

Figure 13 - (a) Finite element model of the lower chassis; (b) Optimized topology of the lower chassis redesigned [117]

2.2.3 NUMERICAL METHODS IN STRUCTURAL OPTIMIZATION

The structural analysis is a fundamental module in the structural optimization procedure. An accurate numerical simulation of the structure at each iteration deeply contributes to the final optimal solution. Thus, several numerical techniques have been employed in order to obtain the most optimal solutions out of the optimization algorithms. The first works on structural optimization employed element-based approaches to analyse the structure after each iteration. The first work implementing the FEM into structural optimization was published in 1973 by Zienkiewicz and Campbell [118]. In this work, the authors defined the design variables as the nodal coordinates of the finite element discretization. The community rapidly recognized that the FEM was not very well suited to structural optimization applications. In structural optimization, the structure's geometry is continuously changing through sequential iterations. Thus, when using the FEM, a frequent remeshing is needed in order to avoid highly distorted elements. Other techniques besides the FEM were implemented in order to overcome the limitations of the FEM in structural optimization problems. By mid 1980s, the Boundary Element Method (BEM), which offers several advantages over the FEM, was applied to structural optimization [119]–[124]. Since the beginning of the millennium, a new class of numerical methods has been successfully implemented in structural optimization procedures.

2.2.3.1 MESHLESS METHODS IN STRUCTURAL OPTIMIZATION

A meshless method was firstly used in structural optimization in 1998 [125], [126]. In these works, Grindeanu *et al.* developed a continuum-based design sensitivity analysis (DSA) method combined with the RKPM [30] for the structural analysis. The work focused on the analysis of hyper elastic structures. Thus, the authors intended to use a meshless method over the FEM since meshless methods proved to produce more accurate solutions in problems involving large deformations. To validate the proposed method, the optimization of an engine mount was carried out. The results obtained demonstrated the potential of using meshless methods within structural optimization in order to avoid mesh distortion problems characteristic of the FEM. Subsequently, the RKPM was further extended to the structural optimization field in the analysis of two- and three-dimensional problems [127]–[130]. The RKPM was also combined with a structural optimization method for geometrically non-linearly structures [131].

In 2007, the RKPM as well as a RKPM based on a truly meshless integration technique [132], [133] were used in the shape optimization of continua [130]. To validate the proposed method, the authors addressed the benchmark filet shape optimization problem. Table 1 [130] presents the results for the filet problem obtained with the proposed method as well as with previous studied approaches. The proposed truly meshless method results in higher convergence rates than the classical RKPM and demonstrated to be an efficient approach for shape optimization.

Table 1 - Comparison of results for the filet shape optimization problem [130]

Method employed	Final areas (mm^2)	Iteration number	Total time (s)
BEM (1991) [122]	about 670 (45,8%)	-	-
EFG (1999) [134]	about 550 (37,6%)	15	-
RKPM [130]	546 (37,3%)	13	3110
Truly meshless method [130]	520,5 (35,5%)	7	1860

Concerning approximant meshless methods, the EFGM [33] has been successfully applied in structural optimization. The EFGM was introduced for the first time into the structural optimization field in 2001. Bobaru and Mukherjee [134] also used a DSA approach for the design optimization of two-dimensional elastic problems. In this work, the benchmark example of the shape optimization of a filet [122] was studied . The accurate and smooth solutions obtained resorting to the meshless method are referenced as impossible to obtain using the conventional FEM and BEM numerical methods. In the following year, the same authors used the EFGM in the shape optimization of linear thermoelastic solids [135]. Later Bobaru and Rachakonda applied the EFGM in a new fixed-grid shape optimization method [136]. In the following years, the EFGM was used in several studies on topology optimization [137]–[141].

More recently, the EFGM was combined with the BESO method for the topology optimization of continuum structures [142]. This work presents benchmark beam problems to validate the proposed methodology. The solutions obtained are then compared with ones from the SIMP approach (Figure 14). The proposed method successfully eliminates checkerboard patterns without any sensitivity filtering, which are common features of the SIMP method. Also, the presented method is mesh independent since the obtained results proved to be independent of the nodal discretization used as Figure 15 demonstrates. In 2017, the EFGM was implemented in multi-material optimization [143] as well as on the optimization of continuum structures with displacement constraints [144]. The numerical examples within these works demonstrate the feasibility of the proposed meshless approaches.

(a) (b) (c)

Figure 14 - Solutions for numerical example one in [142]: (a) SIMP without sensitivity filtering; (b) SIMP with sensitivity filtering; (c) Proposed BESO method.

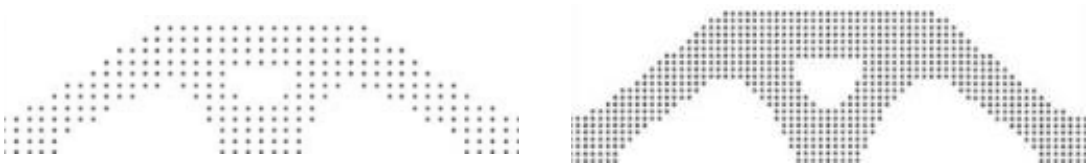

(a) (b)

Figure 15 – Optimization solutions considering different discretizations [142]: (a) Optimization solution for a 41×21 discretization; (b) Optimization solution for a 71×36 discretization

A few works implementing several variants of the MLPG meshless method in the topology optimization of structures are available in the literature [145]–[149]. In 2008, Li and Atluri solved several beam optimization problems using a MLPG “mixed collocation” method [149]. Although the presented method requires sensitivity filtering, the results demonstrate the convergence and stability of the method. Almost simultaneously, the authors used the MLPG “mixed collocation” method for material orientation and topology optimization of anisotropic solids and structures in [146]. One year later, a Finite Volume MLPG (FVMLPG) method was combined with the SIMP optimization method for the topology optimization of continuum structures [147]. As Figure 16 demonstrates, the proposed method effectively eliminates checkerboard pattern arising in the FEM as well as checkerboard pattern with point state arising in the RPIM.

As a development of the MLPG method, an interpolator Natural Neighbour Petrov-Galerkin (NNPG) method was employed in structural optimization analysis in [145], [148]. In 2008, a shape design sensitivity analysis using the NNPG was carried out to solve two-dimensional elastic problems [145]. Within the proposed method, neither background integration meshes or assembly processes to generate the global stiffness

matrix are needed, as well as no user-defined parameters are used. The shape optimization of a filet problem is studied and used to validate the presented method. In 2010, the NNPG method combined with the SIMP approach was extended to the topology optimization of moderately thick plates [148]. The proposed method prevents checkerboard patterns without using sensitivity filtering and demonstrated to produce accurate solutions for the topology optimization of plates.

(a) (b) (c)

Figure 16 - Optimization of a cantilever beam with a concentrated force applied at the right lower corner [147]: (a) Solution using the FVMLPG proposed method [147]; (b) Solution with the FEM; Solution with the RPIM

Regarding particle meshless methods, the SPH method [28] was extended to the topology optimization of plane structures in 2016 [150]. The SIMP approach with a sensitivity filter to eliminate checkerboard patterns was used to solve elastic topology optimization examples. To validate the proposed method a simply supported beam, a cantilever beam and an L-shaped beam are optimized. The results obtained using the SPH method are compared with the ones obtained with classical finite element analysis (Figure 17). In the cantilever beam example, a meshless Galerkin method solution from [138] is used for comparison. The results obtained from the numerical examples permit to conclude that the proposed optimization method based on the SPH meshless method is efficient and stable without the need of sensitivity filters. Also, the method is mesh-independent since final topologies do not depend on the refinement of the discretization used.

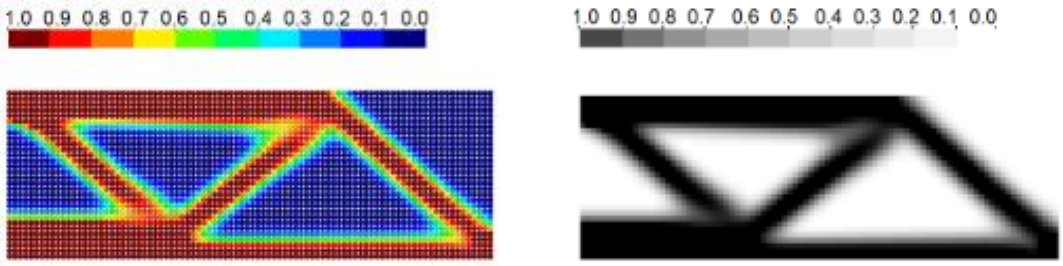

(a) (b)

Figure 17 - Optimization of a simply supported beam: (a) Topology optimization using SPH [150]; (b) Topology optimization using FEM [151]

2.2.3.2 RPIM IN STRUCTURAL OPTIMIZATION

Concerning the RPIM and NNRPIM meshless methods, very few works on structural optimization have been developed. However, in the literature one can find a work combining the RPIM with the SIMP method [152] as well as another one combining the RPIM with an "hard-kill" method [153]. In 2008, the same authors that used the FVMLPG method [147] also applied the RPIM to the topology optimization of structures [152]. In this work, Zheng *et al.* combined the RPIM with the SIMP optimization method for the design optimization of elastostatic continuum structures. The final solutions were obtained using the optimality criteria method [93]. To validate the proposed method, two cantilever beam examples were solved. Figure 18 demonstrates the ability of the proposed method to eliminate checkerboard patterns present in the FEM solutions when no sensitivity filtering is used. However, it is referred that the computational time is higher. The solution for a cantilever beam with a concentrated force applied at the right lower corner (Figure 19) obtained with the proposed method is compared with the one obtained by the RPIM with the design variable being the densities of the Gauss quadrature points. Figure 19 demonstrates that the proposed method successfully eliminates checkerboard pattern with point state arising in the different RPIM approach.

Figure 18 - Cantilever beam with a concentrated force applied on the middle of the free end solutions: (a) Optimization result by proposed method; (b) Optimization result by FEM; (c) Optimization result by FEM by sensitivity filtering [152]

Figure 19 - (a) Cantilever beam with a concentrated force applied at the right lower corner solutions: (a) Optimization result by proposed method; (b) Optimization result by RPIM with the densities of the Gauss quadrature points as a design variable [152]

A work combining the RPIM with an evolutionary hard-kill method, which is the purpose of the present dissertation, is presented by Lee *et al.* in [153]. In this work, the optimization of two-dimensional trusses is presented. Initially, a study of the influence of the number of field nodes on the final solutions is carried out for a cantilever beam example. The final topology solutions for different field nodes permit to conclude that a higher number of field nodes eliminates unwanted noises on the model and a more defined image is obtained (Figure 20).

(a) (b)

Figure 20 - Effect of the number of field nodes on the optimum topology: (a) 187 field nodes; (b) 693 field nodes [153]

The effect of the removing rate on the optimum topologies is studied considering a simply supported beam problem. Based on the results, the authors conclude that the final topologies vary significantly with the removing rate employed. Figure 21 shows that different topologies for the simply supported beam were achieved for different removing rates.

(a) (b)

Figure 21 - Effect of the removing rate on the optimum topology: (a) 0,01 at iteration 96; (b) 0,04 at iteration 24 [153]

Although the NNRPIM is a well-established meshless method in various engineering applications, works on structural optimization using the NNRPIM are still to develop. The present dissertation aims to implement the NNRPIM in the topology optimization of structures, thus extending the NNRPIM to the structural optimization field.

2.2.4 INNOVATIVE APPLICATIONS IN INDUSTRY

Structural optimization is an engineering tool that is already being used in industry. Due to the inclusion of optimization modules in commercial structural analysis packages such as Abaqus, Ansys and Solidworks, as well as the advancements in the additive manufacturing industry, structural optimization is currently a viable design technique that is being used in practical applications. The present section intends to introduce several recent industrial applications of structural optimization that represent the trends in current structural optimization applications.

2.2.4.1 AIRCRAFT BRACKET OPTIMIZATION (2016)

The topology of an aircraft bracket was optimized by Seabra *et al.* [154]. The optimized component was produced through additive manufacturing and mechanical tests were carried out to validate the proposed design. Within the optimization methodology, three load cases were considered being the objective function the weighted compliance. The topology optimization resulted in a volume reduction of 54% of the original component (Figure 22). This work highlights the benefits that additive manufacturing can provide to topology optimization in the means that it can produce highly complex geometries and justify the implementation of topology optimized designs in the industry.

(a) (b)

Figure 22 – Aircraft bracket: (a) Mesh of the original component; (b) Mesh of the optimized component [154]

2.2.4.2 TRANSMISSION GEARBOX OPTIMIZATION (2018)

In [155] the topology optimization of transmission gearbox was carried out by Liang *et al*. The topology optimization module from Abaqus is used, in which a variable density method is used due to its computational efficiency. The optimization resulted in a 7,6% mass reduction while maintaining the stiffness and dynamic performance of the gearbox. The initial design as well as the optimized one are shown in Figure 23. The numerical results obtained are presented in Table 2. This work shows that structural optimization methods can be applied not only to transmission gearboxes but also in the general vehicle system to produce lightweight designs with equal or increased performance.

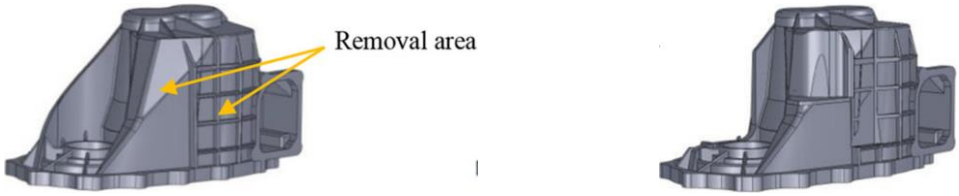

(a) (b)

Figure 23 - Transmission gearbox: (a) Initial design; (b) Optimized design [155]

Table 2 - Transmission gearbox optimization results [155]

Dynamic performance index	Initial model	Optimized model	Change rate (%)
Mass (kg)	9,85	9,10	-7,6
Maximum stress (MPa)	158	158	0
Maximum displacement (mm)	0,94	0,89	-5,3

2.2.4.3 BRAKE PEDAL OPTIMIZATION (2018)

The topology optimization of a brake pedal is presented in a work by Abdi *et al.* [156]. The objective of the work was to support the design and development of a brake pedal for a formula student race car program in De Montfort University. In this work, two optimization techniques were used: topology optimization and lattice structure design to stabilize the footpad area and reduce residual stress induced during manufacturing. The recently developed Iso-XFEM evolutionary topology optimization method was used.

The design of a brake pedal with a 15% of the initial design domain volume (close to original component) as well as one with 10% of the initial volume were studied. The topologies obtained are shown in Figure 24.

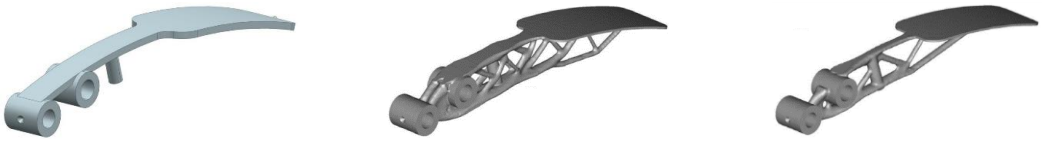

(a) (b) (c)

Figure 24 – Brake pedal: (a) Existing brake pedal model; (b) Optimized model with a 15% volume fraction; (c) Optimized model with a 10% volume fraction [156]

The results obtained for the three brake pedal designs in terms of volume, maximum von-Mises stress and compliance are presented in Table 3. The topology optimization solutions present increased performance compared with the existing component. Thus, this work shows that optimization techniques can be used to produce lighter automotive components with increased performance and that additive manufacturing is viable technique to produce the obtained complex designs.

Table 3 - Results for the three brake pedal designs [156]

	Volume (cm^3)	Max Von-Mises stress (MPa)	Compliance $(N.m)$
Existing pedal	72,1	5012	95,312
Optimized design $(VF = 0{,}15)$	70,8	458	0,994
Optimized design $(VF = 0{,}10)$	54,6	976	2,032

2.2.4.4 ROBOT ARM OPTIMIZATION (2019)

A widely used five degrees of freedom palletizing robot was optimized in [157]. The original model as well as the optimized one are shown in Figure 25. It was found that the deformation in the lower of the optimized design decreased in comparison with the initial design of the robot arm. The decrease in deformation leads to an increase of the robot precision and performance. Thus, the implementation of structural optimization techniques in the design process resulted in the weight reduction of the lower arm as well as in an increased mechanical performance of the robot.

(a) (b)

Figure 25 – Industrial robot: (a) Initial CAD model; (b) CAD model with optimized lower arm [157]

The analysis was performed considering three different materials: structural steel, aluminium alloy, and stainless steel. In Table 4 are presented the results obtained for the structural steel case, since it was the case in which the best results were achieved.

Table 4 - Robot arm optimization results considering structural steel [157]

	Total deformation (mm)	Stress (MPa)	Strain $(no\ units)$
Lower arm - solid type	0,0526	0,7392	4,72E-06
Lower Arm - Modified structure	0,04958	0,6539	4,10E-06

2.2.4.5 JABIRU LANDING GEAR AND ENGINE MOUNT OPTIMIZATION (2019)

In [158], Munk *et al.* developed a topology optimization algorithm to solve aerospace design problems. The landing gear of a Jabiru J160 as well as an engine mount for a Jabiru propeller powered 2200cc engine are optimized. The objective in both examples is minimum weight without failure while fulfilling the Federal Aviation Regulations. In this work the BESO algorithm was used to optimize the components topology. Figure 26 shows the final designs of the landing gear. Figure 26a demonstrates a design following conventional engineering principles while Figure 26b presents the computationally optimized design. In this work it was found that material is used more efficiently in the topologically optimized design. Moreover, in the conventional design high stresses are only present near the attachment point to the fuselage meaning that some material is not being structurally used. Contrarily, in the optimized design the stress is distributed uniformly. By implementing the topological optimized design, a 40% mass reduction is achieved in comparison with the standard engineering design. The optimization of the engine mount also resulted in a least weight design. The results obtained show that optimization techniques can produce significantly lighter components while complying with the regulations of the aircraft industry and demonstrate that topology optimization algorithms can be successfully used in aerospace design.

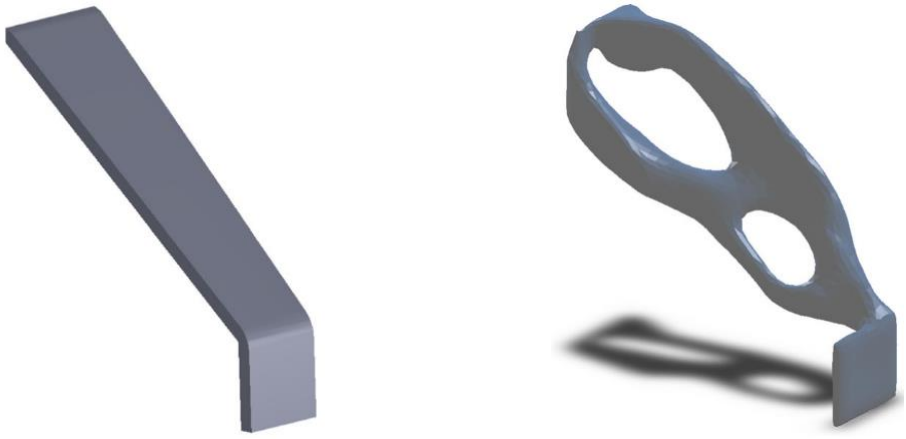

(a) (b)

Figure 26 - Final landing gear designs: (a) Engineering principles ; (b) Topology optimization solution [158]

DISSERTATION DEVELOPMENT

3 DISSERTATION DEVELOPMENT

In the following chapter, the practical work developed is presented. Initially, a preliminary convergence study is carried-out to validate the numerical methods and achieve a proficient level with the software used. Afterwards, the proposed structural optimization algorithm is applied to benchmark structural optimization examples, using the FEM, RPIM and NNRPIM. Finally, the developed methodology is extended to automotive and aircraft applications. The numerical examples were analysed in the provided software FEMAS (Finite Element and Meshless Analysis Software: cmech.webs.com), running in Matlab environment. The element and nodal meshes are created in FEMAP student edition v2020 (Finite Element Modelling And Postprocessing) and then imported to FEMAS, where all simulations are performed.

3.1 INTRODUCTORY CONVERGENCE STUDY

An introductory convergence study is presented to validate the proposed numerical methods (FEM, RPIM and NNRPIM). Hence, the linear-static analysis of a benchmark example with available analytical solutions is carried out considering both a two-dimensional approach, and a three-dimensional approach. The objectives of preliminary study are:

i. Achieve a proficient level with the software;
ii. Evaluate the convergence and accuracy of the proposed numerical methods in predicting displacement and stress fields;
iii. Compare the RPI meshless methods with the FEM solutions.

The cantilever beam submitted to a uniformly distributed load problem is considered (Figure 27). The dimensions of the beam are $L = 1\,m$ and $h = 0{,}05\,m$, corresponding to a length to height ratio of $L/h = 20$. The material elastic properties are $E = 1\,MPa$ and $\upsilon = 0{,}3$, and a uniformly distributed load of $P = 0{,}1\,N/m$ is applied along the length of the beam. The analytical solutions of the displacement and stress fields are can be found in the literature [159].

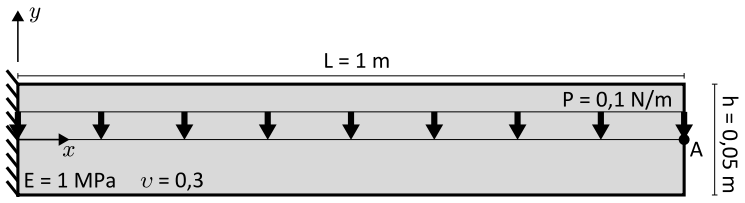

Figure 27 - Cantilever beam problem

The convergence of the numerical methods is evaluated by the vertical displacement at point A, for which analytical solution is given by:

$$v_A = \frac{PL^4}{8EI} \tag{48}$$

Where the moment of inertia of the cross section I is defined by:

$$I = \frac{h^3}{12}\text{, considering the 2D analysis}$$
$$I = \frac{bh^3}{12}\text{, considering the 3D analysis} \quad (49)$$

Being b the thickness of beam. Then, the relative error of the displacement at point A is calculated using the following expression:

$$Error\ [\%] = \frac{{v_A}^{numerical} - {v_A}^{analytical}}{{v_A}^{analytical}} \quad (50)$$

3.1.1 TWO-DIMENSIONAL ANALYSIS

Initially, the cantilever beam example is solved using the two-dimensional analysis, considering plane stress conditions. The problem is solved using the FEM, RPIM and NNRPIM. In the FEM analysis, a classic FEM formulation is used considering four node quadrilateral elements. The formulation of the used RPI meshless methods is described in detail in section 2.1. Regarding the RPIM, sixteen nodes inside the influence domains are considered and a Gaussian integration is performed resorting to quadrilateral integration cells with 2×2 integration points. In the NNRPIM analysis, second-degree influence cells and a full integration are considered. Concerning the RPI shape functions in RPIM and NNRPIM, the following parameters are assumed: $c = 0{,}0001$, $p = 0{,}9999$ and constant polynomial basis.

The problem is analysed considering regular meshes of 123, 495, 1449 and 5457 nodes. The vertical displacement values at point A and the respective relative errors are shown in Figure 28. Figure 29, Figure 30, Figure 31 and Figure 32 respectively show the normal stress along $y = h/2$, the normal stress along $x = L/2$, the shear stress along $y = 0$ and the shear stress along $x = L/2$.

As Figure 28 denotes, the NNRPIM demonstrates a significantly higher rate of convergence than the FEM and RPIM. With 405 nodes, the NNRPIM can perfectly predict the displacement at point A, whilst the FEM and RPIM still present a considerable error of 4%. If more refined meshes are employed, all methods converge to the exact solution. Yet, the increasingly computational time of the analysis may constraint the use of highly refined meshes, and high convergent methods may be used. Concerning the obtained stress fields, Figure 29 and Figure 30 show that the FEM, RPIM and NNRPIM have identical solutions regarding the normal stress σ_{xx}, being the relative error smaller as denser meshes are used. Slight errors occur at the extremes of the beam, due to discontinuity of the model. Nonetheless, with 1449 and 5457 nodes meshes, the FEM, RPIM and NNRPIM accurately predict the normal stress distribution. Regarding the shear stress τ_{xy} field, the same conclusions as for the normal stress distribution are withdrawn. The shear stress distribution along the beam height ($x = L/2$) present noticeable errors at $y = -h/2$ and $y = h/2$, yet the distribution is increasingly accurate as the number of nodes increases.

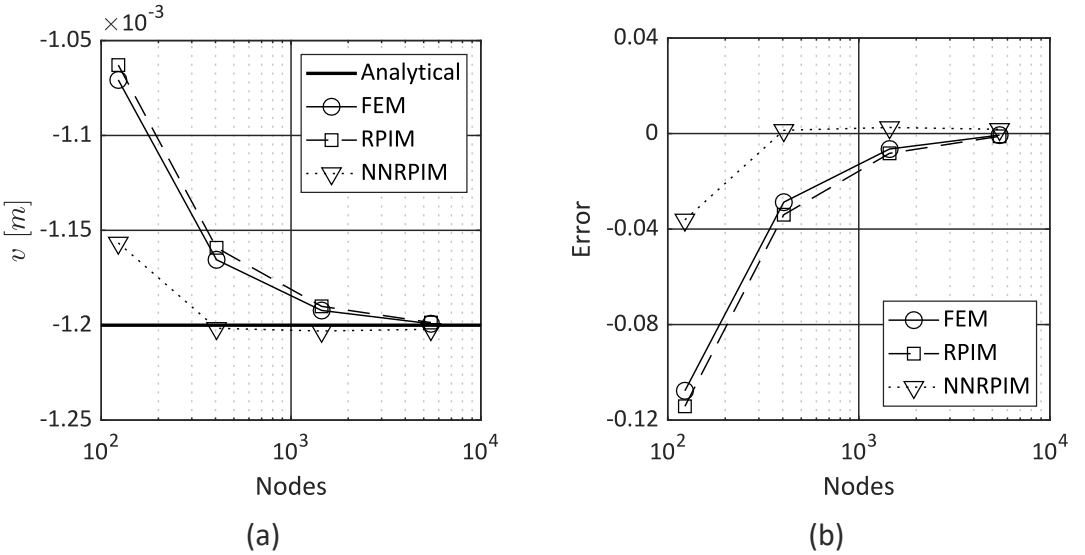

Figure 28 - (a) Displacement solutions at point A obtained with 123, 405, 1449 and 5457 nodes; (b) Relative error

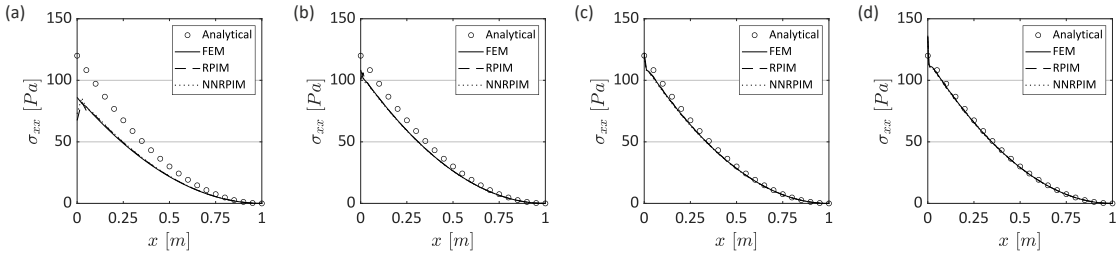

Figure 29 - Normal stress along y=h/2: (a) 123 nodes; (b) 405 nodes; (c) 1449 nodes; (d) 5457 nodes

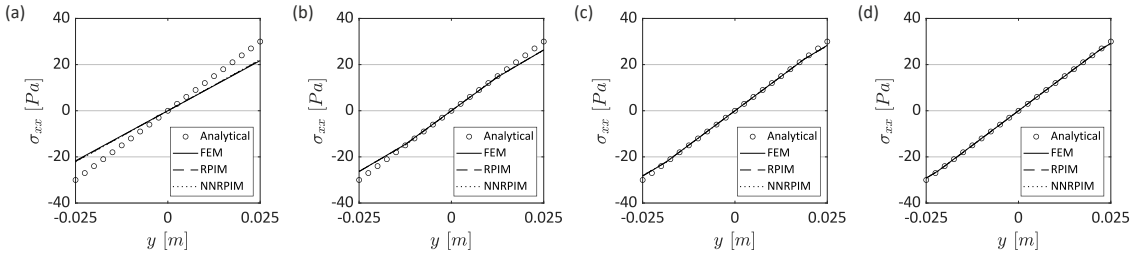

Figure 30 - Normal stress along x=L/2: (a) 123 nodes; (b) 405 nodes; (c) 1449 nodes; (d) 5457 nodes

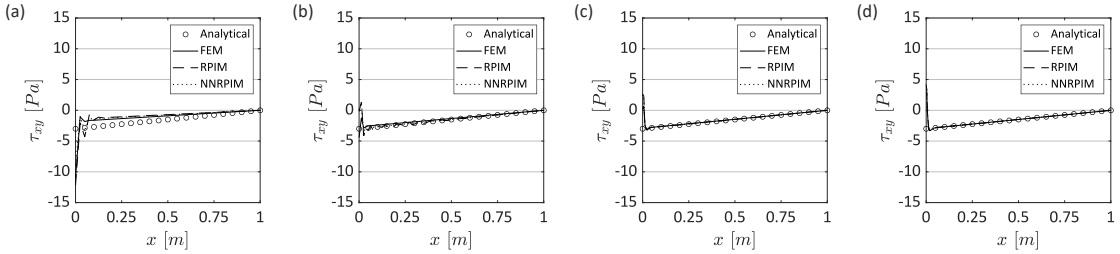

Figure 31 - Shear stress along y=0: (a) 123 nodes; (b) 405 nodes; (c) 1449 nodes; (d) 5457 nodes

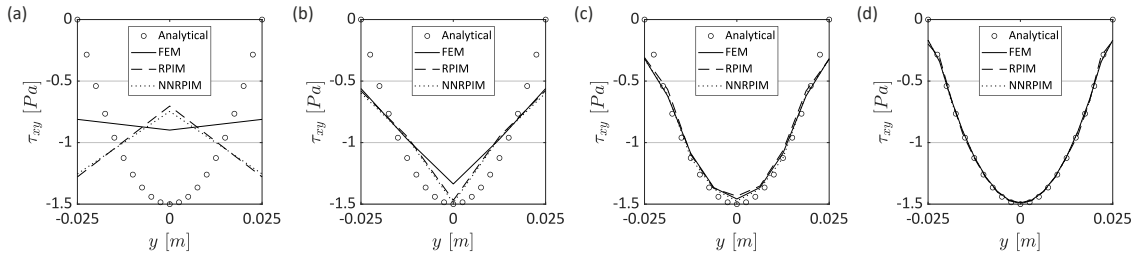

Figure 32 - Shear stress along x=L/2: (a) 123 nodes; (b) 405 nodes; (c) 1449 nodes; (d) 5457 nodes

3.1.2 THREE-DIMENSIONAL ANALYSIS

The cantilever beam problem is solved using the FEM, RPIM and NNRPIM considering the three-dimensional deformation theory. In the FEM analysis, a classical formulation is used considering eight node hexahedral elements. Regarding the RPIM, twenty-seven nodes inside the influence domains are considered, and Gaussian integration is performed resorting to hexahedral integration cells with $2 \times 2 \times 2$ integration points. In the NNRPIM analysis, second-degree influence cells and a full integration are considered. Concerning the RPI shape functions in RPIM and NNRPIM, the following parameters are assumed: $c = 0{,}0001$, $p = 0{,}9999$ and constant polynomial basis.

The problem is analysed considering regular meshes of 369, 1485 and 4347 nodes. In all nodal discretizations, two divisions are used in the z direction (thickness direction) while maintaining the element size. Therefore, the thickness of the beam (b) is changed to maintain an equal element size (or integration cell) in all three directions (Figure 33). Additionally, the varying thickness changes the moment of inertia of the cross section of the beam, thus changing the analytical solution according to the mesh used (equation(49)).

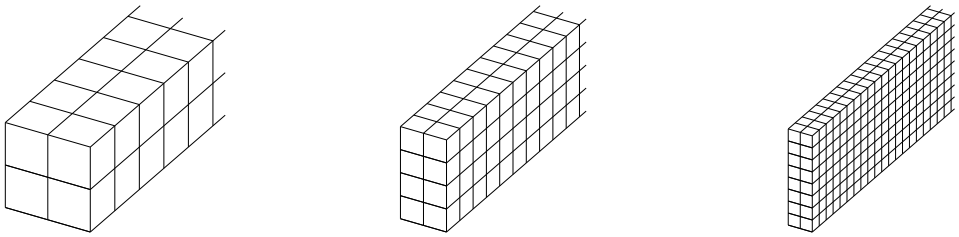

Figure 33 - Maintaining element size by varying beam thickness: (a) 369 nodes; (b) 1215 nodes; (c) 4347 nodes

The obtained displacements at point A considering the three-dimensional approach and respective relative errors are shown in Figure 34. Figure 35, Figure 36, Figure 37 and Figure 38 respectively display the normal stress distribution along the beam length ($y = h/2$ and $z = 0$) and height ($x = L/2$ and $z = 0$), and the shear stress distribution along the beam length ($y = 0$ and $z = 0$) and height ($x = L/2$ and $z = 0$). The problem is analysed using the FEM, RPIM and NNRPIM. However, the RPIM could not calculate proper solutions, due to the number of divisions along the thickness direction being too low (two divisions). So, only the FEM and NNRPIM are presented.

As in the two-dimensional analysis, the NNRPIM demonstrates to converge to the analytical solution at a higher rate than the FEM. In fact, the NNRPIM accurately calculates the displacement at point A when the coarser mesh is used. Contrarily, the FEM presents a considerable error if the 369 nodes mesh is used and converges to the analytical solution if the 4347 nodes mesh is used. Regarding the normal stress σ_{xx} and shear stress τ_{xy} distributions, the FEM and NNRPIM present similar solutions. As Figure 35, Figure 36, Figure 37 and Figure 38 demonstrates, the FEM and NNRPIM numerical solutions approach the analytical solution if denser meshes are used. When using the 4347 nodes mesh, the FEM and NNRPIM accurately predict the normal and shear stress distribution in the beam.

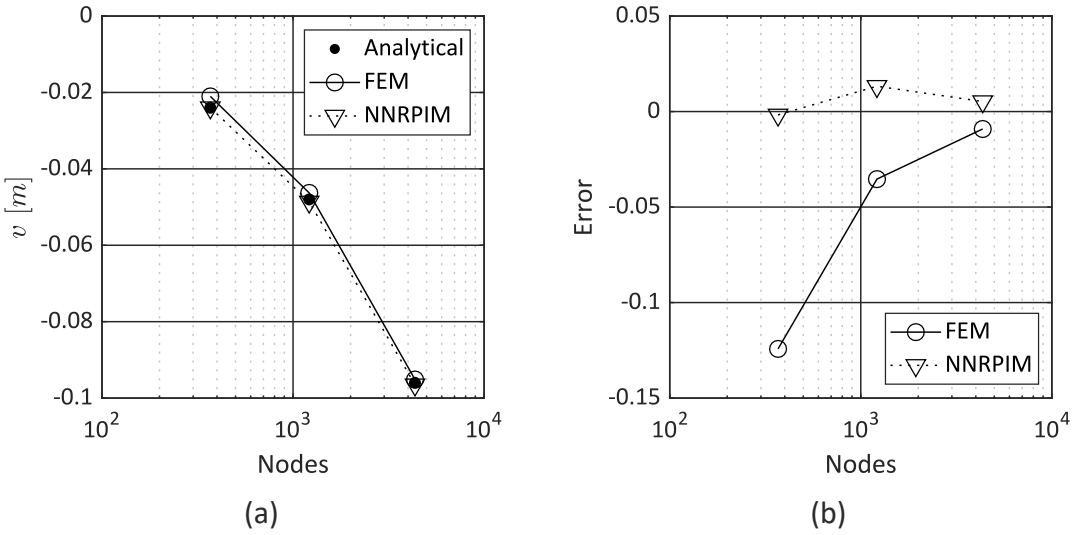

Figure 34 - (a) Displacement solutions at point A obtained with 369, 1215 and 4347 nodes; (b) Relative error

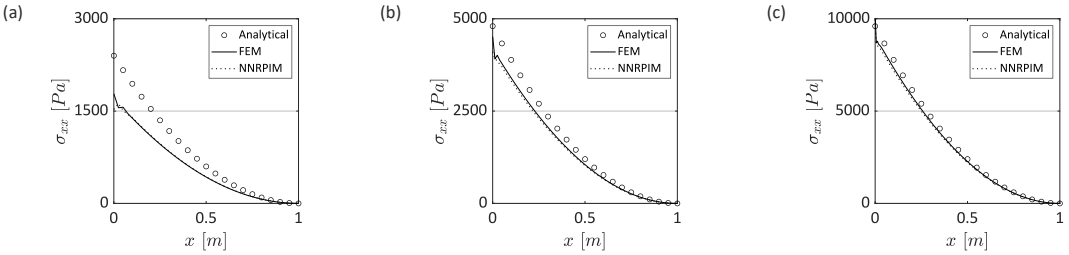

Figure 35 - Normal stress along y=z=0: (a) 369 nodes; (b) 1215 nodes; (c) 4347 nodes

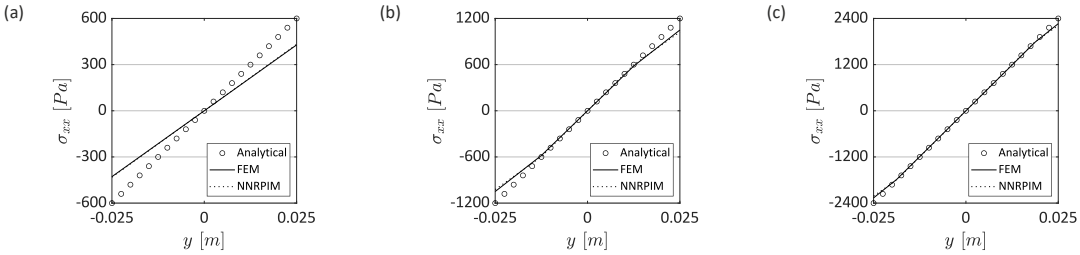

Figure 36 - Normal stress along x=L/2 and z=0: (a) 369 nodes; (b) 1215 nodes; (c) 4347 nodes

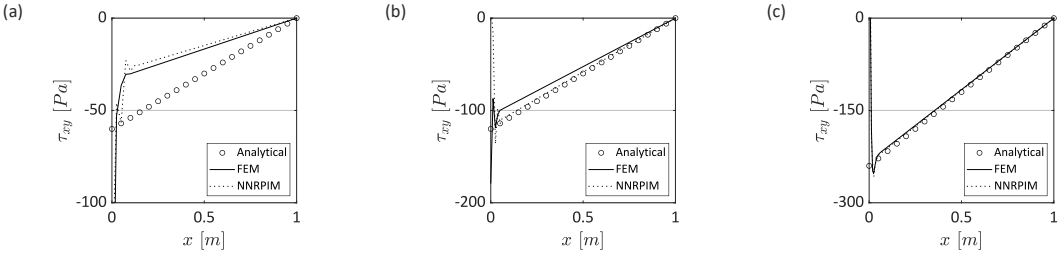

Figure 37 - Shear stress along y=z=0: (a) 369 nodes; (b) 1215 nodes; (c) 4347 nodes

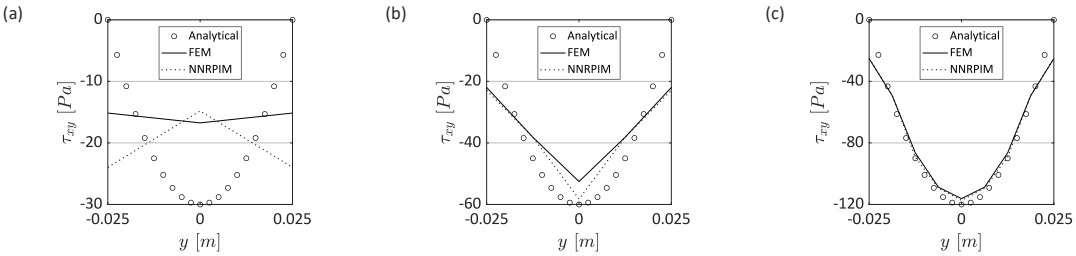

Figure 38 - Shear stress along x=L/2 and z=0: (a) 369 nodes; (b) 1215 nodes; (c) 4347 nodes

3.1.3 REMARKS

The cantilever submitted to a uniformly distributed load was analysed using the FEM, RPIM and NNRPIM. Considering the two-dimensional approach, the following conclusions are withdrawn:

i. FEM, RPIM and NNRPIM accurately predict displacement and stress fields;
ii. Considering maximum displacement, the NNRPIM converges at higher rate than the RPIM and FEM, which have similar rates of convergence;
iii. FEM, RPIM and NNRPIM have similar stress field solutions and approach the analytical distribution as the number of nodes increases;

Regarding the three-dimensional analysis, the following remarks are pointed out:

i. FEM and NNRPIM accurately predict displacement and stress fields;
ii. The NNRPIM calculates displacement solutions close to the analytical with all meshes used. Contrarily, the FEM converges to the exact solution as denser meshes are employed;
iii. RPIM failed to calculate accurate solutions, since it requires more than two divisions in the transversal direction.

3.2 STRUCTURAL OPTIMIZATION BENCHMARK EXAMPLES

In this section, an evolutionary structural optimization algorithm is applied to widely studied benchmark structural optimization examples. The selected optimization examples are the short cantilever and the loaded knee structure, also known as the “L” shaped bracket. Considering many literature works, the main objective of analysing these benchmark examples is to demonstrate the efficiency of the proposed algorithm in obtaining optimal topologies reported in the literature. The objectives of the several structural optimization analyses performed are the following:

i. Calibrate algorithm parameters considering the FEM, RPIM and NNRPIM;
ii. Investigate mesh influence in the optimal solutions;
iii. Evaluate the computational time of the structural optimization analysis;
iv. Demonstrate effectiveness of the method in obtaining optimal solutions reported in the literature.

The structural optimization benchmark examples are analysed using the FEM, RPIM and NNRPIM in the structural analysis phase, considering a linear static plane stress approach. In the FEM analysis, a classic FEM formulation is used considering four node quadrilateral elements. The formulation of the used RPI meshless methods is described in detail in section 2.1. Regarding the RPIM, sixteen nodes inside the influence domains are considered and a Gaussian integration is performed resorting to quadrilateral integration cells with 2×2 integration points. In the NNRPIM analysis, second-degree influence cells and a full integration are considered. Concerning the RPI shape functions in RPIM and NNRPIM, the following parameters are assumed: $c = 0{,}0001$, $p = 0{,}9999$ and constant polynomial basis.

3.2.1 SHORT CANTILEVER

The short cantilever under a point load at the middle of the free end (Figure 39a) is a benchmark optimization problem widely analysed in structural optimization. Figure 39 presents the cantilever optimal topology obtained in several literature works. The study developed on the cantilever example aims to evaluate the mesh and algorithm parameters influence in the algorithm solution and also to demonstrate that the optimization algorithm can produce the optimal solutions reported in the literature.

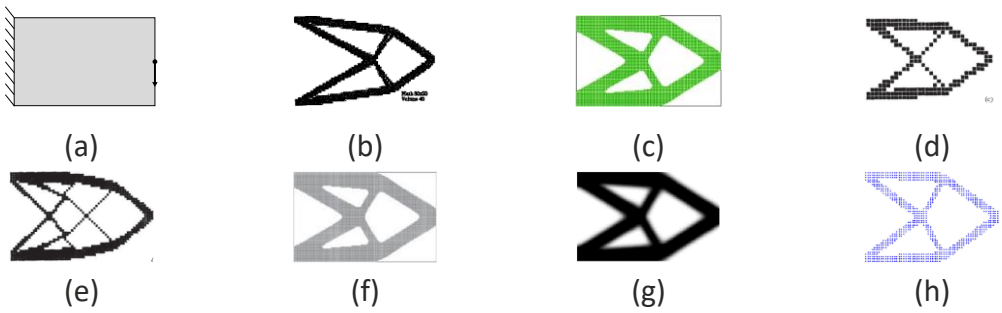

Figure 39 - Short cantilever literature solutions: (a) Short-cantilever structural optimization example; (b) [160]; (c) [161]; (d) [162]; (e) [162]; (f) [162]; (g) [162]; (h) [144]

The short cantilever problem analysed in this dissertation is presented in Figure 40a. The dimensions of the beam are $L = 1{,}6\,m$ and $h = 1\,m$, and a point load of $100\,N$ is applied at the middle of the free end. The material mechanical properties are $E = 1\,MPa$ and $\upsilon = 0{,}3$. To study the mesh density influence in the optimal solutions, the structural optimization analysis is performed considering a regular mesh of 693 nodes (Figure 40b), and a regular mesh of 2665 nodes (Figure 40c). To avoid stress concentrations or singularity, which may lead to inaccurate solutions, the point load of $100\,N$ is distributed over three nodes in the 693 nodes mesh, and over five nodes in the 2665 nodes mesh.

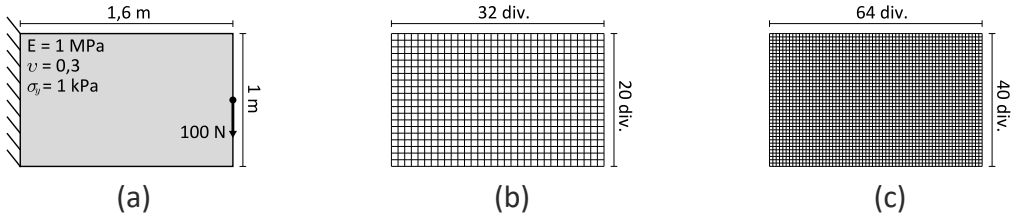

Figure 40 - Short cantilever structural optimization example: (a) Geometry, material and boundary conditions; (b) 693 nodes and 640 elements mesh; (c) 2665 nodes and 2560 elements mesh

The influence of the initial Decrease Ratio (DR) used in the optimization analysis is investigated. Structural optimization analyses are performed considering DR of 1%, 2%, 5% and 10%. Also, two distinct optimality criterions are assumed, VM effective stress and Strain Energy Density (SED). The density evolution on all structural optimization analyses combining the mentioned parameters are presented in Table 5, Table 6, Table 7 and Table 8, along with the iteration at each solution is reached and the respective volume fraction. The obtained solutions that achieve or approach the expected optimal solution (Figure 39) are highlighted. The topologies are selected based on characteristics as volume fraction, manufacturability, and aesthetics, and are the basis to posteriorly discuss the mesh influence, algorithm parameters and computational time.

Table 5 - Cantilever optimization solutions for 693 nodes mesh and VM criterion

DR	Method	Algorithm Solutions							
1%	FEM	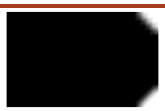	5	95,9%		10	92,4%		15	89,2%		20	86,9%
	RPIM		5	97,1%		15	93,6%		25	91,4%		33	91,4%
	NNRPIM		4	96,1%		8	92,6%		12	88,8%		16	86,6%
2%	FEM		3	95,2%		6	90,1%		9	87,5%		12	86,2%
	RPIM		10	90,2%		20	86,7%		28	80,3%		43	83,4%
	NNRPIM		24	69,4%		40	70,2%		92	60,1%		126	65,2%
5%	FEM	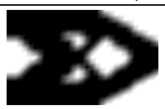	9	69,2%		**18**	**54,7%**	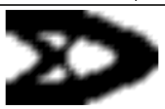	**30**	**62,1%**		**34**	**47,5%**
	RPIM		12	75,1%		30	70,2%		50	64,8%		78	67,6%
	NNRPIM		27	76,7%		31	62,8%		41	69,2%		50	58,0%
10%	FEM		4	72,8%		7	67,3%		8	59,1%		12	47,8%
	RPIM		5	73,9%		15	68,1%		24	50,6%		65	78,8%
	NNRPIM		**17**	**32,0%**		54	74,2%		**64**	**53,8%**		**65**	**71,5%**

Table 6 - Cantilever optimization solutions for 693 nodes mesh and SED criterion

DR	Method	Algorithm Solutions			
1%	FEM	 2 98,5%	 8 92,8%	 14 89,8%	 19 88,8%
	RPIM	 5 97,1%	 15 94,1%	 20 92,9%	 27 91,5%
	NNRPIM	 3 97,2%	 6 94,2%	 9 91,7%	 13 89,1%
2%	FEM	 3 95,2%	 6 89,8%	 9 87,5%	 12 86,9%
	RPIM	 10 91,2%	 15 89,7%	 23 85,2%	 36 80,8%
	NNRPIM	 20 74,9%	 43 73,4%	 **50 65,3%**	 **54 62,2%**
5%	FEM	 7 76,8%	 11 62,7%	 14 52,2%	 19 34,6%
	RPIM	 8 81,2%	 32 68,8%	 39 63,0%	 **47 53,0%**
	NNRPIM	 **17 56,6%**	 21 43,2%	 **24 30,8%**	 **45 46,7%**
10%	FEM	 8 71,6%	 25 64,0%	 **47 61,0%**	 **50 65,9%**
	RPIM	 7 68,3%	 38 43,4%	 45 60,9%	 104 63,6%
	NNRPIM	 5 83,1%	 13 71,9%	 22 46,1%	 **23 66,2%**

Table 7 - Cantilever optimization solutions for 2665 nodes mesh and VM criterion

DR	Method	Algorithm Solutions							
1%	FEM		28	83,1%		60	71,4%		66	68,4%		80	74,7%
	RPIM		50	81,4%		110	76,8%		133	75,6%		152	71,7%
	NNRPIM		30	78,8%		68	67,1%		95	78,4%		108	71,0%
2%	FEM		12	81,1%		20	71,2%		37	63,7%		79	29,3%
	RPIM		60	68,6%		**96**	**54,8%**		**128**	**48,3%**		174	57,5%
	NNRPIM		18	71,0%		**45**	**62,3%**		**54**	**72,4%**		**80**	**63,1%**
5%	FEM		8	69,8%		16	67,7%		**20**	**51,8%**		**24**	**34,7%**
	RPIM		14	71,7%		37	70,7%		46	47,4%		**47**	**44,6%**
	NNRPIM		14	66,5%		**26**	**59,0%**		28	64,1%		32	61,6%
10%	FEM		4	80,1%		7	69,1%		10	55,9%		14	45,3%
	RPIM		4	82,8%		8	74,9%		9	67,8%		**10**	**60,4%**
	NNRPIM		4	80,4%		7	51,2%		9	32,2%		**10**	**40,2%**

Table 8 - Cantilever optimization solutions for 2665 nodes mesh and SED criterion

DR	Method	Algorithm Solutions			
1%	FEM	 10 91,6%	 23 84,3%	 40 77,1%	 53 75,1%
	RPIM	 10 93,1%	 30 84,9%	 70 82,2%	 100 79,3%
	NNRPIM	 40 73,6%	 52 76,9%	 **90 56,8%**	 **103 51,8%**
2%	FEM	 50 35,0%	 51 49,6%	 **52 61,6%**	 **80 28,6%**
	RPIM	 30 77,2%	 70 65,1%	 120 63,3%	 150 59,8%
	NNRPIM	 **46 53,2%**	 **92 34,3%**	 **93 49,9%**	 115 49,7%
5%	FEM	 14 44,9%	 **17 61,9%**	 **24 43,6%**	 **28 58,4%**
	RPIM	 8 78,1%	 25 72,9%	 37 64,5%	 71 57,0%
	NNRPIM	 6 76,9%	 11 58,5%	 **20 45,1%**	 **33 56,3%**
10%	FEM	 2 89,5%	 4 70,6%	 **6 66,3%**	 11 47,9%
	RPIM	 3 81,7%	 5 68,0%	 8 48,6%	 **9 42,0%**
	NNRPIM	 4 70,5%	 11 74,9%	 19 44,1%	 **20 52,5%**

3.2.1.1 MESH INFLUENCE AND ALGORITHM PARAMETERS

A summary of the structural optimization analysis is presented in Table 9. The selected optimal topologies regarding the used numerical method and algorithm parameters are shown, except for the optimization analyses which did not achieve the optimal solution reported in the literature. In Table 9 it can be observed that several analyses did not achieve satisfactory solutions, whilst several other produced the optimal topology reported in the literature. Considering the number of optimal solutions in both nodal discretizations, using the 2665 nodes mesh results in a considerably higher number of solutions. Nonetheless, the 693 nodes mesh achieved remarkable solutions under specific parameters and numerical methods.

The structural optimization considering the 693 nodes mesh could not achieve proper results when assuming DR of 1% and 2% with neither the FEM, RPIM or NNRPIM. In these cases, the DR is too low and the algorithm cannot manage to evolve the initial structure towards an optimal solution, thus stopping the analysis at early iterations. The best results were obtained with DR of 5% and 10%. However, the optimality criterion affects the results when using the coarser mesh. When assuming a DR of 5%, optimal solutions were reached considering the VM criterion when using the FEM. Contrarily, the NNRPIM obtains the optimal topology with the SED criterion. Considering a DR of 10%, the reverse conclusions are achieved, but for the NNRPIM which approaches the optimal topology with both VM and SED criterions. Hence, sparser meshes can achieve optimal topologies, yet the algorithm parameters may be carefully selected, especially when using the FEM and RPIM.

The 2665 nodes mesh achieves the optimal topology within a wider range of parameters, as it can be noticed in Table 9. As in the 693 nodes mesh, no results were obtained when assuming a DR of 1%, except when the NNRPIM is combined with the SED criterion. Regarding the FEM and the NNRPIM, it can be concluded that the most beneficial solutions are obtained when assuming DR of 2% and 5%. Nonetheless, the NNRPIM achieves the optimal topology within a larger combination of parameters. Moreover, combining the NNRPIM with the SED criterion led to the optimal topology when using DR of 1%, 2%, 5% and 10%. Despite several analyses using a DR of 10% approach the topology reported in the literature, these solutions are rough and have some unexpected truss arrangements, meaning that high DR may result in coarser and less detailed solutions. Too much material is removed at each iteration, which can prevent the algorithm to reach a smooth optimal topology.

Table 9 - Selected cantilever optimal solutions

32x20 (693 nodes)					
		1%	2%	5%	10%
FEM	VM	-	-	 18 30 34	-
	SED	-	-	-	 47 50
RPIM	VM	-	-	-	-
	SED	-	-	 47	-
NNRPIM	VM	-	-	-	 17 64 65
	SED	-	 50 54 17 24 45		 23

64x40 (2665 nodes)					
		1%	2%	5%	10%
FEM	VM	-	-	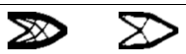 20 24	
	SED	-	 52 80 17 24 28		 6
RPIM	VM	-	 96 128	 47	 10
	SED	-	-	-	 9
NNRPIM	VM	-	 45 54 80	 26	 10
	SED	 90  103	 46 92 93 20 33		 20

3.2.1.2 COMPUTATIONAL TIME

In this section, the computational time of the structural optimization analyses is evaluated. In Figure 41 the curves relating the time and iterations in each analysis are presented. Additionally, the points at which the optimal solutions in Table 9 are obtained are highlighted. In a first stage it can be noticed that the mesh density highly influences the computational time per iteration. On the other hand, it is noticed that using the FEM, RPIM or NNRPIM does not significatively influence the computational time of the structural optimization analysis. Although when using the 2665 nodes mesh the computational time per iteration (line slope) can differ if the FEM, RPIM or NNRPIM is used, the time and iteration at which the optimal solutions are achieved is not significantly different. If the 693 mesh is used, the structural optimization computational time is relatively low and no differences in the computational time are observed when the FEM, RPIM or NNRPIM is used. Hence the mesh density is the critical parameter in

the computational time of the structural optimization analysis, and the numerical method used in the structural analysis phase does not significantly influences the computational time per iteration. Also, no relation is observed when the VM or SED criterion is used.

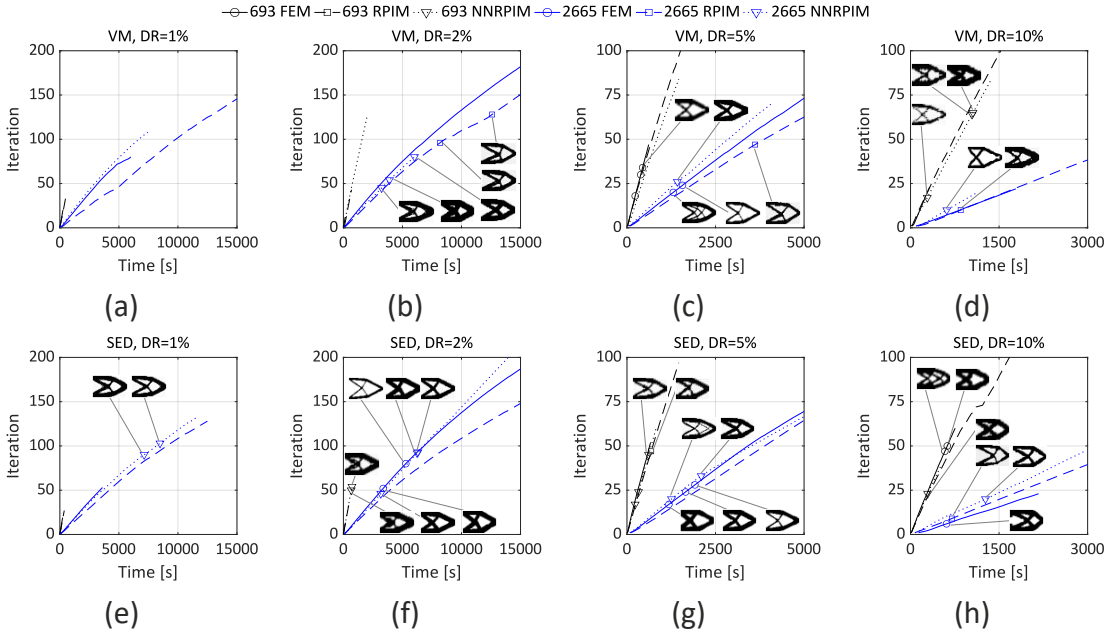

Figure 41 - Cantilever analyses computational time: (a) VM and DR=1%; (b) VM and DR=2%; (c) VM and DR=5%; (d) VM and DR=10%; (e) SED and DR=1%; (f) SED and DR=2%; (g) SED and DR=5%; (h) SED and DR=10%

Figure 42 intends to compare the computational time of the obtained optimal solutions (Table 9) regarding the DR assumed. Considering the 693 nodes mesh, the DR does not significantly influences the time at which the optimal topology is achieved. Since the computational time is relatively low, no patterns develop between the DR assumed and the computational time to achieve the optimal topology. Differently, when considering the 2665 nodes mesh, it is noticeable that the computational time needed to achieve the optimal solutions decreases as higher DR are employed. Even though using DR around 10% may approach the optimal topology at relatively low computational times, as it is referred previously, the obtained solutions assuming DR rounding 10% may be rougher and less reliable.

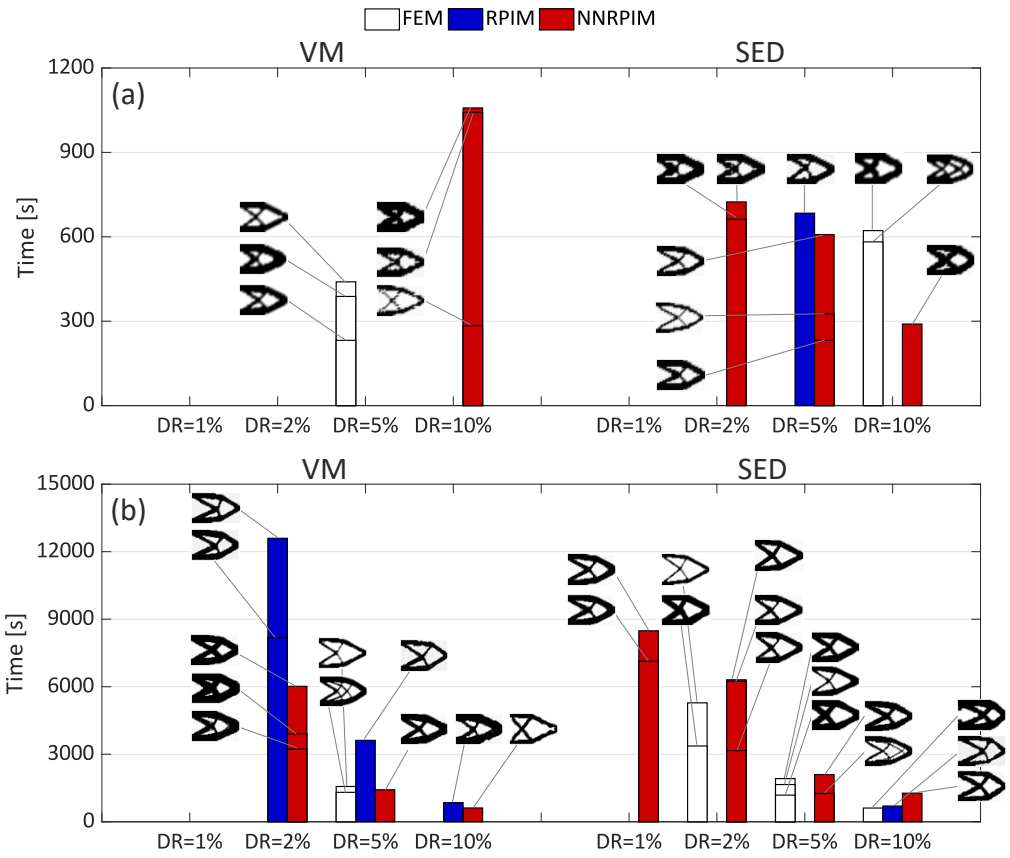

Figure 42 - Cantilever optimal solutions computational time: (a) 693 nodes mesh; (b) 2665 nodes mesh

A scatter map relating the computational time and iteration at which the optimal solutions in Table 9 are obtained is presented in Figure 43. Comparing the two distinct meshes used, Figure 43a illustrates the before mentioned fact that high DR (5% and 10%) produce better results when the 693 nodes mesh is used. Contrarily, when the 2665 nodes mesh is used low DR (1%, 2% and 5%) produce better results. Also, it is reinforced the fact that if lower DR are used, the computational time is considerably higher. Even though using the 2665 nodes mesh considering medium DR (5%) can result in the optimal topology at relatively low computational, assuming low DR (2%) may lead to more consistent solutions.

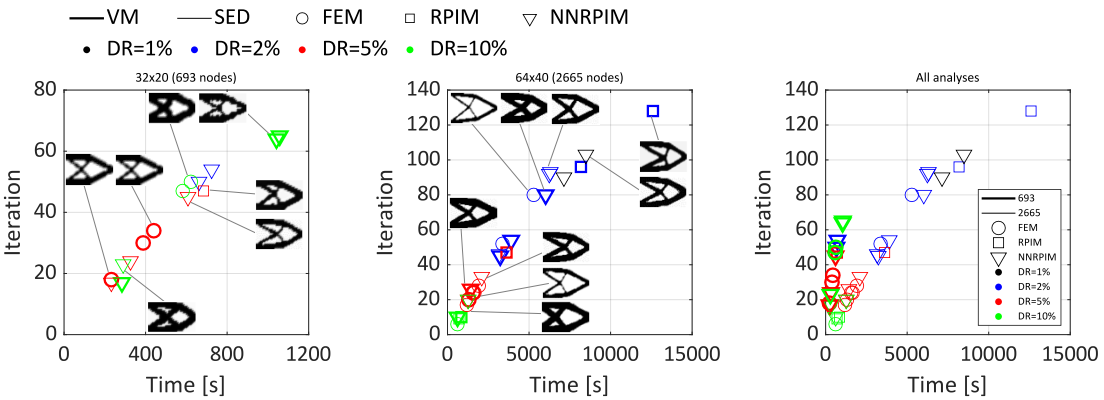

Figure 43 - Cantilever optimal solutions iteration and computational time: (a) 693nodes mesh; (b) 2665 nodes mesh; (c) All analyses

3.2.1.3 REMARKS

The short-cantilever structural optimization example was analysed considering two different meshes of 693 and 2665 nodes. Also, optimization analyses combining the VM stress and SED optimal criterion, and DR of 1%, 2%, 5% and 10% were performed. Regarding the studied algorithm parameters, mesh influence and computational time of the structural optimization analysis, the following conclusions are withdrawn:

i. DR of 5% and 10% achieve the optimal topology if the 693 nodes mesh is used. Differently, DR of 2% and 5% produce the best solutions when the 2665 nodes mesh is used;
ii. If the coarser mesh is used the optimal topology is achieved when considering a specific combination of parameters, while the more refined mesh achieves the optimal solution within a wide range of algorithm parameters and numerical methods;
iii. Using the FEM and NNRPIM consistently produce the optimal solution, while the RPIM showed to be more sensitive to the algorithm parameters;
iv. Optimality criterion has no influence in the computational time;
v. FEM, RPIM and NNRPIM have similar times per iteration when considering the same mesh density;
vi. The nodal density highly influences the computational time of the analysis;
vii. Concerning the 2665 nodes mesh, higher decrease ratios achieve the optimal solution at lower computational times, yet obtained solutions may be less detailed;

3.2.2 LOADED KNEE STRUCTURE ("L" SHAPED BRACKET)

As the short cantilever analysed in the previous section, the knee structure (Figure 44a) is also a widely analysed example in structural optimization. Several optimal topologies for the "L" shaped bracket reported in the literature are shown in Figure 44. The present structural optimization problem intends to further validate the proposed algorithm and numerical methods, as well as support the mesh and algorithm parameters calibration derived in the cantilever example.

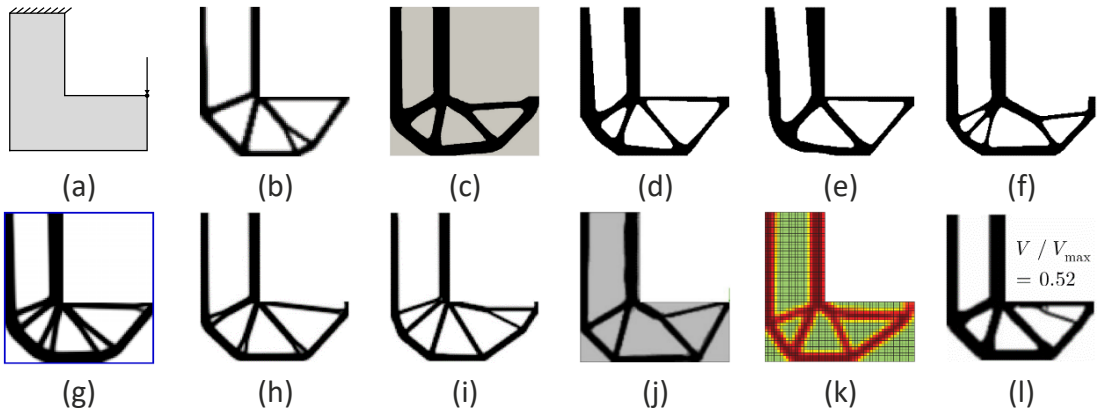

Figure 44 - Knee structure literature solutions: (a) "L" shaped bracket structural optimization example; (b) [163]; (c) [164]; (d) [165]; (e) [165]; (f) [165]; (g) [166]; (h) [167]; (i) [167]; (j) [168]; (k) [169]; (l) [170]

The geometry, dimensions and boundary conditions of the analysed "L" shaped bracket is presented in Figure 46a. The material mechanical properties assumed are $E = 1\ MPa$ and $\upsilon = 0{,}3$. To further investigate the mesh density influence, the structural optimization analysis of the knee structure is performed considering meshes of 1105, 2425 and 4257 nodes (Figure 46). As in the cantilever example, the point load is horizontally distributed over three nodes in the 1105 and 2425 nodes meshes, and over five nodes in the 4257 nodes mesh. The structural optimization analysis of the cantilever beam allowed to conclude that best optimization solutions were achieved with DR of 2% and 5%. Thus, the analysis of the knee structure is performed considering DR of 2% and 5%. Also, VM effective stress and SED criterions are used. The structural optimization results are presented in Table 10 to

Table 15. Regarding the optimization results and discussion, the same methodology adopted in the cantilever example is followed in the knee structure problem.

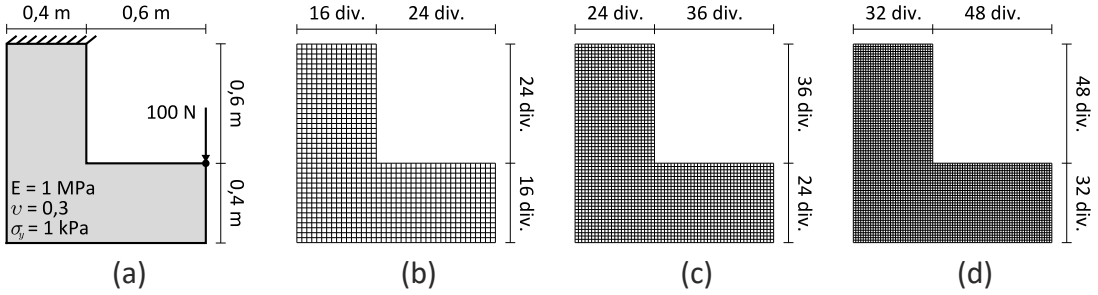

Figure 45 - "L" shaped bracket structural optimization example: (a) Geometry, material and boundary conditions; (b) 1105 nodes and 1024 elements mesh ; (c) 2425 nodes and 2304 elements mesh ; (d) 4257 nodes and 4096 elements mesh

3.2.2.1 MESH INFLUENCE AND ALGORITHM PARAMETERS

The obtained optimal topologies of the "L" bracket example are presented in Table 16. It can be noticed that the topology reported in the literature is achieved with the three meshes employed. A relative high number of optimal solutions is achieved in the structural optimization analyses with the three different meshes. These results support the conclusions withdraw from the cantilever example, since only the calibrated DR are considered in the present example. As in the cantilever example, the sparser mesh produces better results with DR=5%. Nevertheless, the NNRPIM achieves the optimal topology reported in the literature when combining the 1105 nodes mesh with DR of 2% or 5%. Although the optimal topology reported in the literature is achieved when the 1105, 2425 or 4257 nodes meshes is used, using the more refined mesh allows for more detailed and smooth solutions. If the 2425 or 4257 nodes mesh is used, optimal solutions are obtained with DR of 2% and 5% when the FEM, RPIM and NNRPIM are used in the structural analysis. When the more refined mesh is used, using the FEM and NNRPIM achieve better results if DR of 2% is used, whilst using DR of 5% produces the optimal topology when the RPIM is used. Supporting the results obtained in the cantilever example, a global analysis allows to conclude that DR of 5% achieves better results when relative coarse meshes is used, while DR of 2% allows for better results if more refined meshes are used.

Table 10 - "L" Bracket optimization solutions for 1105 nodes mesh and VM criterion

DR	Method	Algorithm Solutions			
2%	FEM	 9 92,4%	 18 84,0%	 27 74,4%	 36 66,7%
	RPIM	 20 96,8%	 46 89,2%	 86 81,8%	 154 72,4%
	NNRPIM	 10 90,4%	 30 68,2%	 **75 57,2%**	 **76 75,8%**
5%	FEM	 4 87,9%	 13 61,0%	 14 76,8%	 50 40,2%
	RPIM	 **29 61,1%**	 **31 75,5%**	 66 71,3%	 113 60,8%
	NNRPIM	 **16 61,6%**	 **21 44,5%**	 59 56,5%	 60 74,2%

Table 11 - "L" Bracket optimization solutions for 1105 nodes mesh and SED criterion

DR	Method	Algorithm Solutions			
2%	FEM	 5 95,7%	 9 91,3%	 14 85,5%	 18 83,9%
	RPIM	 5 98,0%	 9 98,0%	 14 97,3%	 18 96,8%
	NNRPIM	 49 51,4%	 50 71,5%	 **53 67,2%**	 76 66,6%
5%	FEM	 **15 51,5%**	 **16 69,8%**	 51 53,3%	 54 64,5%
	RPIM	 15 75,2%	 31 86,8%	 48 69,4%	 **67 67,1%**
	NNRPIM	 **15 71,5%**	 24 75,5%	 **34 38,7%**	 65 52,0%

Table 12 - "L" Bracket optimization solutions for 2425 nodes mesh and VM criterion

DR	Method	Algorithm Solutions			
2%	FEM	 41 62,9%	 46 70,0%	 **64 48,1%**	 180 50,2%
	RPIM	 105 64,6%	 **137 68,6%**	 157 68,6%	 276 64,5%
	NNRPIM	 56 52,8%	 **74 27,8%**	 **76 44,9%**	 **90 43,1%**
5%	FEM	 8 70,7%	 17 50,7%	 20 38,6%	 24 40,1%
	RPIM	 18 65,0%	 **29 61,3%**	 **42 55,2%**	 **44 50,2%**
	NNRPIM	 **12 54,5%**	 16 39,0%	 **19 47,1%**	 **92 46,8%**

Table 13 - "L" Bracket optimization solutions for 2425 nodes mesh and SED criterion

DR	Method	Algorithm Solutions			
2%	FEM	 **50 58,4%**	 71 65,3%	 **84 49,8%**	 **97 51,7%**
	RPIM	 67 78,4%	 98 73,6%	 **124 67,8%**	 171 68,1%
	NNRPIM	 **58 58,8%**	 **86 66,5%**	 **90 60,6%**	 269 61,5%
5%	FEM	 12 55,9%	 14 49,0%	 16 42,1%	 **17 57,2%**
	RPIM	 12 71,6%	 **42 63,4%**	 **102 71,3%**	 **157 73,3%**
	NNRPIM	 20 48,9%	 **26 61,5%**	 **30 62,2%**	 **66 67,2%**

Table 14 - "L" Bracket optimization solutions for 4257 nodes mesh and VM criterion

DR	Method	Algorithm Solutions			
2%	FEM				
		43 64,4%	**69 45,1%**	110 28,9%	**116 34,9%**
	RPIM				
		41 71,1%	69 71,6%	96 71,8%	120 68,9%
	NNRPIM				
		75 26,8%	**91 33,9%**	**107 23,0%**	108 36,9%
5%	FEM				
		4 85,9%	8 69,5%	10 60,9%	16 59,9%
	RPIM				
		25 64,0%	**35 41,2%**	**93 69,0%**	97 60,6%
	NNRPIM				
		8 69,1%	**12 66,6%**	**14 57,1%**	28 49,1%

Table 15 - "L" Bracket optimization solutions for 4257 nodes mesh and SED criterion

DR	Method	Algorithm Solutions			
2%	FEM				
		38 60,2%	44 52,9%	**45 64,4%**	**65 57,6%**
	RPIM				
		34 81,1%	75 77,1%	115 85,9%	132 80,3%
	NNRPIM				
		43 65,1%	58 55,8%	**86 39,1%**	92 61,2%
5%	FEM				
		10 62,5%	20 63,7%	30 45,7%	**31 55,5%**
	RPIM				
		20 74,3%	**50 71,7%**	**58 65,5%**	**92 63,4%**
	NNRPIM				
		9 64,8%	10 74,1%	**42 61,1%**	77 65,2%

Table 16 - Selected "L" shaped bracket optimal solutions

40x24x16 (1105 nodes)				
	2%		5%	
	VM	SED	VM	SED
FEM	-	-	-	 15 16
RPIM	-	-	 29 31	 67
NNRPIM	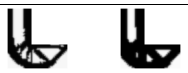 75 76	 53	 16 21 60	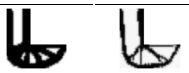 15 34
60x36x24 (2425 nodes)				
	2%		5%	
	VM	SED	VM	SED
FEM	 64	 50 84 97	-	 17
RPIM	 137	 124	 29 42 44	 42 102 157
NNRPIM	 74 76 90	 58 86 90	 12 19 92	 26 30 66
80x48x32 (4257 nodes)				
	2%		5%	
	VM	SED	VM	SED
FEM	 43 69 116	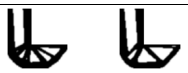 45 65	-	 31
RPIM	-	-	 25 35 93	 50 58 92
NNRPIM	 75 91 107	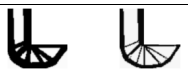 43 86	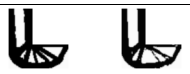 12 14	 42

3.2.2.2 COMPUTATIONAL TIME

As shown for the cantilever example, the mesh density highly influences the computational time per iteration (line slope). Regarding the "L" shaped bracket example, Figure 46 demonstrates the significant differences in the computational times considering the three different meshes employed. The 1105 nodes mesh is ten times faster than the 4257 nodes mesh, and three times faster than the 2425 nodes mesh. Therefore, the computational time per iteration may increase exponentially with the number of nodes used. Concerning the computational times of the FEM, RPIM and

NNRPIM, as it was concluded in the cantilever example, no pattern is observable in the computational time of the analysis using the different numerical methods.

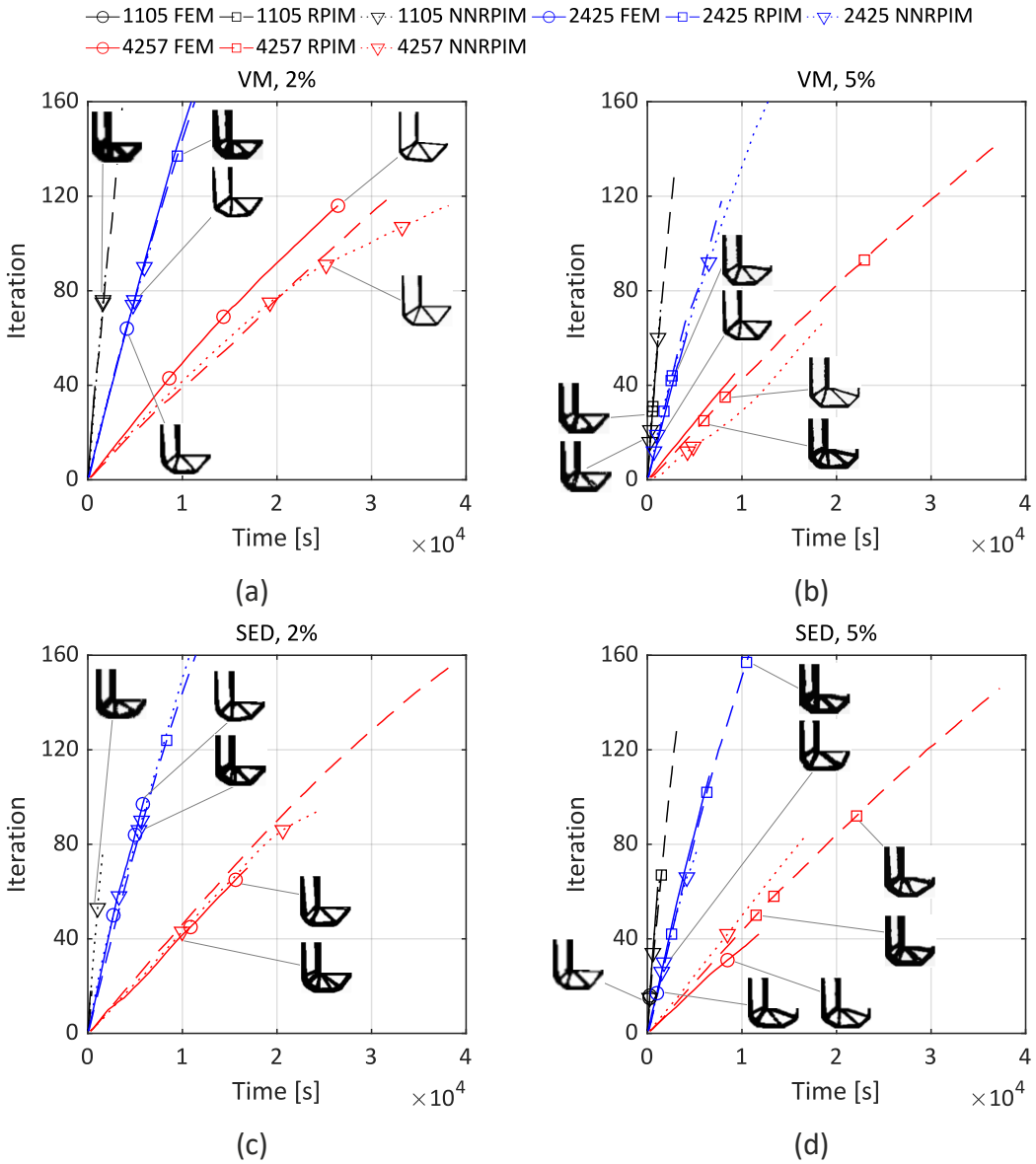

Figure 46 - Knee structure computational time: (a) VM criterion and DR=2%; (b) VM criterion and DR=5%; (c) SED criterion and DR=2%; (d) SED criterion and DR=5%;

In the cantilever example, a consistent pattern arises between the computational time at which the optimal topology is obtained, and the DR considered. It is observed that higher DR achieve the optimal topology at lower computational time. Regarding the "L" shaped bracket example, Figure 47 presents the obtained optimal topologies computational times regarding the considered DR. Since only DR of 2% and 5% are used in the present problem, the same pattern is less clear. Nonetheless, if DR of 5% is used, the optimal topology is generally obtained at lower computational times.

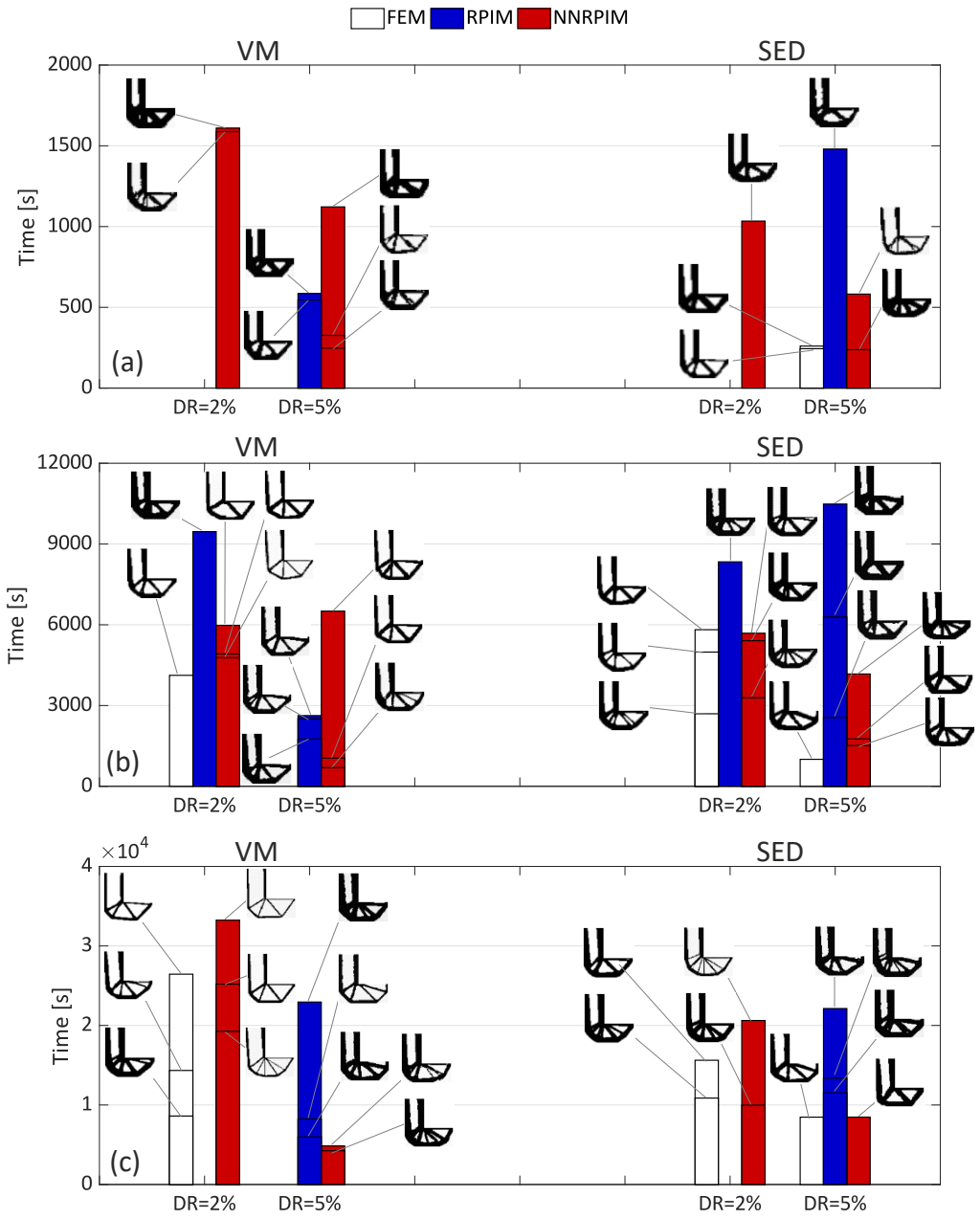

Figure 47 - Knee structure optimal solutions computational time: (a) 1105 nodes; (b) 2525 nodes; (c) 4257 nodes

3.2.2.3 REMARKS

The "L" shaped bracket problem is studied using the optimal DR calibrated in the cantilever example (2% and 5%). Additionally, the mesh influence is further evaluated by using three different meshes of 1105, 2425 and 4257 nodes. The structural optimization analyses combining the previous parameters allowed to take away the following conclusions:

i. Mesh density influences the optimal material distribution; More refined meshes allow to obtain more detailed and smooth solutions with reduced volume fractions;
ii. In all three meshes considered, assuming DR of 2% and 5% achieves the optimal topologies reported in the literature;

iii. Computational time per iteration significantly increases as denser meshes are used;
iv. Generally, using DR of 5% achieves optimal topologies at lower computational times than if DR of 2% is used;
v. The results of the knee structure example support and further validates the parameters calibrated in the cantilever example;

3.2.3 SUMMARY

In this section, a summary combining the cantilever and knee structure examples data is provided. A qualitative evaluation of the structural optimization study on the cantilever and knee structure problems is presented in Table 17. In the cantilever example, DR of 2% and 5% produced the best results, while no satisfactory solutions are obtained within the extreme DR assumed. So, DR of 2% and 5% are used in the knee structure problem. The second example supports the initial calibration in the cantilever exercise. As Table 17 illustrates, DR of 2% and 5% provide the best solutions both in quality and quantity. Regarding the mesh density influence, the green and yellow marks density is higher in the more refined meshes area. However, the computational time significantly increases if denser meshes is used.

Table 17 - Qualitative classification of structural optimization examples solutions

		DR=1%		DR=2%		DR=5%		DR=10%	
		VM	SED	VM	SED	VM	SED	VM	SED
Cantilever 693 nodes	FEM	🔴	🔴	🔴	🔴	🟢	🔴	🔴	🟡
	RPIM	🔴	🔴	🔴	🔴	🔴	🟡	🔴	🔴
	NNRPIM	🔴	🔴	🔴	🟡	🔴	🟢	🟡	🟡
"L" 1105 nodes	FEM	-	-	🔴	🔴	🔴	🟢	-	-
	RPIM	-	-	🔴	🔴	🟢	🟡	-	-
	NNRPIM	-	-	🟡	🟢	🟡	🟡	-	-
"L" 2425 nodes	FEM	-	-	🟢	🟢	🔴	🟡	-	-
	RPIM	-	-	🟡	🟡	🟢	🟡	-	-
	NNRPIM	-	-	🟢	🟡	🟢	🟢	-	-
Cantilever 2665 nodes	FEM	🔴	🔴	🔴	🟢	🟢	🟢	🔴	🟡
	RPIM	🔴	🔴	🟡	🔴	🟡	🔴	🟡	🟡
	NNRPIM	🔴	🟢	🟢	🟢	🟢	🟢	🟡	🟡
"L" 4257 nodes	FEM	-	-	🟢	🟢	🔴	🟡	-	-
	RPIM	-	-	🔴	🔴	🟡	🟢	-	-
	NNRPIM	-	-	🟢	🟡	🟡	🟡	-	-

🟢 Optimal topology 🟡 Approaches optimal topology 🔴 No satisfactory solution

In Table 18, the best topologies obtained in both examples are presented. Summing up, the proposed structural optimization algorithm successfully calculates the optimal topology of the cantilever and the knee structure examples reported in the literature. The optimal topology is achieved with the FEM, RPIM and NNRPIM. However, the best solutions with each numerical method may be achieved when combining various algorithm parameters (DR and optimality criterion).

Table 18 - Cantilever and "L" shaped bracket optimal solutions

	Cant. 693	“L” 1105	“L” 2425	Cant. 2665	“L” 4257
FEM					
	VM DR=5% It. 35 47,5%	SED DR=5% It. 15 51,5%	SED DR=2% It. 97 51,7%	SED DR=2% It. 80 28,6%	VM DR=2% It. 116 34,9%
RPIM					
	SED DR=5% It. 47 53,0%	VM DR=5% It. 29 61,1%	VM DR=5% It. 44 50,2%	VM DR=2% It. 128 48,3%	SED DR=5% It. 92 63,4%
NNRPIM	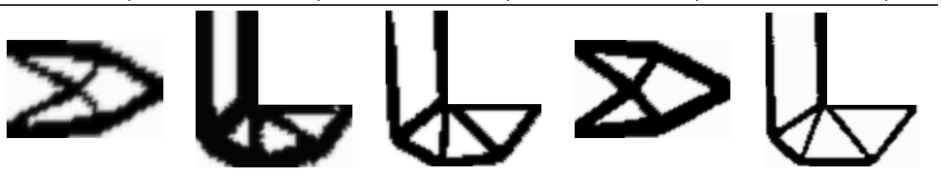				
	SED DR=5% It. 45 46,7%	SED DR=2% It. 53 67,2%	VM DR=2% It. 76 44,9%	SED DR=2% It. 93 49,9%	VM DR=2% It. 91 33,9%

In both the cantilever and the “L” shaped bracket examples, the influence of the mesh density on the computational time of the structural optimization analysis is studied. Combining data from both problems, the influence of the mesh density in the computational time per iteration is presented in Figure 48. The computational time per iteration plotted in Figure 48a represents the mean of all structural optimization analyses. In Figure 48b, the computational time per iteration is presented regarding if the FEM, RPIM or NNRPIM is used in the structural analysis phase. While the computational time significantly increases with the number of nodes used, no clear patter arises between the computational time per iteration and the numerical method used in the structural analysis.

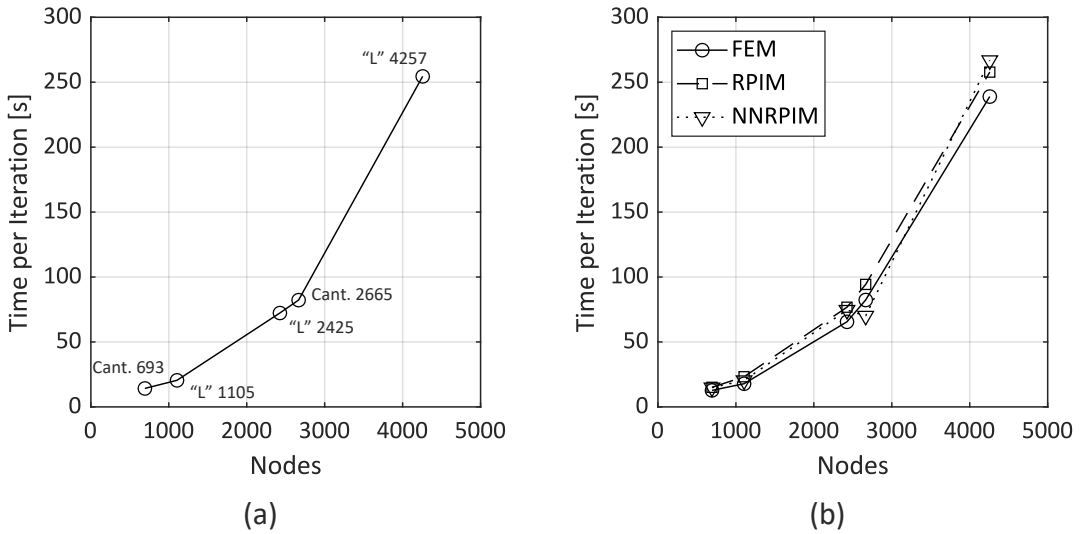

Figure 48 - Nodal density influence in computational time

3.3 INDUSTRIAL STRUCTURAL OPTIMATION APPLICATIONS

The structural optimization algorithm is applied to several industrial applications using the FEM, RPIM and NNRPIM. An automotive wheel rim, pedal and an aircraft wing rib are optimized, considering plane stress conditions. Regarding the numerical methods employed, the same parameters assumed in the benchmark examples are considered. On the other hand, the structural optimization algorithm parameters considered are DR of 2% and VM stress criterion, which verified to produce consistent solutions within the benchmark problems. The structural optimization implementation methodology followed in this section is presented in Figure 49. Initially, the original structure geometry is designed in Solidworks 2019. Then, the nodal meshes are created in FEMAP and imported to FEMAS, where the numerical analysis are performed. Based on the algorithm solutions, an optimized structure is designed and the models are numerically analysed. Regarding the linear static analyses, the optimized models are discretized in roughly the same number of nodes as the original models, and the NNRPIM is used. Finally, several changes to the optimized model can be made to further increase performance.

Figure 49 - Structural optimization implementation procedure

3.3.1 AUTOMOTIVE WHEEL RIM

Automotive parts represent a wide range of applications where structural optimization can be implemented to design cost and energy efficient components. In this section, the design of an automotive wheel rim is developed through structural optimization. The analysed model is presented in Figure 50, whose dimensions are common size dimensions. Boundary regions are set to non-design regions to preserve the original shape of the rim. The wheel rim model is discretized in 3960 nodes and 7680 three node elements, and common aluminium elastic material properties are considered: $E = 70\ GPa$ and $\upsilon = 0{,}33$.

Figure 50 - (a) Wheel rim design model; (b) Wheel rim dimensions (mm)

The essential and natural boundary conditions introduced in the wheel rim are shown in Figure 51. Tire pressure is not considered. Rather, two point-load forces are considered: normal reaction force and friction force. By considering the friction force as

$\mu \cdot N$, being μ the static coefficient of friction and N the normal reaction force, it is assumed the wheel is on the verge of slipping.

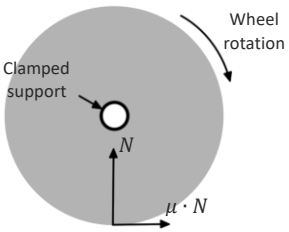

Figure 51 - Wheel rim boundary conditions

Considering a regular $1000\ kg$ mass car, the normal reaction force is calculated by the following expression:

$$N = \frac{W}{4} = \frac{1000\ kg \cdot g}{4} = \frac{1000\ kg \cdot 9{,}8\ m/s^2}{4} = 2450\ N \tag{51}$$

Regarding the friction force, the static coefficient of friction varies according with tire and ground materials, and weather conditions. Since the assumed value may affect the algorithm solutions, an average value considering tire rubber and common asphalt of 0,7 is considered. Following the described approach, the algorithm redistributes the material in the applied force region. The obtained topology can then be reproduced around the centre axis. The optimization algorithm solutions are presented in Table 19.

Table 19 - Wheel rim structural optimization results

FEM		RPIM		NNRPIM	
					
96	7,26 h	15	1,30 h	65	2,80 h
					
101	7,64 h	25	2,13 h	73	3,22 h
					
112	8,49 h	31	2,61 h	74	3,26 h
					
124	9,41 h	38	3,19 h	79	3,51 h

3.3.1.1 OPTIMAL TOPOLOGY DESIGN AND STRUCTURAL ANALYSIS

Since a single point load is applied at the base of the wheel, the algorithm produces a topology focused on that region of the wheel, as can be observed in Table 19. Based on the algorithm solutions, several models can be designed by reproducing the resulting topology a certain number of times. In this work, two models were designed by reproducing the algorithm solution six (Figure 52a), and eight times (Figure 52b).

(a) (b)

Figure 52 - (a) Optimized rim model 1; (b) Optimized rim model 2

Unlike in the original continuous domain, two load cases may be considered in the optimized structures. Due to the empty spaces in the model, the displacement at the ground contact point is not constant as the wheel roles. Therefore, the load cases presented in Figure 53 are studied in the structural analysis.

(a) (b)

Figure 53 - (a) Load case 1; (b) Load case 2

The structural analysis results are presented in Table 20. Figure 54 and Table 21 show the displacement and stress fields on the original and optimized models, respectively. The structure stiffness is calculated by dividing the total force over the displacement at the ground contact point. The initial continuous model has a $1237\ cm^2$ surface area. The new developed designs (models 1 and 2) have surface areas of $699{,}9\ cm^2$ (model 1) and $757{,}3\ cm^2$ (model 2), resulting in volume reductions of 43,4% and 38,8%, respectively. Since for model 2 the optimal structure is reproduced 8 times, the model 2 occupies a larger volume. On the other hand, it shows a lower distance between local structures, which reduces displacement if load case two is considered.

As can be noticed in Table 20, load case two is the most severe case. Since less material is present in the load region, displacement and stress are considerably higher in load case two. Comparing the two developed designs, model 2 allow for lower displacement

and stress. On the other hand, model 1 achieves a lower volume fraction. Nonetheless, displacements are of low magnitude and induced stresses are significantly below material yield stress.

Even though displacements are higher in the new optimized structures, considerably low volume fractions were achieved. In practical industrial applications, if displacements are within specified constraints, significant weight saving can be achieved through implementation of structural optimization in design phase. Considering the present application, after obtaining a local algorithm solution, several designs can be tested. By varying the number of reproductions, as well as part thickness, several models can be designed accordingly with volume objectives and displacement constraints. This structural optimization application demonstrates that innovative designs can be developed based on structural optimization algorithms, since these automatically design a new optimized topology from an initial continuous solid domain.

Table 20 - Structural analysis results in original and optimized rim structures

	Original structure	6 Reproductions structure		8 Reproductions structure	
		LC 1	LC 2	LC 1	LC 2
V_f	100%	56,6% (-43,4%)		61,2% (-38,8%)	
$\|u\|\ [m]$	4,18E-07	7,57E-07 (+81,3%)	1,15E-06 (+176%)	7,32E-07 (+75,3%)	8,74E-07 (+109%)
$K\ [N/m]$	7,16E+09	3,95E+09 (-44,8%)	2,60E+09 (-63,7%)	4,08E+09 (-43,0%)	3,42E+09 (-52,2%)
$K/V_f\ [N/m]$	7,16E+09	6,98E+09 (-2,50%)	4,59E+09 (-35,9%)	6,67E+09 (-6,82%)	5,59E+09 (-21,9%)
${\sigma_{VM}}^{max}$	2,29E+05	3,31E+05 (+44,4%)	5,20E+05 (+127%)	3,22E+05 (+40,6%)	4,39E+05 (91,4%)

(a) (b)

Figure 54 - (a) Original rim model total displacement field; (b) Original rim model VM stress field

Table 21 - Total displacement and VM stress fields of optimized rim structures

6 Reproductions structure		8 Reproductions structure	
LC 1	LC 2	LC 1	LC 2
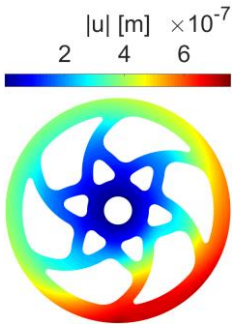	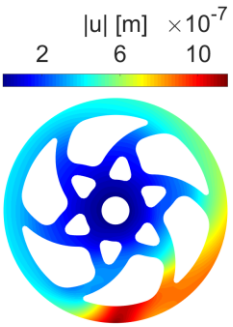	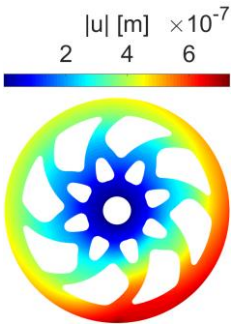	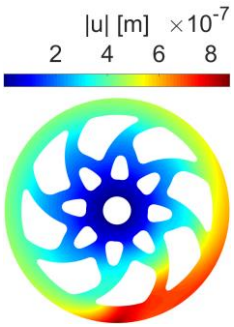
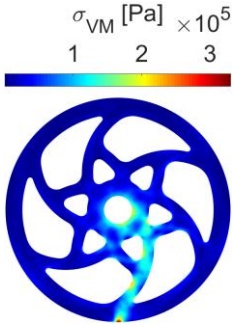	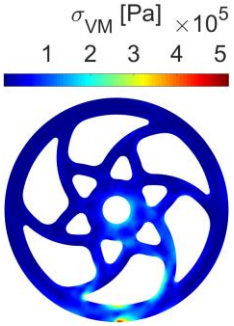	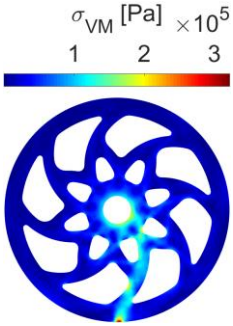	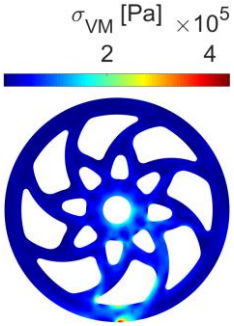

3.3.2 AUTOMOTIVE BRAKE PEDAL

Today, automotive brake pedals are primarily produced through conventional manufacturing processes. Although several new generation materials as composite and lightweight plastic materials have been tested in automotive pedals, structural optimization is a growing technique capable of achieving lightweight pedal designs to produce through additive manufacturing. Several authors have implemented structural optimization algorithms to reduce the mass of brake pedals [156], [171], [172]. In this dissertation, a general two-dimensional brake pedal is designed (Figure 55) and posteriorly optimized. The region around supports must be set as “not-remodelled” material (i.e., this material cannot be optimized) to preserve the material in that regions until the end of the analysis. Additionally, the contour of the pedal is also set as “not-remodelled” domain to preserve the initial pedal shape, thus forcing the algorithm to remodel and optimize the interior of the structure.

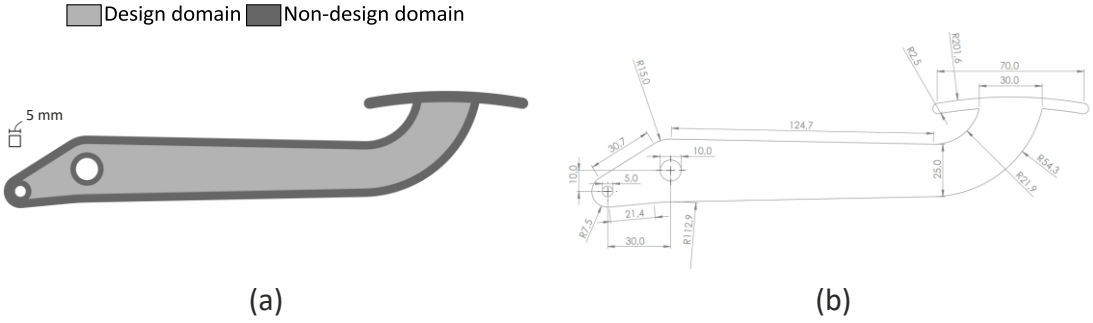

(a) (b)

Figure 55 - (a) General pedal design model; (b) Pedal dimensions (mm)

The designed model is discretized in 3920 nodes and 7374 three nodes elements, and common steel elastic material properties are considered: $E = 210\ GPa$ and $\upsilon = 0{,}3$. Regarding the boundary conditions, different load cases considering the initial and final position of the brake pedal, as well as different foot positions are considered. Considering the initial and final positions of the pedal, and by assuming that the force applied by the foot remains in the same direction, different load cases may be considered by varying the angle at which the force is applied on the foot pad. The different load cases considered are shown in Figure 56b. Each load case has the same weight (25%). In all load cases the support holes are clamped. The pedal structural optimization results are presented in Table 22.

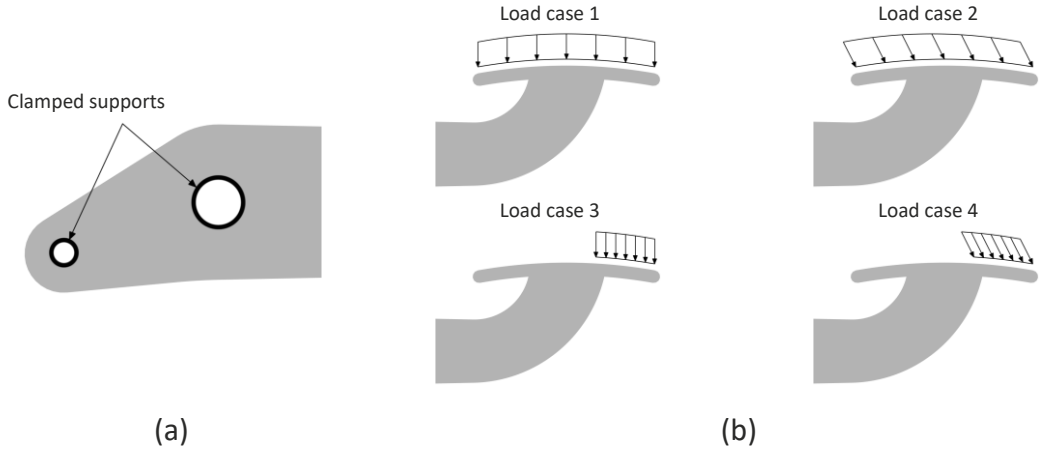

Figure 56 - Automotive pedal boundary conditions: (a) Essential boundary on all load cases; (b) Natural boundary for each load case

Table 22 - Pedal structural optimization results

FEM		RPIM		NNRPIM	
				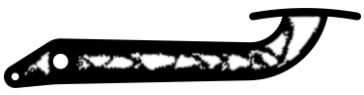	
44	6,78 h	25	4,27 h	30	3,82 h
				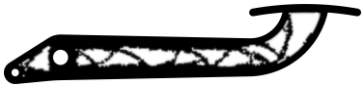	
50	7,74 h	40	6,83 h	34	4,33 h
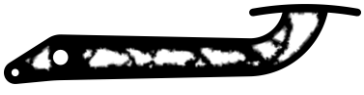				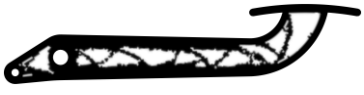	
54	8,39 h	47	8,07 h	38	4,85 h
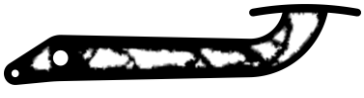					
60	9,36 h	49	8,45 h	60	7,82 h

3.3.2.1 OPTIMAL TOPOLOGY DESIGN AND STRUCTURAL ANALYSIS

Based on the obtained algorithm solutions presented in Table 22, an optimized topology was designed. Then, based on the structural analysis results of the original and redesigned models, the initial redesigned model is further optimized by changing beam thickness in order to improve general mechanical performance and stiffness to weight ratio.

3.3.2.1.1 INITIAL OPTIMIZED DESIGN

The initially optimized model shown in Figure 57 was designed with constant beam thickness, focusing primarily on volume reduction. Whilst the original model has a surface area of $5862\,mm^2$, the optimized model has $3081\,mm^2$ of surface area, achieving a material reduction of 47,4%. After a linear static analysis of the original and optimized models, both structures are characterized in terms of total displacement at the middle of the foot pad, and maximum VM effective stress. As material is removed from the original structure, it is expected the displacement of the optimized structure to be higher. Nonetheless, the reduction in volume must significantly compensate the loss in stiffness. Since structural components are primarily characterized by structure stiffness, the optimality of the structure is evaluated by its stiffness to weigh ratio. The pedal stiffness is calculated by dividing the $1000\,N$ force over the displacement at the middle of the foot pad.

(a) (b)

Figure 57 - (a) Original pedal model; (b) Optimized pedal model

The structural analysis results for the original and optimized structures are presented in Table 23. Total displacement and VM stress distribution plots are shown in Table 24. As expected, the displacement of the optimized model is significantly higher in four load cases, resulting in a stiffness reduction of 42,6% (average of all load cases). Being the volume reduction higher than the loss in structure stiffness, the optimal design has a superior stiffness to weight ratio (+9,23%). Regarding the VM stress fields induced in optimized structure, one can observe in Table 24 that greater stresses occur at the contour beams of the pedal. Although the maximum VM stress is significantly lower than the material yield stress, the optimized structure can be redesigned to smoothly distribute stress in those regions, which may also positively affect the stiffness and stiffness to weigh ratio of the pedal structure. In the following section, the initial optimized model is redesigned by varying beam thickness accordingly with the described issues to further optimize the pedal structure.

Table 23 - Structural analysis results in original and optimized pedal structure

	Original structure		Optimized structure	
V_f	100%		52,6% (-47,4%)	
$\|u\|\ [m]$	LC 1	LC 2	LC 1	LC 2
	4,40E-06	4,53E-06	7,62E-06 (+73,2%)	7,94E-06 (+75,3%)
	LC 3	LC 4	LC 3	LC 4
	5,39E-06	5,38E-06	9,35E-06 (+73,3%)	9,42E-06 (+75,0%)
$K\ [N/m]$	LC 1	LC 2	LC 1	LC 2
	2,27E+08	2,21E+08	1,31E+08 (-42,3%)	1,26E+08 (-43,0%)
	LC 3	LC 4	LC 3	LC 4
	1,85E+08	1,86E+08	1,07E+08 (-42,3%)	1,06E+08 (-42,9%)
$K/V_f\ [N/m]$	LC 1	LC 2	LC 1	LC 2
	2,27E+08	2,21E+08	2,5E+08 (+9,86%)	2,4E+08 (+8,52%)
	LC 3	LC 4	LC 3	LC 4
	1,85E+08	1,86E+08	2,04E+08 (+9,81%)	2,02E+08 (+8,73%)
${\sigma_{VM}}^{max}\ [Pa]$	LC 1	LC 2	LC 1	LC 2
	1,54E+06	1,53E+06	2,13E+06 (+38,4%)	2,01E+06 (+31,2%)
	LC 3	LC 4	LC 3	LC 4
	2,38E+06	2,14E+06	2,79E+06 (+17,4%)	2,44E+06 (+14,2%)

Table 24 - Displacement and VM stress fields of original and optimized pedal structures

Original structure		Optimized structure	
LC 1	LC 2	LC 1	LC 2
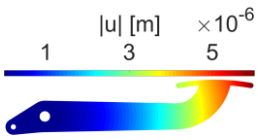	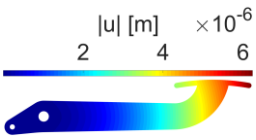	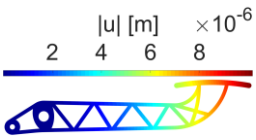	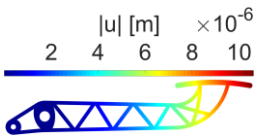
LC 3	LC 4	LC 3	LC 4
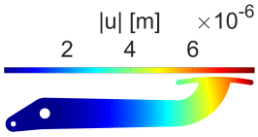	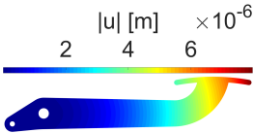	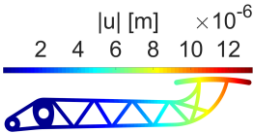	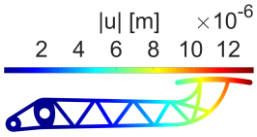
LC 1	LC 2	LC 1	LC 2
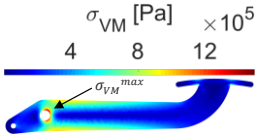	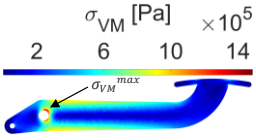	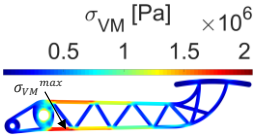	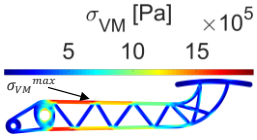
LC 3	LC 4	LC 3	LC 4
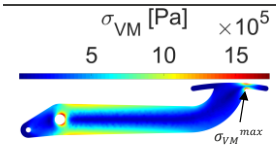	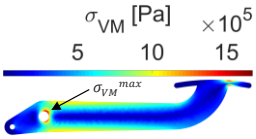	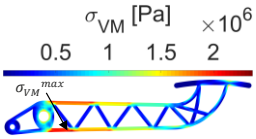	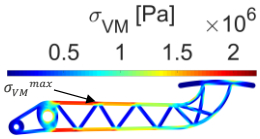

3.3.2.1.2 SIZE OPTIMIZATION

In the previous section, it was observed that the initial optimized model could be further optimized by varying beam thickness, specifically in the contour parts of the pedal where higher stresses occur. Therefore, the model presented in Figure 58c was designed. The outward beams thickness is increased, whilst the interior beams thickness was reduced. The resulting model has a surface area of $3750\,mm^2$, corresponding to a weight reduction of 36% comparing to the original structure (Figure 58a).

(a) (b) (c)

Figure 58 - (a) Original pedal model; (b) Initial optimized pedal model; (c) Optimized pedal model after size optimization

In Table 25, the structural analysis results of all three designed models (original structure, optimized structure 1 and optimized structure 2) are presented for comparison. Although optimized structure 2 achieves a lower volume reduction, the displacement is significantly reduced when compared with optimized structure 1. The displacement reduction from structure 1 to structure 2 results in a stiffness increase and, more relevant, in a significant increase in the stiffness to weight ratio to +25,2% of the original pedal structure. Additionally, the maximum VM stress is reduced to values

closer to those of the original structure. It can also be seen in Table 26 that the maximum stress region was moved out from the outward parts of the structure and the VM stress field is smoother in the optimized structure 2. This application demonstrates that structural optimization is a viable technique to design optimal topologies and reduce weight of existing structures. Moreover, the implementation of standard engineering procedures can further increase the structure mechanical performance while still considerably reducing volume.

Table 25 - Structural analysis results in original and optimized pedal structures

	Original structure		Optimized structure 1		Optimized structure 2	
V_f	100%		52,6% (-47,4%)		64,0% (-36,0%)	
$\|u\|\ [m]$	LC 1	LC 2	LC 1	LC 2	LC 1	LC 2
	4,40E-06	4,53E-06	7,62E-06 (+73,2%)	7,94E-06 (+75,3%)	5,42E-06 (+23,1%)	5,71E-06 (+26,0%)
	LC 3	LC 4	LC 3	LC 4	LC 3	LC 4
	5,39E-06	5,38E-06	9,35E-06 (+73,3%)	9,42E-06 (+75,0%)	6,69E-06 (+24,1%)	6,8E-06 (+26,4%)
$K\ [N/m]$	LC 1	LC 2	LC 1	LC 2	LC 1	LC 2
	2,27E+08	2,21E+08	1,31E+08 (-42,3%)	1,26E+08 (-43,0%)	1,85E+08 (-18,8%)	1,75E+08 (-20,7%)
	LC 3	LC 4	LC 3	LC 4	LC 3	LC 4
	1,85E+08	1,86E+08	1,07E+08 (-42,3%)	1,06E+08 (-42,9%)	1,49E+08 (-19,4%)	1,47E+08 (-20,9%)
$K/V_f\ [N/m]$	LC 1	LC 2	LC 1	LC 2	LC 1	LC 2
	2,27E+08	2,21E+08	2,5E+08 (+9,86%)	2,4E+08 (+8,52%)	2,89E+08 (+27,0%)	2,74E+08 (+24,0%)
	LC 3	LC 4	LC 3	LC 4	LC 3	LC 4
	1,85E+08	1,86E+08	2,04E+08 (+9,81%)	2,02E+08 (+8,73%)	2,34E+08 (+26,0%)	2,3E+08 (+23,7%)
${\sigma_{VM}}^{max}\ [Pa]$	LC 1	LC 2	LC 1	LC 2	LC 1	LC 2
	1,54E+06	1,53E+06	2,13E+06 (+38,4%)	2,01E+06 (+31,2%)	1,59E+06 (+3,03%)	1,56E+06 (+2,23%)
	LC 3	LC 4	LC 3	LC 4	LC 3	LC 4
	2,38E+06	2,14E+06	2,79E+06 (+17,4%)	2,44E+06 (+14,2%)	2,47E+06 (+3,90%)	2,39E+06 (+11,9%)

Table 26 - Displacement and VM stress fields of optimized pedal structure 2

LC 1	LC 2	LC 3	LC 4
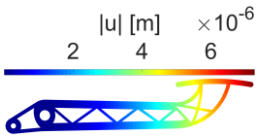	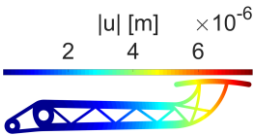	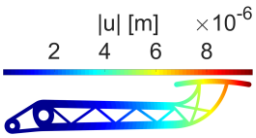	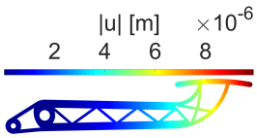
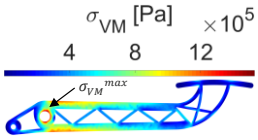	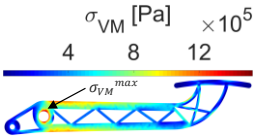	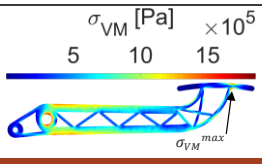	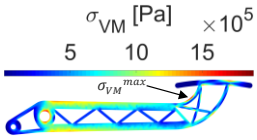

3.3.3 AIRCRAFT WING RIB

Aircraft industry continuously investigates new techniques to design components with reduced weight and increased performance. In recent years, topology optimization is being introduced to aircraft industry as a profitable tool in the product design phase. Wing ribs (Figure 59a) are components where significant weight reductions can be achieved. Several works implementing topology optimization in the design of aircraft wing ribs can be found in the literature [173]–[176]. In this dissertation, a common aircraft wing rib design (Figure 59b) is optimized by means of structural optimization. The structural optimization analysis is based on the model presented in Figure 59c. The whole interior is design domain, and the contour of the structure is set as "not-remodelled" material to preserve the exterior shape of the rib.

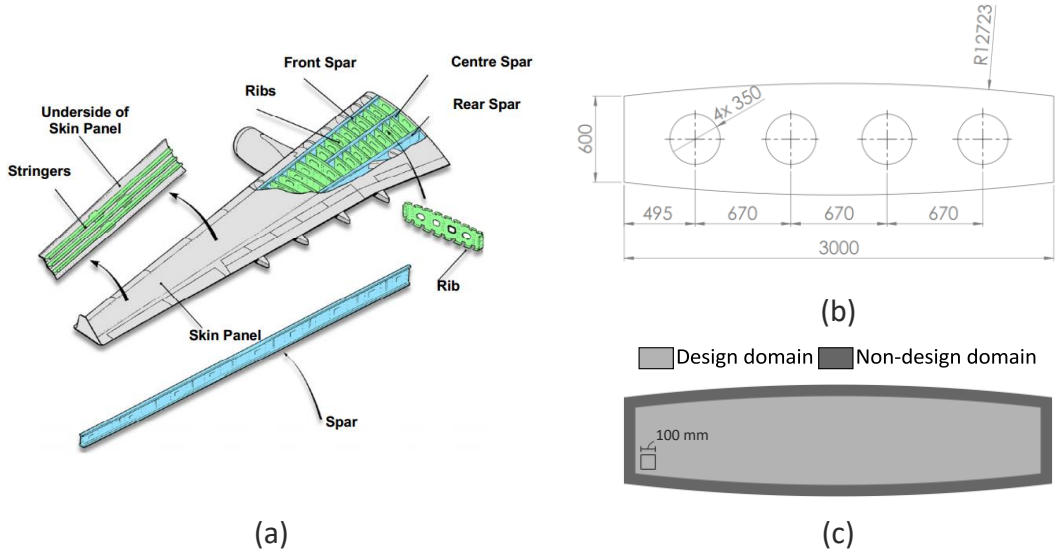

Figure 59 -(a) Aircraft wing components (image from [174]); (b) Conventional rib model dimensions (mm); (c) Initial design model

The model is discretized in 3844 nodes and 7372 three nodes elements. Regarding the material properties, aluminium elastic properties are considered: $E = 70\ GPa$ and $\upsilon = 0{,}33$. Aircraft components are subjected to highly complex loads. The loads applied in this work are based on the loads considered in [176], in which similar wing rib designs are developed. Figure 60 presents the boundary conditions enforced on the wing rib. The wing rib structural optimization results are presented in Table 27.

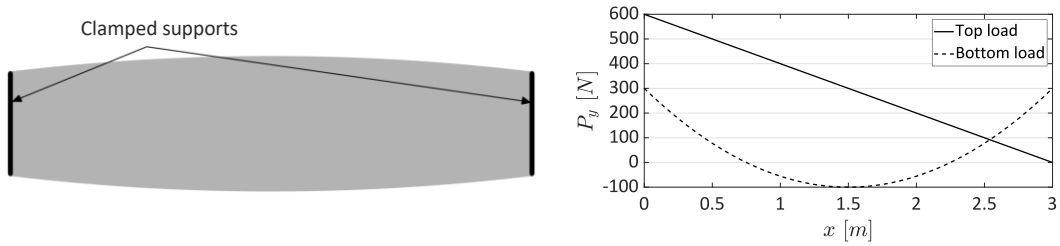

(a) (b)

Figure 60 - Wing rib boundary conditions: (a) Essential boundary; (b) Natural boundary

Table 27 - Wing rib structural optimization results

FEM		RPIM		NNRPIM	
					
61	4,43 h	48	3,88 h	40	1,79 h
					
75	5,47 h	60	4,85 h	50	2,28 h
					
89	6,74 h	75	6,10 h	60	2,79 h
					
93	7,10 h	86	7,09 h	72	3,37 h

3.3.3.1 OPTIMAL TOPOLOGY DESIGN AND STRUCTURAL ANALYSIS

After analysing the algorithm solutions presented in Table 27, an optimized model is designed based on a conventional beam structure design. Afterwards, a manual shape optimization is applied to the initial optimized model. The initial beam structure is converted into an organic structure with curved shapes, which may provide several advantages regarding stress concentrations and stiffness to weight ratio.

3.3.3.1.1 BEAM STRUCTURE DESIGN

The implementation of structural optimization allows to design an innovative wing rib structure. The conventional rib design presented in Figure 61a presents a surface area of $1{,}770\ m^2$. The structural optimization based design in Figure 61b reduces the surface area of the wing rib structure in 20,7% to $1{,}404\ m^2$. The algorithm optimization solutions in Table 27 denotes that major volume reduction is achieved by removing the inner centre material. Consequently, structure stiffness is highly dependent on the outward and centre beam dimensions. Therefore, the optimized model centre beams are thicker to resist bending, while side beams are thinner to minimize weight.

(a) (b)

Figure 61 - (a) Conventional rib model; (b) Optimized rib model

The structural analysis results for the original and optimized structures are presented in Table 28. Total displacement and VM stress distribution plots are shown in Table 29. The displacement presented in Table 28 are evaluated at the top middle of the rib. Compared with the conventional wing rib structure, the new developed design achieves a 20,7% volume reduction, whilst stiffness is decreased in 16,7%. Hence, the new design increases the stiffness to weigh ratio in 5,09%. The maximum VM stress is 30,2% higher, yet the induced stresses are considerably lower than the material yield stress.

As can be noticed in Table 29, stress concentrations arise in several beam junctions. Although the designed beam structure achieves a 20,7% volume reduction compared to the conventional rib design (corresponding to a 5,09% increase in the stiffness to weight ratio), the topological optimized structure can be further developed by substituting the beam structure design for an organic type structure.

Table 28 - Structural analysis results in the original and optimized rib structure

	Conventional structure	Beam structure
V_f	100%	79,3% (-20,7%)
$\|u\|\ [m]$	8,17E-08	9,8E-08 (+20,0%)
$K\ [N/m]$	1,22E+07	1,02E+07 (-16,7%)
$K/V_f\ [N/m]$	1,22E+07	1,29E+07 (+5,09%)
${\sigma_{VM}}^{max}$	7,34E+03	9,56E+03 (+30,2%)

Table 29 - Total displacement and VM stress fields of original and optimized rib structure

Conventional structure	Beam structure
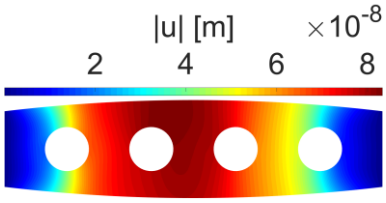	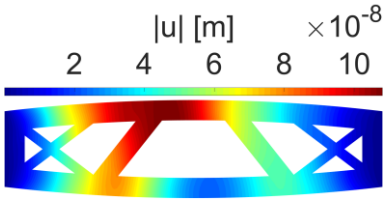
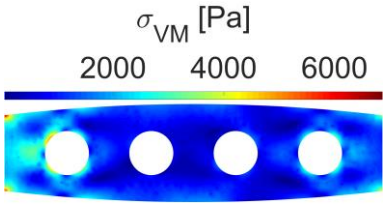	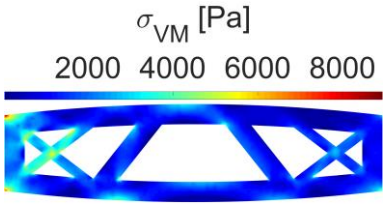

3.3.3.1.2 ORGANIC STRUCTURE DESIGN

Based on the initial optimized model, a new non-conventional structure design is developed. The designed model is more organic structure, possessing curved organic shapes, rather than conventional beam type structures. This type of structure may allow for less stress concentration and smooth stress fields. The organic structure design has a surface area of $1{,}480\ m^2$, corresponding to a 16,4% volume reduction compared with the conventional rib design. Even though the volume fraction is increased in 4,3%, the development of the initially optimized structure results in an increase in the stiffness to weight ratio from 5,09% to 8,45% (Table 30). Furthermore, maximum VM stress is also reduced if organic structures are used rather than conventional beam structures.

(a) (b) (c)

Figure 62 - (a) Conventional rib model; (b) Initial optimized rib model; (c) Modified optimized rib model

The application of such curved structures in aircraft industry is constrained by manufacturing processes, since producing such large structure is still a challenge to additive manufacturing techniques. Nonetheless, this work shows the potential of implementing organic type designs in structural components, which may be feasible to implement as additive manufacturing technology advances. This work demonstrates that new wing rib structures can be developed through structural optimization, achieving significant weight reduction compared with conventional rib designs. As demonstrated in this application, developing organic type structure within structural optimized components can significantly reduce maximum effective stress and maintain smooth stress fields. Even if induced stresses are substantially below material yield stress, the smooth stress fields obtained with this kind of structure can be well beneficial in several mechanical points of view, such as increased fatigue resistance or reduced vibrations.

Table 30 - Structural analysis results in the original and optimized rib structures

	Conventional structure	Beam structure	Organic structure
V_f	100%	79,3% (-20,7%)	83,6% (-16,4%)
$\|u\|\ [m]$	8,17E-08	9,8E-08 (+20,0%)	9,01E-08 (+10,3%)
$K\ [N/m]$	1,22E+07	1,02E+07 (-16,7%)	1,11E+07 (-9,33%)
$K/V_f\ [N/m]$	1,22E+07	1,29E+07 (+5,09%)	1,33E+07 (+8,45%)
${\sigma_{VM}}^{max}\ [Pa]$	7,34E+03	9,56E+03 (+30,2%)	8,61E+03 (+17,4%)

Table 31 - Displacement and VM stress fields of original and optimized rib structures

Conventional structure	Beam structure	Organic structure
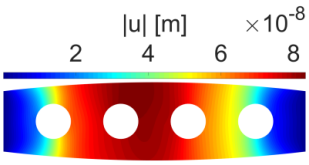	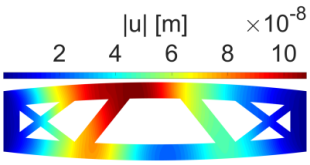	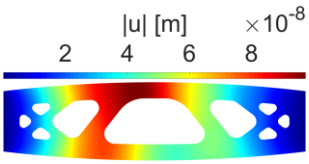
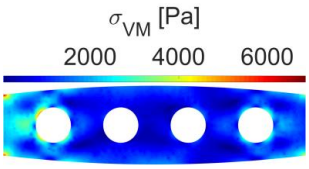	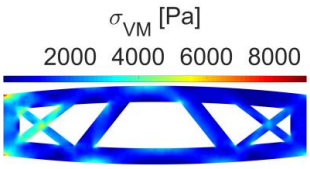	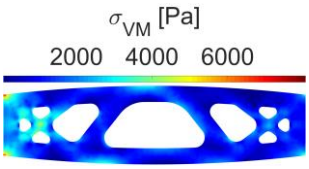

CONCLUSIONS

4.1 FUTURE WORKS

4 CONCLUSIONS AND PROPOSALS OF FUTURE WORKS

The focus of this dissertation was to extend two promising RPI meshless methods to the structural optimization field. By combining an evolutionary algorithm with the FEM, RPIM and NNRPIM, two benchmark optimization examples reported in the literature are firstly solved to calibrate algorithm parameters, study mesh influence and evaluate computational time of the optimization analyses. Posteriorly, the methodology was implemented in the structural optimization of industrial components. The combination of the evolutionary optimization algorithm with the FEM, RPIM and NNRPIM demonstrated to be an efficient tool in generating optimal designs.

To investigate and calibrate the proposed algorithm, the short-cantilever and "L" shaped bracket structural optimization benchmark examples were solved. Regarding algorithm parameters, mesh influence and computational time, the following conclusions were withdrawn:

i. Depending on the nodal density, the DR between 2% and 5% achieve better results. DR of 5% achieve satisfactory results if coarser meshes are used. On the other hand, as denser meshes are used, DR of 2% demonstrated to produce more consistent solutions;
ii. Although optimal topologies were achieved with sparse meshes, refined meshes produce more detailed and consistent solutions. Yet, the computational time is significantly affected;
iii. Higher decrease ratios achieve optimal topologies at lower computational times. However, lower DR result in more detailed, smooth and consistent solutions;
iv. Since the FEM, RPIM and NNRPIM demonstrated to have similar computational time per iteration, nodal density is the critical factor in computational time per iteration.

Supported by the benchmark analysis remarks, the calibrated methodology was extended to industrial applications. The carried-out analyses demonstrates that the FEM, RPIM and NNRPIM are solid numerical methods within structural optimization. Additionally, the developed designs represent the wide range of industrial applications in which structural optimization can be successfully implemented. An automotive wheel rim and pedal, as well as an aircraft wing rib were designed:

i. Through structural optimization, a new automotive wheel rim was designed, showing the potential of optimization algorithms to create innovative designs from an initial solid domain.
ii. Based on common pedal design, an optimized model was developed, achieving a 36% volume reduction, and a 25,2% increase in the stiffness to weigh ratio. The developed design demonstrates the effectiveness of topology optimization application to existing structures, as well as the benefits of size optimization of the obtained topology.
iii. Based on an initial continuous domain, a new aircraft wing rib design was developed. Compared with a conventional rib design, the developed design

achieves a 16,4% volume reduction, whilst increasing stiffness to weigh ratio in 8,45%. The designed organic structure demonstrates the benefits of exploring organic shapes in structural components. Compared with a conventional beam structure, reduced displacement and maximum VM stress were achieved whilst maintaining a significant volume reduction.

This work was developed on an academic software (FEMAS: cmech.webs.com), running in Matlab environment. Also associated to computer power and speed, the developed work is constrained by mesh density and computational time. Today, several commercial software are available to implement structural optimization. Commercial software may allow for better results within less computational time. Nonetheless, the developed methodology not only consolidates the FEM as a viable numerical method, but also highly enhances the potential of RPI meshless methods in structural optimization.

4.1 FUTURE WORKS

As in most numerical techniques, the computational time of the presented methodology is highly influenced by mesh density. Additionally, computer hardware characteristics may also affect the total time of the optimization analysis. Due to time restriction, the present work was developed only considering two-dimensional structures. Nonetheless, the same methodology can be extended to three-dimensional examples. Additionally, a complement to the work developed would be to experimentally validate the optimized structures. By producing through additive manufacturing, and testing the developed designs, the benefits of implementing structural optimization in the design of mechanical components can be further emphasized. Concerning the poor state of the art of meshless methods in structural optimization, investigating efficient meshless methods (RPIM and NNRPIM) in different optimization algorithms can further reinforce the meshless method advantages, and extend the range of applications in structural optimization. The future of structural optimization depends on the continuous development of computationally efficient algorithms and accurate numerical methods. Additionally, the development of additive manufacturing techniques and its coupling with structural optimization will continuously reinforce the advantages of implementing optimization algorithms in the product design phase, thus expanding the range of applications of structural optimization in industry.

REFERENCES

5 REFERENCES

[1] L. Rayleigh, “On the theory of resonance,” *Trans. R. Soc.*, vol. 161, 1870.

[2] W. Ritz, “Über eine neue methode zur lösung gewisser Variationsprobleme der mathematischen physik,” *J. fur die Reine und Angew. Math.*, vol. 135, pp. 1–61, 1909.

[3] B. G. Galerkin, “Series solution of some problems of elastic equilibrium of rods and plates,” *Vestn. Inzh. Tekh*, vol. 19, pp. 897–908, 1915.

[4] A. Hrennikoff, “Solution of Problems in Elasticity by the Frame Work Method,” *J. Appl. Mech.*, vol. 8, pp. 169–175, 1941.

[5] R. Courant, “Variational Methods for the Solution of Problems of Equilibrium and Vibrations,” *Bull. Am. Math. Soc.*, vol. 49, pp. 1–23, 1943.

[6] J. H. Argyris and S. Kelsey, “Energy Theorems and Structural Analysis.” Springer, 1960.

[7] M. J. Turner, R. W. Clough, H. C. Martin, and L. J. Topp, “Stiffness and Deflection Analysis of Complex Structures,” *J. Aeronaut. Sci.*, vol. 23, no. 9, pp. 805–823, 1956.

[8] R. W. Clough, “The Finite Element Method in Plane Stress Analysis,” *Proc. 2nd ASCE Conf. Electron. Comput. Pittsburgh, PA*, 1960.

[9] M. J. Turner, E. H. Dill, H. C. Martin, and R. J. Melosh, “Large Deflections of Structures Subjected to Heating and External Loads,” *J. Aerosp. Sci.*, vol. 27, pp. 97–106, 1960.

[10] J. S. Archer, “Consistent matrix formulations for structural analysis using finite-element techniques,” *AIAA J.*, vol. 3, no. 10, pp. 1910–1918, 1965.

[11] E. L. Wilson and R. E. Nickell, “Application of the finite element method to heat conduction analysis,” *Nucl. Eng. Des.*, vol. 4, pp. 276–286, 1966.

[12] H. C. Martin, “Finite element analysis of fluid flows,” *Proc. Second Conf. matrix methods Struct. Mech.*, 1968.

[13] O. C. Zienkiewicz, R. L. Taylor, and D. D. Fox, *The Finite Element Method for Solid and Structural Mechanics*, 7th ed. Butterworth-Heinemann, 2014.

[14] J. N. Reddy, *An Introduction to the finite element method*, 3rd ed. McGraw-Hill, 2006.

[15] K. J. Bathe, *Finite Element Procedures*, 2nd ed. Prentice Hall, Pearson Education, Inc., 2014.

[16] Y. W. Kwon and H. Bang, *The finite element method using matlab*, 1st ed. CRC Press, 2000.

[17] G. R. Liu and S. S. Quek, *The finite element method: a practical course*, 1st ed. Butterworth-Heinemann, 2003.

[18] C. A. Brebbia and J. Dominguez, *Boundary elements an introductory course*, 2nd ed. Boston, Southampton: WIT Press/Computational Mechanics Publications, 1992.

[19] G. Beer, I. Smith, and C. Duenser, *The boundary element method with programming for engineers and scientists*. Wien, New York: Springer, 2008.

[20] J. Gwinner and E. P. Stephan, *Advanced Boundary Element Methods Treatment of Boundary Value, Transmission and Contact Problems*. Springer, 2018.

[21] “Web of Science.” [Online]. Available: http://apps.webofknowledge.com/WOS_GeneralSearch_input.do?product=WO

S&search_mode=GeneralSearch&SID=F31nkeF3R4FAImUIyTg&preferencesSaved=. [Accessed: 16-Dec-2019].

[22] Y. T. GU, “Meshfree Methods and Their Comparisons,” *Int. J. Comput. Methods*, vol. 02, no. 04, pp. 477–515, 2005.

[23] V. P. Nguyen, T. Rabczuk, S. Bordas, and M. Duflot, “Meshless methods: A review and computer implementation aspects,” *Math. Comput. Simul.*, vol. 79, no. 3, pp. 763–813, 2008.

[24] J. S. Chen, M. Hillman, and S. W. Chi, “Meshfree methods: Progress made after 20 years,” *J. Eng. Mech.*, vol. 143, no. 4, 2017.

[25] J. C. Slater, “Electronic Energy Bands in Metals,” *Phys. Rev.*, vol. 45, no. 11, 1934.

[26] C. Lanczos, “Trigonometric Interpolation of Empirical and Analytical Functions,” *J. Math. Phys.*, vol. 17, no. 1–4, pp. 123–199, 1938.

[27] G. R. Liu and Y. T. Gu, *An introduction to meshfree methods and their programming*. Netherlands: Springer, 2005.

[28] R. A. Gingold and J. J. Monaghan, “Smoothed particle hydrodynamics: theory and application to non-spherical stars,” *Mon. Not. R. Astron. Soc.*, vol. 181, pp. 375–389, 1977.

[29] L. D. Libersky and A. G. Petschek, “Smooth Particle Hydrodynamics With Strength of Materials,” *Lect. Notes Phys.*, vol. 395, pp. 248–257, 1991.

[30] L. Wing Kam, S. Jun, and Z. Yi Fei, “Reproducing kernel particle methods,” *Int. J. Numer. Methods Fluids*, vol. 20, no. 8–9, pp. 1081–1106, 1995.

[31] B. Nayroles, G. Touzot, and P. Villon, “Generalizing the finite element method: Diffuse approximation and diffuse elements,” *Comput. Mech.*, vol. 10, no. 5, pp. 307–318, 1992.

[32] P. Lancaster and K. Salkauskas, “Surfaces Generated by Moving Least Squares Methods,” *Math. Comput.*, vol. 37, no. 155, p. 141, 1981.

[33] T. Belytschko, Y. Y. Lu, and L. Gu, “Element-free Galerkin methods,” *Int. J. Numer. Methods Eng.*, vol. 37, no. 2, pp. 229–256, 1994.

[34] S. N. Atluri and T. Zhu, “A new Meshless Local Petrov-Galerkin (MLPG) approach in computational mechanics,” *Comput. Mech.*, vol. 22, no. 2, pp. 117–127, 1998.

[35] S. De and K. J. Bathe, “The method of finite spheres,” *Comput. Mech.*, vol. 25, no. 4, pp. 329–345, 2000.

[36] J. Braun and M. Sambridge, “A numerical method for solving partial differential equations on highly irregular evolving grids,” *Nature*, vol. 376. pp. 655–660, 1995.

[37] N. Sukumar, B. Moran, and T. Belytschko, “The natural element method in solid mechanics,” *Int. J. Numer. Methods Eng.*, vol. 43, pp. 839–887, 1998.

[38] G. R. Liu and Y. T. Gu, “A point interpolation method for two-dimensional solids,” *Int. J. Numer. Methods Eng.*, vol. 50, no. 4, pp. 937–951, 2001.

[39] J. G. Wang and G. R. Liu, “A point interpolation meshless method based on radial basis functions,” *Int. J. Numer. Methods Eng.*, vol. 54, no. 11, pp. 1623–1648, 2002.

[40] L. M. J. S. Dinis, R. M. Natal Jorge, and J. Belinha, “Analysis of 3D solids using the natural neighbour radial point interpolation method,” *Comput. Methods Appl. Mech. Eng.*, vol. 196, no. 13–16, pp. 2009–2028, 2007.

[41] J. Belinha, L. M. J. S. Dinis, and R. M. N. Jorge, “The natural radial element method,” *Int. J. Numer. Methods Eng.*, pp. 1885–1891, 2012.

[42] J. Belinha, L. M. J. S. Dinis, and R. M. N. Jorge, “Composite laminated plate analysis

using the natural radial element method," *Compos. Struct.*, vol. 103, pp. 50–67, 2013.

[43] J. Belinha, L. M. J. S. Dinis, and R. M. Natal Jorge, "Analysis of thick plates by the natural radial element method," *Int. J. Mech. Sci.*, vol. 76, pp. 33–48, 2013.

[44] G. R. Liu, K. Y. Dai, K. M. Lim, and Y. T. Gu, "A point interpolation mesh free method for static and frequency analysis of two-dimensional piezoelectric structures," *Comput. Mech.*, vol. 29, no. 6, pp. 510–519, 2002.

[45] J. Belinha, *Meshless Methods in Biomechanics - Bone Tissue Remodelling Analysis*, 1st ed. Cham, Heidelberg, New York, Dordrecht, London: Springer, 2014.

[46] G. R. Liu, Y. Li, K. Y. Dai, M. T. Luan, and W. Xue, "A linearly conforming interpolation method for solid mechanics problems," *Int. J. Comput. Methods*, vol. 3, no. 4, pp. 401–428, 2006.

[47] G. R. Liu, G. Y. Zhang, Y. Y. Wang, Z. H. Zhong, G. Y. Li, and X. Han, "A nodal integration technique for meshfree radial point interpolation method (NI-RPIM)," *Int. J. Solids Struct.*, vol. 44, no. 11–12, pp. 3840–3860, 2007.

[48] X. Y. Cui, H. Feng, G. Y. Li, and S. Z. Feng, "A cell-based smoothed radial point interpolation method (CS-RPIM) for three-dimensional solids," *Eng. Anal. Bound. Elem.*, vol. 50, pp. 474–485, 2015.

[49] G. R. Liu, Y. Jiang, L. Chen, G. Y. Zhang, and Y. W. Zhang, "A singular cell-based smoothed radial point interpolation method for fracture problems," *Comput. Struct.*, vol. 89, no. 13–14, pp. 1378–1396, 2011.

[50] G. Voronoi, "Nouvelles applications des paramètres continus à la théorie des formes quadratiques. Deuxiäme Memoire. Reeherches sur les parallelloedres primitifs.," *J. für die Reine und Angew. Math.*, vol. 134, pp. 198–287, 1908.

[51] B. Delauney, "SUR LA SPHÈRE VIDE. A LA MÉMOIRE DE GEORGES VORONOÏ," *Izv. Akad. Nauk SSSR, Otd. Mat. i Estestv. Nauk*, pp. 793–800, 1934.

[52] L. M. J. S. Dinis, R. M. Natal Jorge, and J. Belinha, "Analysis of plates and laminates using the natural neighbour radial point interpolation method," *Eng. Anal. Bound. Elem.*, vol. 32, no. 3, pp. 267–279, 2008.

[53] L. M. J. S. Dinis, R. M. N. Jorge, and J. Belinha, "An unconstrained third-order plate theory applied to functionally graded plates using a meshless method," *Mech. Adv. Mater. Struct.*, vol. 17, no. 2, pp. 108–133, 2010.

[54] L. M. J. S. Dinis, R. M. Jorge, and J. Belinha, "Composite laminated plates: A 3D natural neighbor radial point interpolation method approach," *Journal of Sandwich Structures and Materials*, vol. 12, no. 2. pp. 119–138, 2010.

[55] L. M. J. S. Dinis, R. M. N. Jorge, and J. Belinha, "A 3D shell-like approach using a natural neighbour meshless method: Isotropic and orthotropic thin structures," *Compos. Struct.*, vol. 92, no. 5, pp. 1132–1142, 2010.

[56] L. M. J. S. Dinis, R. M. Natal Jorge, and J. Belinha, "The natural neighbour radial point interpolation method: Dynamic applications," *Eng. Comput. (Swansea, Wales)*, vol. 26, no. 8, pp. 911–949, 2009.

[57] L. M. J. S. Dinis, R. M. N. Jorge, and J. Belinha, "Static and dynamic analysis of laminated plates based on an unconstrained third order theory and using a radial point interpolator meshless method," *Comput. Struct.*, vol. 89, no. 19–20, pp. 1771–1784, 2011.

[58] L. M. J. S. Dinis, R. M. Natal Jorge, and J. Belinha, "A natural neighbour meshless method with a 3D shell-like approach in the dynamic analysis of thin 3D structures," *Thin-Walled Struct.*, vol. 49, no. 1, pp. 185–196, 2011.

[59] C. F. Santos, J. Belinha, F. Gentil, M. Parente, and R. N. Jorge, "The free vibrations

analysis of the cupula in the inner ear using a natural neighbor meshless method," *Eng. Anal. Bound. Elem.*, vol. 92, no. August 2017, pp. 50–63, 2018.

[60] J. Belinha, J. M. C. Azevedo, L. M. J. S. Dinis, and R. M. N. Jorge, "Simulating fracture propagation in brittle materials using a meshless approach," *Eng. Comput.*, vol. 34, no. 3, pp. 503–522, 2018.

[61] J. Belinha, J. M. C. Azevedo, L. M. J. S. Dinis, and R. M. N. Jorge, "The Natural Neighbor Radial Point Interpolation Method in Computational Fracture Mechanics: A 2D Preliminary Study," *Int. J. Comput. Methods*, vol. 14, no. 4, pp. 1–25, 2017.

[62] B. V. Farahani, P. J. Tavares, J. Belinha, and P. M. G. P. Moreira, "A Fracture Mechanics Study of a Compact Tension Specimen: Digital Image Correlation, Finite Element and Meshless Methods," *Procedia Struct. Integr.*, vol. 5, pp. 920–927, 2017.

[63] J. M. C. Azevedo, J. Belinha, L. M. J. S. Dinis, and R. M. Natal Jorge, "Crack path prediction using the natural neighbour radial point interpolation method," *Eng. Anal. Bound. Elem.*, vol. 59, pp. 144–158, 2015.

[64] L. M. J. S. Dinis, R. M. Natal Jorge, and J. Belinha, "Large deformation applications with the radial natural neighbours interpolators," *C. - Comput. Model. Eng. Sci.*, vol. 44, no. 1, pp. 1–34, 2009.

[65] R. Sibson, "A brief description of natural neighbor interpolation," *Barnett V Interpret. Multivar. data. Wiley, Chichester*, pp. 21–36, 1981.

[66] F. P. Preparata and M. I. Shamos, *Computational Geometry: An Introduction*. New York: Springer-Verlag, 1985.

[67] B. N. Boots, *Voronoï (Thiessen) polygons*. Norwich: Geo Books, 1986.

[68] A. Okabe, B. Boots, K. Sugihara, and S. N. Chiu, *Spatial Tessellations: Concepts and Applications of Voronoï Diagrams*, 2nd ed. Chichester: John Wiley & Sons, LTD, 2000.

[69] C. L. Lawson, "Software for C1 Surface Interpolation," *Math. Softw.*, pp. 161–194, 1977.

[70] D. F. Watson, *Contouring: a guide to the analysis and display of spatial data*. Oxford: Pergamon Press, 1992.

[71] I. Babuška, U. Banerjee, J. E. Osborn, and Q. Zhang, "Effect of numerical integration on meshless methods," *Comput. Methods Appl. Mech. Eng.*, vol. 198, no. 37–40, pp. 2886–2897, 2009.

[72] J. S. Chen, S. Yoon, and C. T. Wu, "Non-linear version of stabilized conforming nodal integration for Galerkin mesh-free methods," *Int. J. Numer. Methods Eng.*, vol. 53, no. 12, pp. 2587–2615, 2002.

[73] S. De and K. J. Bathe, "The method of finite spheres with improved numerical integration," *Comput. Struct.*, vol. 79, pp. 2183–2196, 2001.

[74] J. S. Chen, C. T. Wu, S. Yoon, and Y. You, "A stabilized conforming nodal integration for Galerkin mesh-free methods," *Int. J. Numer. Methods Eng.*, vol. 50, no. 2, pp. 435–466, 2001.

[75] J. Dolbow and T. Belytschko, "Numerical integration of the Galerkin weak form in meshfree methods," *Comput. Mech.*, vol. 23, no. 3, pp. 219–230, 1999.

[76] S. Beissel and T. Belytschko, "Nodal integration of the element-free Galerkin method," *Comput. Methods Appl. Mech. Eng.*, vol. 139, no. 1–4, pp. 49–74, 1996.

[77] G. R. Liu, "A point assembly method for stress analysis for two-dimensional solids," *Int. J. Solids Struct.*, vol. 39, pp. 261–276, 2002.

[78] G. R. Liu, *Meshfree Methods Moving Beyond the Finte Element Method*, 2nd ed. CRC Press, 2011.

[79] K. Y. Sze, J. S. Chen, N. Sheng, and X. H. Liu, "Stabilized conforming nodal integration: Exactness and variational justification," *Finite Elem. Anal. Des.*, vol. 41, no. 2, pp. 147–171, 2004.

[80] K. Y. Dai, G. R. Liu, X. Han, and Y. Li, "Inelastic analysis of 2D solids using a weak-form RPIM based on deformation theory," *Comput. Methods Appl. Mech. Eng.*, vol. 195, no. 33–36, pp. 4179–4193, 2006.

[81] W. Elmer, J. S. Chen, M. Puso, and E. Taciroglu, "A stable, meshfree, nodal integration method for nearly incompressible solids," *Finite Elem. Anal. Des.*, vol. 51, pp. 81–85, 2012.

[82] R. L. Hardy, "Theory and applications of the multiquadric-biharmonic method," *Comput. Math. with Appl.*, vol. 19, no. 8–9, pp. 163–208, 1990.

[83] J. Duchon, "Splines minimizing rotation invariant seminorms in Sobolev spaces. In: Schemmp W, Zeller K (eds) Constructive theory of functions of several variables.," in *Lecture notes in Mathematics*, Berlin: Springer, 1977.

[84] M. A. Golberg, C. S. Chen, and H. Bowman, "Some recent results and proposals for the use of radial basis functions in the BEM," *Eng. Anal. Bound. Elem.*, vol. 23, no. 4, pp. 285–296, 1999.

[85] O. M. Querin, M. Victoria, C. Alonso, R. Ansola, and P. Martí, *Topology Design Methods for Structural Optimization*, 1st ed. Elsevier Ltd, 2017.

[86] M. P. Bendsøe and O. Sigmund, *Topology Optimization*, 2nd ed. Springer, 2004.

[87] A. G. M. Michell, "LVIII. The limits of economy of material in frame-structures," *London, Edinburgh, Dublin Philos. Mag. J. Sci.*, vol. 8, no. 47, pp. 589–597, 1904.

[88] G. I. N. Rozvany, "Grillages of maximum strength and maximum stiffness," *Int. J. Mech. Sci.*, vol. 14, no. 10, pp. 651–666, 1972.

[89] G. I. N. Rozvany, "Optimum Choice of Determinate Trusses under Multiple Loads," *J. Struct. Div.*, vol. 103, no. 12, pp. 2432–2433, 1977.

[90] E. Tyflopoulos, D. T. Flem, M. Steinert, and A. Olsen, "State of the art of generative design and topology optimization and potential research needs," *Proc. Nord. Des. Era Digit. Nord. 2018*, pp. 1–15, 2018.

[91] M. P. Bendsøe and N. Kikuchi, "Generating optimal topologies in structural design using a homogenization method," *Comput. Methods Appl. Mech. Eng.*, vol. 71, no. 2, pp. 197–224, 1988.

[92] M. P. Bendsøe, "Optimal shape design as a material distribution problem," *Struct. Optim.*, vol. 1, no. 4, pp. 193–202, 1989.

[93] M. Zhou and G. I. N. Rozvany, "The COC algorithm, Part II: Topological, geometrical and generalized shape optimization," *Comput. Methods Appl. Mech. Eng.*, vol. 89, no. 1–3, pp. 309–336, 1991.

[94] G. I. N. Rozvany, M. Zhou, and T. Birker, "Generalized shape optimization without homogenization," *Struct. Optim.*, vol. 4, no. 3–4, pp. 250–252, 1992.

[95] Y. M. Xie and G. P. Steven, "A simple evolutionary procedure for structural optimization," *Compurers Struct.*, vol. 49, no. 5, pp. 885–896, 1993.

[96] O. M. Querin, G. P. Steven, and Y. M. Xie, "Evolutionary structural optimisation (ESO) using a bidirectional algorithm," *Eng. Comput.*, vol. 15, no. 8, pp. 1031–1048, 1998.

[97] X. Y. Yang, Y. M. Xie, G. P. Steven, and O. M. Querin, "Bi-directional evolutionary method for stiffness optimisation," *AIAA J.*, vol. 37, no. 11, pp. 1493–1488, 1999.

[98] O. M. Querin, G. P. Steven, and Y. M. Xie, “Evolutionary structural optimisation using an additive algorithm,” *Finite Elem. Anal. Des.*, vol. 34, no. 3–4, pp. 291–308, 2000.

[99] O. M. Querin, V. Young, G. P. Steven, and Y. M. Xie, “Computational efficiency and validation of bi-directional evolutionary structural optimization,” *Comput. Methods Appl. Mech. Eng.*, vol. 189, no. 2, pp. 559–573, 2000.

[100] M. Burger, B. Hackl, and W. Ring, “Incorporating topological derivatives into level set methods,” *J. Comput. Phys.*, vol. 194, no. 1, pp. 344–362, 2004.

[101] J. Sokolowski and A. Zochowski, “On the topological derivative in shape optimization,” *SIAM J. Control Optim.*, vol. 37, no. 4, pp. 1251–1272, 1999.

[102] H. A. Eschenauer, V. V. Kobelev, and A. Schumacher, “Bubble method for topology and shape optimization of structures,” *Struct. Optim.*, vol. 8, no. 1, pp. 42–51, 1994.

[103] H. Jia, H. G. Beom, Y. Wang, S. Lin, and B. Liu, “Evolutionary level set method for structural topology optimization,” *Comput. Struct.*, vol. 89, no. 5–6, pp. 445–454, 2011.

[104] M. Y. Wang, S. Chen, X. Wang, and Y. Mei, “Design of multimaterial compliant mechanisms using level-set methods,” *J. Mech. Des. Trans. ASME*, vol. 127, no. 5, pp. 941–956, 2005.

[105] G. Allaire, F. Jouve, and A. M. Toader, *Structural optimization using sensitivity analysis and a level-set method*, vol. 194, no. 1. 2004.

[106] J. A. Sethian and A. Wiegmann, “Structural Boundary Design via Level Set and Immersed Interface Methods,” *J. Comput. Phys.*, vol. 163, no. 2, pp. 489–528, 2000.

[107] G. Allaire, F. Jouve, and A. M. Toader, “A level-set method for shape optimization,” *Comptes Rendus Math.*, vol. 334, pp. 1125–1130, 2002.

[108] M. Wallin and M. Ristinmaa, “Boundary effects in a phase-field approach to topology optimization,” *Comput. Methods Appl. Mech. Eng.*, vol. 278, pp. 145–159, 2014.

[109] B. Bourdin and A. Chambolle, “Design-Dependent Loads in Topology Optimization,” *ESAIM Control. Optim. Calc. Var.*, vol. 9, pp. 19–48, 2003.

[110] S. Y. Wang and K. Tai, “Structural topology design optimization using Genetic Algorithms with a bit-array representation,” *Comput. Methods Appl. Mech. Eng.*, vol. 194, no. 36–38, pp. 3749–3770, 2005.

[111] X. Liu, W. J. Yi, Q. S. Li, and P.-S. Shen, “Genetic evolutionary structural optimization,” *J. Constr. Steel Res.*, vol. 64, pp. 305–311, 2008.

[112] A. H. Taheri and K. Suresh, “An isogeometric approach to topology optimization of multi-material and functionally graded structures,” *Int. J. Numer. Methods Eng.*, vol. 109, no. 5, pp. 668–696, 2016.

[113] Q. X. Lieu and J. Lee, “A multi-resolution approach for multi-material topology optimization based on isogeometric analysis,” *Comput. Methods Appl. Mech. Eng.*, 2017.

[114] O. Sigmund and K. Maute, “Topology optimization approaches: A comparative review,” *Struct. Multidiscip. Optim.*, vol. 48, no. 6, pp. 1031–1055, 2013.

[115] J. D. Deaton and R. V. Grandhi, “A survey of structural and multidisciplinary continuum topology optimization: Post 2000,” *Struct. Multidiscip. Optim.*, vol. 49, pp. 1–38, 2013.

[116] G. I. N. Rozvany, “A critical review of established methods of structural topology optimization,” *Struct. Multidiscip. Optim.*, vol. 37, pp. 217–237, 2009.

[117] C. H. G. Li, “Design of the lower chassis of a monorail personal rapid transit (MPRT) car using the evolutionary structural optimization (ESO) method,” *Struct. Multidiscip. Optim.*, vol. 54, no. 1, pp. 165–175, 2016.

[118] Z. O. C. and C. J. S., “Shape optimization and sequential linear programming,” *Gall. RH, Zienkie- wicz OC Optim. Struct. Des. Wiley, New York*, pp. 109–126, 1973.

[119] C. A. M. Soares, H. C. Rodrigues, and K. K. Choi, “Shape Optimal Structural Design Using Boundary Elements and Minimum Compliance Techniques,” *J. Mech. Des. Trans. ASME*, vol. 106, no. 4, pp. 518–523, 1984.

[120] C. A. M. Soares, H. C. Rodrigues, L. M. O. Faria, and E. J. Haug, “Optimization of the Geometry of Shafts Using Boundary Elements,” *J. Mech. Transm. Autom. Des.*, vol. 106, pp. 199–202, 1984.

[121] R. J. Yang, “Component shape optimization using bem,” *Comput. Struct.*, vol. 37, no. 4, pp. 561–568, 1990.

[122] Z. Zhao, *Shape Design Sensitivity Analysis using the Boundary Element Method - Lecture Notes in Engineering 62*. Springer-Verlag, 1991.

[123] K. Yamazaki, J. Sakamoto, and M. Kitano, “Three-dimensional shape optimization using the boundary element method,” *AIAA J.*, vol. 32, no. 6, pp. 1295–1301, 1994.

[124] X. Wei, A. Chandra, L.-J. Leu, and S. Mukherjee, “SHAPE OPTIMIZATION IN ELASTICITY AND ELASTO VISCOPLASTICITY BY THE BOUNDARY ELEMENT METHOD XIN,” *Int. J. Solids Struct.*, vol. 31, no. 4, pp. 533–550, 1994.

[125] I. Grindeanu, K. H. Chang, K. K. Choi, and J. S. Chen, “Design sensitivity analysis of hyperelastic structures using a meshless method,” *AIAA J.*, vol. 36, no. 4, pp. 618–627, 1998.

[126] I. Grindeanu, K. K. Choi, J.-S. Chen, and K.-H. Chang, “Shape design optimization of hyperelastic structures using a meshless method,” *AIAA J.*, vol. 37, no. 8, pp. 990–997, 1999.

[127] I. Grindeanu, N. H. Kim, K. K. Choi, and J. S. Chen, “CAD-Based Shape Optimization Using a Meshfree Method,” *Concurr. Eng.*, vol. 10, no. 1, pp. 55–66, 2002.

[128] N. H. Kim, K. K. Choi, and M. E. Botkin, “Numerical method for shape optimization using meshfree method,” *Struct. Multidiscip. Optim.*, vol. 24, no. 6, pp. 418–429, 2003.

[129] Z. Q. Zhang, J. X. Zhou, N. Zhou, X. M. Wang, and L. Zhang, “Shape optimization using reproducing kernel particle method and an enriched genetic algorithm,” *Comput. Methods Appl. Mech. Eng.*, vol. 194, no. 39–41, pp. 4048–4070, 2005.

[130] W. Zou, J. X. Zhou, Z. Q. Zhang, and Q. Li, “A truly meshless method based on partition of unity quadrature for shape optimization of continua,” *Comput. Mech.*, vol. 39, no. 4, pp. 357–365, 2007.

[131] S. Cho and J. Kwak, “Topology design optimization of geometrically non-linear structures using meshfree method,” *Comput. Methods Appl. Mech. Eng.*, vol. 195, pp. 5909–5925, 2006.

[132] M. Duflot and H. Nguyen-Dang, “A truly meshless Galerkin method based on a moving least squares quadrature,” *Commun. Numer. Methods Eng.*, vol. 18, pp. 441–449, 2002.

[133] Z. Q. Zhang, J. X. Zhou, X. M. Wang, Y. F. Zhang, and L. Zhang, “Investigations on reproducing kernel particle method enriched by partition of unity and visibility criterion,” *Comput. Mech.*, vol. 34, no. 4, pp. 310–329, 2004.

[134] F. Bobaru and S. Mukherjee, “Shape sensivity analysis and shape optimization in planar elasticity using the element-free Galerkin method,” *Comput. Methods*

Appl. Mech. Eng., vol. 190, no. 32–33, pp. 4319–4337, 2001.

[135] F. Bobaru and S. Mukherjee, "Meshless approach to shape optimization of linear thermoelastic solids," *Int. J. Numer. Methods Eng.*, vol. 53, pp. 765–796, 2002.

[136] F. Bobaru and S. Rachakonda, "E(FG)2: A new fixed-grid shape optimization method based on the element-free galerkin mesh-free analysis: Taking large steps in shape optimization," *Struct. Multidiscip. Optim.*, vol. 32, pp. 215–228, 2006.

[137] Z. Juan, L. Shuyao, and L. Guangyao, "The topology optimization design for continuum structures based on the element free Galerkin method," *Eng. Anal. Bound. Elem.*, vol. 34, no. 7, pp. 666–672, 2010.

[138] Z. Luo, N. Zhang, Y. Wang, and W. Gao, "Topology optimization of structures using meshless density variable approximants," *Int. J. Numer. Methods Eng.*, 2012.

[139] F. Zhao, "Topology optimization with meshless density variable approximations and BESO method," *Comput. Aided Des.*, vol. 56, pp. 1–10, 2014.

[140] V. Shobeiri, "The topology optimization design for cracked structures," *Eng. Anal. Bound. Elem.*, vol. 58, pp. 26–38, 2015.

[141] Y. Wang, Z. Luo, J. Wu, and N. Zhang, "Topology optimization of compliant mechanisms using element-free Galerkin method," *Adv. Eng. Softw.*, vol. 85, pp. 61–72, 2015.

[142] V. Shobeiri, "Topology optimization using bi-directional evolutionary structural optimization based on the element-free Galerkin method," *Eng. Optim.*, vol. 48, no. 3, pp. 380–396, 2016.

[143] M. Cui, H. Chen, J. Zhou, and F. Wang, "A meshless method for multi-material topology optimization based on the alternating active-phase algorithm," *Eng. Comput.*, vol. 33, no. 4, pp. 871–884, 2017.

[144] X. Yang, J. Zheng, and S. Long, "Topology optimization of continuum structures with displacement constraints based on meshless method," *Int. J. Mech. Mater. Des.*, vol. 13, no. 2, pp. 311–320, 2017.

[145] K. Wang, S. Zhou, Z. Nie, and S. Kong, "Natural neighbour Petrov-Galerkin Method for shape design sensitivity analysis," *C. - Comput. Model. Eng. Sci.*, vol. 26, no. 2, pp. 107–121, 2008.

[146] S. Li and S. N. Atluri, "The MLPG mixed collocation method for material orientation and topology optimization of anisotropic solids and structures," *C. - Comput. Model. Eng. Sci.*, vol. 30, no. 1, pp. 37–56, 2008.

[147] J. Zheng, S. Long, Y. Xiong, and G. Li, "A finite volume meshless local petrov-galerkin method for topology optimization design of the continuum structures," *C. - Comput. Model. Eng. Sci.*, vol. 42, no. 1, pp. 19–34, 2009.

[148] S. L. Li, S. Y. Long, and G. Y. Li, "A topology optimization of moderately thick plates based on the meshless numerical method," *C. - Comput. Model. Eng. Sci.*, vol. 60, no. 1, pp. 73–94, 2010.

[149] S. Li and S. N. Atluri, "Topology-optimization of structures based on the MLPG mixed collocation method," *C. - Comput. Model. Eng. Sci.*, vol. 26, no. 1, pp. 61–74, 2008.

[150] J. Lin, Y. Guan, G. Zhao, H. Naceur, and P. Lu, "Topology optimization of plane structures using smoothed particle hydrodynamics method," *Int. J. Numer. Methods Eng.*, pp. 1–18, 2016.

[151] E. Andreassen, A. Clausen, M. Schevenels, B. S. Lazarov, and O. Sigmund, "Efficient topology optimization in MATLAB using 88 lines of code," *Struct. Multidiscip. Optim.*, vol. 43, pp. 1–16, 2011.

[152] J. Zheng, S. Long, Y. Xiong, and L. Guangyao, "A Topology Optimization Design for

the Continuum Structure Based on the Meshless Numerical Technique," *Comput. Model. Eng. Sci.*, vol. 34, no. 2, pp. 137–154, 2008.

[153] S.-J. Lee, C.-K. Lee, and J.-E. Bae, "Evolution of 2D Truss Structures using Topology Optimization Technique with Meshless Method," *Proc. Int. Assoc. Shell Spat. Struct. Symp.*, pp. 1058–1065, 2009.

[154] M. Seabra *et al.*, "Selective laser melting (SLM) and topology optimization for lighter aerospace componentes," *Procedia Struct. Integr.*, vol. 1, pp. 289–296, 2016.

[155] M. Liang, J. Hu, S. Li, and Z. Chen, "Topology optimization of transmission gearbox under multiple working loads," *Adv. Mech. Eng.*, vol. 10, no. 11, pp. 1–7, 2018.

[156] M. Abdi, I. Ashcroft, and R. D. Wildman, "Design optimization for an additively manufactured automotive component," *Int. J. Powertrains*, vol. 7, pp. 142–161, 2018.

[157] G. Shanmugasundar, R. Sivaramakrishnan, S. Meganathan, and S. Balasubramani, "Structural optimization of an five degrees of freedom (T-3R-T) robot manipultor using finite element analysis," *Mater. Today Proc.*, vol. 16, pp. 1325–1332, 2019.

[158] D. J. Munk, D. J. Auld, G. P. Steven, and G. A. Vio, "On the benefits of applying topology optimization to structural design of aircraft components," *Struct. Multidiscip. Optim.*, vol. 60, no. 3, pp. 1245–1266, 2019.

[159] J. M. G. Barry J. Goodno, *Mechanics of Materials*, 9th ed. CENGAGE Learning, 2018.

[160] K. Suzuki and N. Kikuchi, "Shape and topology optimization by a homogenization method," *Comput. Methods Appl. Mech. Eng.*, vol. 93, pp. 291–318, 1991.

[161] X. Huang and Y. M. Xie, "Convergent and mesh-independent solutions for the bi-directional evolutionary structural optimization method," *Finite Elem. Anal. Des.*, vol. 43, no. 14, pp. 1039–1049, 2007.

[162] X. Huang and Y. M. Xie, *Evolutionary Topology Optimization of Continuum Structures*. WILEY, 2010.

[163] C. Conlan-Smith and K. A. James, "A stress-based topology optimization method for heterogeneous structures," *Struct. Multidiscip. Optim.*, vol. 60, no. 1, pp. 167–183, 2019.

[164] R. Picelli, S. Townsend, C. Brampton, J. Norato, and H. A. Kim, "Stress-based shape and topology optimization with the level set method," *Comput. Methods Appl. Mech. Eng.*, vol. 329, pp. 1–23, 2018.

[165] L. Xia, L. Zhang, Q. Xia, and T. Shi, "Stress-based topology optimization using bi-directional evolutionary structural optimization method," *Comput. Methods Appl. Mech. Eng.*, vol. 333, pp. 356–370, 2018.

[166] H. Wang, J. Liu, X. Qian, X. Fan, and G. Wen, "Continuum structural layout in consideration of the balance of the safety and the properties of structures," *Lat. Am. J. Solids Struct.*, vol. 14, no. 6, pp. 1143–1169, 2017.

[167] E. Biyikli and A. C. To, "Proportional topology optimization: A new non-sensitivity method for solving stress constrained and minimum compliance problems and its implementation in MATLAB," *PLoS One*, vol. 10, no. 12, pp. 1–23, 2015.

[168] E. Holmberg, B. Torstenfelt, and A. Klarbring, "Stress constrained topology optimization," *Struct. Multidiscip. Optim.*, vol. 48, no. 1, pp. 33–47, 2013.

[169] A. Verbart, M. Langelaar, N. Van Dijk, and F. Van Keulen, "Level set based topology optimization with stress constraints and consistent sensitivity analysis," *Collect. Tech. Pap. - AIAA/ASME/ASCE/AHS/ASC Struct. Struct. Dyn. Mater. Conf.*, pp. 1–15, 2012.

[170] C. Le, J. Norato, T. Bruns, C. Ha, and D. Tortorelli, “Stress-based topology optimization for continua,” *Struct. Multidiscip. Optim.*, vol. 41, no. 4, pp. 605–620, 2010.

[171] M. N. Sudin, M. M. Tahir, F. R. Ramli, and S. A. Shamsuddin, “Topology optimization in automotive brake pedal redesign,” *Int. J. Eng. Technol.*, vol. 6, no. 1, pp. 398–402, 2014.

[172] M. I. M. Sargini, S. H. Masood, S. Palanisamy, E. Jayamani, and A. Kapoor, “Finite element analysis of automotive arm brake pedal for rapid manufacturing,” *IOP Conf. Ser. Mater. Sci. Eng.*, vol. 715, no. 1, 2020.

[173] L. Krog, A. Tucker, and G. Rollema, “Application of topology, sizing and shape optimization methods to optimal design of aircraft components,” *3rd Altair UK HyperWorks Users Conf.*, pp. 1–12, 2002.

[174] L. Krog, A. Tucked, M. Kemp, and R. Boyd, “Topology optimization of aircraft wing box ribs,” *Collect. Tech. Pap. - 10th AIAA/ISSMO Multidiscip. Anal. Optim. Conf.*, vol. 3, pp. 2020–2030, 2004.

[175] B. K. Stanford and P. D. Dunning, “Optimal Topology of Aircraft Rib and Spar Structures under Aeroelastic Loads,” pp. 1–23, 2014.

[176] A. Rinku and G. K. Ananthasuresh, “Topology and Size Optimization of Modular Ribs in Aircraft Wings,” *11th World Congr. Struct. Multidiscip. Optim.*, pp. 1–6, 2015.